PORE-SCALE MODELING OF THE SURFACE ROUGHNESS EFFECT ON FLUID-FLUID INTERFACIAL AREA FOR CONTAMINANT TRANSPORT IN VADOSE ZONE

by

Hao Jiang

Copyright © Hao Jiang 2020

A Dissertation Submitted to the Faculty of the

DEPARTMENT OF CHEMICAL AND ENVIRONMENTAL ENGINEERING

In Partial Fulfillment of the Requirements

For the Degree of

DOCTOR OF PHILOSOPHY
WITH A MAJOR IN ENVIRONMENTAL ENGINEERING

In the Graduate College

THE UNIVERSITY OF ARIZONA

2020

THE UNIVERSITY OF ARIZONA
GRADUATE COLLEGE

As members of the Dissertation Committee, we certify that we have read the dissertation prepared by Hao Jiang, titled "Pore-scale Modeling of the Surface Roughness Effect on Fluid-Fluid Interfacial Area for Contaminant Transport in Vadose Zone" and recommend that it be accepted as fulfilling the dissertation requirement for the Degree of Doctor of Philosophy.

Mark L Brusseau Date: 10 Jan 2020
Dr. Mark L. Brusseau

Date: 1/10/2020
Dr. Bo Guo

James Farrell Date: 1/10/2020
Dr. James Farrell

Final approval and acceptance of this dissertation is contingent upon the candidate's submission of the final copies of the dissertation to the Graduate College.

I hereby certify that I have read this dissertation prepared under my direction and recommend that it be accepted as fulfilling the dissertation requirement.

Mark L Brusseau Date: 10 Jan 2020
Dissertation Committee Chair: Dr. Mark L. Brusseau

TABLE OF CONTENTS

LIST OF FIGURES

LIST OF TABLES

ABSTRACT

Interaction between solid, wetting fluids and nonwetting fluids frequently occurs in natural environmental processes. An ongoing concern for researchers is the fluid-fluid interfaces on rough solid surfaces inside natural porous media. Interfacial area between the immiscible fluids could be greatly affected by grain surface roughness, in which the adsorbed wetting-fluid films serve as the critical intermediary. It has been demonstrated that the configuration of wetting films is a combination of two competitive surface forces: DLVO adsorption and capillarity, whose effects on wetting fluids can lead to significant changes in the shape of films, and thus distinctive film area under different matric potentials. Therefore, the methodology of the research is to characterize the mechanism of surface roughness involved in the configuration of wetting film, and the resultant change of film area, with an explicit quantitative model.

The main body of the present modeling approach is to use a bundle-of-cylindrical-capillaries (BCC) model for pore geometry that is modified with a surface roughness factor based on the solid surface area. Film-associated interfacial area in the model is represented by an interfacial area factor normalized with solid surface roughness, which is quantified by an explicit sigmoid function (logistic function) that defines the change of film area within the range of two limiting conditions: smooth-surface and maximum roughness. For a given porous medium, its inherent solid phase properties, especially the fractal-scale microstructures of surface roughness,

will generate a characteristic profile of interfacial-area vs. wetting-fluid saturation, which can be fitted from measured data from interfacial partitioning tracer tests (IPTT).

Following the development of modeling approach, simulations with both pre-determined input parameters and actual experimental data were conducted. Example calculations and sensitivity analyses of critical model parameters revealed the phenomenon of "surface roughness masking" that occurred in the interfacial-area vs. saturation curves. Simulation test on experimental data sets for multiple porous media demonstrated the excellent performance of the modeling approach, in which each medium can be explicitly quantified with five critical modeling parameters—two for pore size distribution, one for the sample-scale surface roughness, and two for micro-scale roughness. Inspection of the relationship between roughness-related parameters showed that the micro-scale surface roughness of natural porous media only partially correlate to soil texture. Studies on images from scanning electron microscopy (SEM) also illustrated the complexity of surface roughness. The complicated nature of the micro-scale surface roughness highlighted the potential of the proposed methodology in various environmental applications. It would be particularly useful for systems that comprise large magnitudes of interfacial domain, with energy or mass transport between solid, fluid, and atmosphere.

Key words

Interfacial area; Surface roughness; Contaminant transport; Pore-scale modeling; Porous media

CHAPTER I. INTRODUCTION

1.1 Background

The soil-water-atmosphere interactions are involved in a large amount of environmental processes. A major habitat for the various soil-water-atmosphere interactions is the vadose zone, where matter and energy are continuously exchanged through the hydrological cycle between the outer atmosphere and the groundwater zone. Inside the vadose zone, the different phases (soil, water, air, organic compounds, etc.) are all critical to the fate and transport of substances and contaminants. It is convenient to study the transport processes with respect to specific pairs of the immiscible phases, such as air/water, water/soil, water/NAPL, etc. Studies of many natural processes of mass or energy transport, including adsorption, evaporation, volatilization, interfacial retention, etc., also require identifications of the different phases inside the vadose-zone system.

The conceptual model for a soil-water-atmosphere system treats the problem as the distribution and flow of immiscible fluids inside the porous media of solid. The capillary forces play a major role in the static and dynamic behaviors of fluids. The difference in the capillarity of fluids results in the divergence of wetting and non-wetting fluids. Wetting fluids have a larger affinity to the solid surface of soil, and create the formation of wetting liquid films and capillary menisci. Among typical fluids, water is usually treated as the wetting fluid; air, oil and organic contaminants (such as chlorinated solvents) are usually treated as the non-wetting fluids.

Given the distinctive and characteristic behaviors of wetting and non-wetting fluids, the

interfaces between them are of great significance in various environmental and hydrological disciplines. Over the previous few decades, there are a series of literature that highlights the potential of fluid-fluid interfacial area in the experimental and modeling studies of unsaturated porous media (e.g., Skopp, 1985; Gvirtzman & Roberts, 1991; Hassanizadeh & Gray, 1993; Reeves & Celia, 1996; Costanza & Brusseau, 2000; Pyrak-Nolte et al., 2008). Recently, researchers have shown some specific topics that are highly correlated to the determination of fluid-fluid interfacial areas. For example, the air-water or oil-water interfacial areas have been considered critical to the distribution of soil microbes, and are thus significant in the analyses of microbial activities, such as microbial habitats and the biodegradation of organic contaminants (e.g., Wan et al., 1994; Or, 2002; Johnsen et al., 2005; Or et al., 2007). In the recent years, some emerging contaminants, especially the per- and poly-fluoroalkyl substances (PFAS), highlight the need for determining the interfacial area between wetting and non-wetting fluids, due to the surfactant-like properties of these chemicals (e.g., Lyu et al., 2018; Brusseau, 2018; Brusseau et al., 2019).

The latest trends of researches (microbial habitats, surfactant-like pollutants, etc.) raise the concerns of studying the fluid-fluid interfacial area under the influence of soil, especially the involvement of the grain surfaces (surface roughness) in the fluid-fluid interactions. Therefore, it is of great significance to develop a comprehensive conceptual model that can characterize the mutual relationships between soil, water, air and organic compounds in a vadose zone transport system.

1.2 Objectives

This dissertation aims to develop a model-based approach to associate the nonwetting-wetting interfacial area in porous media with quantified factors of solid surface roughness. The methodology to connect interfacial area and surface roughness is the wetting film. This dissertation presents a quantitative model to parameterize the configurations of wetting films on natural grain surfaces under different hydraulic conditions. This wetting film model can serve as a general approach to quantify the fluid-surface effects for a wide variety of natural porous media.

The present approach employs the concept of fractal geometry in the development of the quantitative expressions for solid surface area and fluid-fluid interfacial area. The approach uses the surface roughness factor and interfacial area factor to parameterize the effects of surface roughness of the wetting films. The small-range methods for surface roughness characterization, such as images from SEM, are also used to verify the approach.

In addition, the approach incorporates an upscaling scheme to generalize the surface roughness-associated wetting film model to any specific type of porous media. Following the scheme, the approach can be applied to the experimental measurements of fluid-fluid interfacial area, and explain the observations in the measured curves. Further, it can parameterize the measured curves into specific surface roughness-associated variables, which can be introduced in a broader scope of applications (e.g., the transport of surfactant-like contaminants such as PFAS).

1.3 Literature Review

1.3.1 Grain Surface Roughness and Its Effect on Porous Fluids

1.3.1.1 Concept of Fractal Roughness

Surface roughness is a ubiquitous property of natural porous media. Due to the development of imaging and metrological technologies, the fractal structures of natural grain surfaces have been revealed. In mathematics, fractal geometry represents the different geometrical features under different observed scales. In a fractal structure (curve or surface), a small range within can contain similar geometrical features after being magnified (self-similarity). Such a structure can be generated through geometrical iterations, in which can be extended to infinity.

Fractal geometry can be used to enlarge the scope of the concept “roughness”. The typical fractal shapes have an important mathematical feature: non-differentiable everywhere, i.e., being “rough” (non-smooth) at any smaller length scale. Traditional expression of surface roughness stems from the statistical data of surface heights. The root-mean-square surface roughness is frequently used in traditional surface metrology, which calculates the root-mean-square average relative height to a reference surface for each measured location in a rough surface. In contrast, the most critical property of fractal roughness is the “fractal dimension” (Hausforff dimension), which describes how a fractal shape deviates from the geometric dimension. For example, a smooth curve is 1D for any straight line or a curve, while a fractal curve is always larger than 1D.

The fractal dimension of a regular self-similar fractal shape (D) can be derived via the following equation:

$$D = \frac{\log N}{\log\left(1/r\right)} \quad (1.1)$$

where N is the number of self-similar pieces, and r is the similarity ratio. For example, the Koch curve (Figure I-1) is a regular fractal shape starting from a line segment. For each iteration, the line is divided into three sections, and the middle section is converted to the two sidelines of an equilateral triangle, which makes four segments in total. Therefore, the fractal dimension of the Koch curve is D = log 4 / log 3 = 1.26.

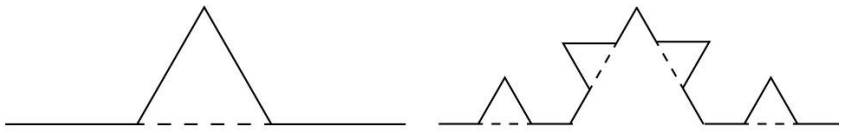

Figure I-1 Illustration of a Koch curve.

For more complicated curves or surfaces, the most common method to calculate the fractal dimension is the box-counting method, in which uniform square or cubic boxes are placed on the fractal shapes to fully cover all of the curves or surfaces. Similar to equation (1), the fractal dimension is the ratio between logarithms of the number of boxes and the reverse box size.

The fractal dimension can show different aspects of roughness compared with the root-mean-square roughness. Theoretically, a mathematically “smooth” surface (differentiable everywhere)

can still have root-mean-square roughness, as long as any points within have different vertical difference compared to a reference height. An imaging simulation in Figure I-2 illustrates a specific case that two surfaces with the same root-mean-square roughness, but different fractal dimensions $D = 2.5$ and 2 (Brown, 1989). These results show that fractal properties provide another perspective of surface roughness compared to the root-mean-square surface height.

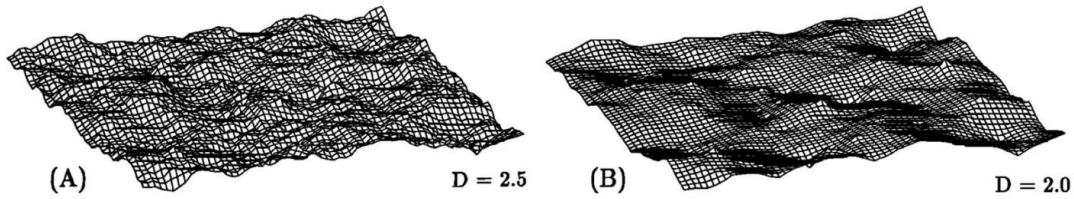

Figure I-2 Examples of two rough surfaces with the same root-mean-square roughness but different fractal dimensions (after Brown, 1989).

1.3.1.2 Surface and Interfacial Area Factor

Given that surface roughness of natural grain media comprises multiple facets of characteristics, it is suggested to propose an indicator to better clarify how "rough" a surface is. As is shown in Figure I-2, a surface can be defined as "smooth" based on its mathematical features ($D = 2$), but still have a considerable relative roughness compared to a reference height. The fractal dimension D is the direct characteristic that represents the fractal complexity. However, equation (1.1) is only applicable for strictly self-similar fractal iterations, i.e., each iteration follows equal pattern (equal shapes and similarity ratio). Real images of natural grain surfaces show that the

fractal structures can be more complicated, which requires some approximation algorithms to calculate, such as the box-counting dimension, information dimension or correlation dimension, etc.

Conversely, a simpler method to represent the complexity of surface roughness has been proposed long before the establishment of the modern concept of fractal geometry, which quantify the rough surface via a “roughness factor” (Wenzel, 1936). The roughness factor is defined as the ratio of “actual surface area” over “geometric surface area”. This definition reflects the later and famous realization of fractal problems: the “coastline paradox”, which illustrates that measurements on a fractal shape (e.g., coastline) under different resolution scale will generate different results. Therefore, it is proposed to measure one fractal shape, such as a natural grain surface, under different resolutions. The low-resolution scale can serve as the measurement for geometric surface area, and the high-resolution scale can serve as the measurement for actual surface area. This concept is also called “rugosity” in some cases to differentiate the traditional denotation of surface roughness.

In soil science, the low and high resolution scales for the soil specific surface area can be achieved through different experimental approaches. The geometrical estimation methods via particle or pore sizes typically give the specific surface area without surface roughness. In addition, images from X-ray computed microtomography (CMT) usually have a minimum resolution limit at micrometers, which also surpasses the magnitude of soil surface roughness. In contrast, the molecular adsorption technology, e.g., nitrogen-BET, provides an approach to measure the soil

specific surface area at molecular scales (10^{-10} m). Comparing the measured results from two resolution levels, the surface roughness factor (X), containing the information of surface fractal features, can be derived for any specific porous medium.

Furthermore, the concept of "actual area / smooth area" can be generalized to fluids, especially to the wetting films in porous media. As is stated in this section, wetting films on natural grain surfaces are held by both the DLVO adsorption and capillary forces, resulting in uneven wetting-nonwetting interfaces (Figure I-3). Similar to the solid surface roughness factor, an "interfacial area factor" (X_a) can be defined as the ratio of the uneven interfacial area over the same geometrical base area. The adsorption/capillary mechanism for wetting films can also predict the theoretical upper and lower limit for the interfacial area factor: under ultra-dry conditions, only adsorption exists and all water molecules form one monolayer, where $X_a = 1$ and fluid-fluid interfacial area equals to the solid surface area. Conversely, under near-saturated conditions, capillary forces dominate and adsorption is negligible, where $X_a = X$ and the wetting films become flat. Therefore, the interfacial area factor X_a is believed to range only within $[1, X]$. As is shown above, the use of roughness factor is suitable for problems including both solids and fluids (wetting films), since it is convenient to compare their surface or interfacial area on the same geometrical base.

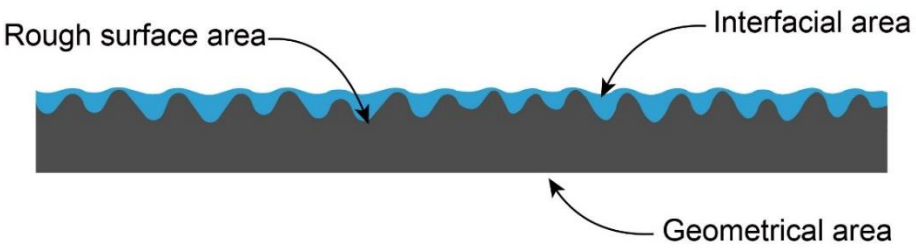

Figure I-3 Illustration of the rough surface area and fluid-fluid interfacial area.

Mathematical definitions and major features of the three mentioned representations of surface roughness (relative surface height, fractal dimension, and area factor) are summarized in Table 1.1.

Table I-1 Summary of the representations of surface roughness

	Relative surface height	Fractal dimension (box-counting)	Area factor
Illustration	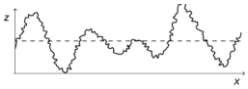	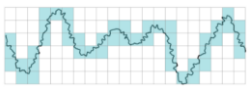	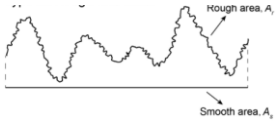
Mathematical definition	$R_{rms} = \sqrt{\frac{1}{n}\sum_{i=1}^{n} z_i^2}$ a	$D = \lim_{\varepsilon \to 0} \frac{\log N(\varepsilon)}{\log \frac{1}{\varepsilon}}$ b	$X = \frac{A_r}{A_s}$ c
Predominant scales[d]	Primary scale (μm)	Primary and further scales (μm to nm), depending on the size of boxes.	Primary and further scales (μm to nm), depending on the resolution of two scales.
Measurement	Direct (from surface profile)	Direct (from surface profile)	Direct (from surface profile) or indirect (from measurements of surface or interfacial areas)

Source of uncertainty	• Area of measured region. • Scale of measurement.	• Box size. • Box counting algorithm.	• Accuracy of measurement. • Validity of pore geometry.

[a] z: surface height coordinates.
[b] ε: box size. N: number of boxes.
[c] A_r: rough surface area. A_s: smooth surface area.
[d] Based on the scale of grain surfaces of porous media.

1.3.1.3 Characterization of Grain Surface Roughness

As is discussed in previous sections, surface roughness of natural grain media can be quantified in three approaches: relative surface height (root-mean-square roughness), fractal dimension, and surface roughness factor. Section 1.3.1.2 gives an experimental approach to estimate the magnitude of the surface roughness factor: taking the ratio of the nitrogen-BET specific surface area over the geometrical (smooth-sphere) surface area via particle or pore sizes (or CMT). In practice, there are more accurate methods to measure surface roughness in a given space, typically by measuring the three-dimensional coordinates of each points in a given space from a rough grain surface. Then, relative surface height, fractal dimension and the rough surface area used for surface roughness factor can all be calculated through geometrical and statistical treatments of the coordinate data.

In soil science, there are two common surface metrological methods to capture the information of surface coordinates: probe methods, including optical profilometer and atomic force microscopy (AFM), and image or photogrammetric methods, usually via pictures from scanning electron microscopy (SEM). The probe methods can directly generate the surface roughness profile as

relative heights for a surface. There are contact or non-contact (pseudo-contact) types of probes. Traditional contact probe uses a mechanical stylus in contact with the sample and moves laterally across the sample surface. For natural grain surfaces whose surface heights can vary to a large extent, it is recommended to use non-contact probes, such as optical profilometers. The pseudo-contact probe, e.g., atomic force microscopy, is also suggestive in the cases for the fine structures of surface roughness at nanometer level.

Compared to the probe methods, SEM image methods are superior in obtaining a comprehensive view of the grain surfaces at flexible resolution levels, which are convenient to incorporate the concepts and algorithms for fractal dimensions. The principle of image methods is to extract the three-dimensional information of surfaces from their two-dimensional SEM images, which is called photogrammetry or 3D reconstruction. There are two basic approaches to conduct 3D reconstructions: single-view or multi-view. Single-view methods typically employ the relationship between brightness and the incident angle of electron beam, which is also called "shape-from-shading" (SFS). Multi-view methods are usually achieved by taking two or more SEM images of the same surfaces with different angle of projection. The 3D coordinates in different SEM images can be reconstructed through stereo matching, which applies a certain algorithm to find the matching points of two images with different angle of view, and then calculate the height of the targeted point from geometric relationships. Between the two methods, single-view methods are straightforward, but may be insufficient in accuracy for images with hard edges; multi-view methods can provide more flexibility, but the interpolations in point-matching

algorithms may also limit its accuracy (Yan et al., 2017). There are also hybrid methods that combine the algorithms from single-view and multi-view reconstructions to achieve the best results in detail (Beil & Carlsen, 1991; Yan et al., 2017).

It is noted that either probe or image methods are only capable of characterizing the surface roughness data for a limited spatial area (field of view), typically on the surface a single grain particle. For natural porous media, the comprehensive surface properties may be more complicated and vary among different grains. Therefore, sample-scale measurement methods, such as the nitrogen-BET measurement for the specific surface area, are also necessary to characterize the surface roughness properties for a whole soil.

1.3.1.4 Surface Roughness Effect on Fluid Configuration and Flow

As an essential property, surface roughness and its effects on fluid configuration and flow have been studied for a long history in surface physics and chemistry. The relationship between surface roughness and the wetting behaviors of fluids is a critical factor in the research of surface roughness effects. However, due to the complexity of surface roughness in natural grain surfaces, there are at least three different viewpoints to conceptualize it: relative surface height, fractal dimension and surface roughness factor. Besides, there are also other experimental or modeling approaches to measure and quantify surface roughness and its effects on soil hydraulic

properties. This section will provide a brief literature review on the studies of surface roughness effects on fluid configuration and flow in small natural surfaces or natural porous media.

Early researchers were interested in the relationship between surface roughness and surface wettability (Adam & Jessop, 1925; Cassie & Baxter, 1944; Oliver et al., 1980; Wenzel, 1936). It was observed on flat surfaces that mechanically rougher surfaces have greater difference between advancing and receding contact angles (Adam & Jessop, 1925). Then, Wenzel (1936) stated that wetting properties should be inherent for a solid substance, and should be directly proportional to surface roughness. Cassie & Baxter (1944) extended the study between surface roughness and wettability to porous surfaces and formulated the relationship between surface roughness (given by surface roughness factor) and contact angle. Researchers in the following decades focused on demonstrating the surface roughness effect on wettability that could induce contact angle hysteresis between drainage and imbibition (Dullien et al., 1989; Huh & Mason, 1977; Morrow, 1970a; Shuttleworth & Bailey, 1948). However, early research of surface roughness effects on porous fluids were limited by the characterization of real grain surfaces, among which only idealized surface models were employed. It was not until the development of sophisticated surface metrological technology, such as laser profilometer and scanning electron microscopy (SEM) was the grain surface roughness able to be precisely measured for the study of its effect on porous-media fluids and hysteresis phenomena (Oliver et al., 1980; Tokunaga et al., 2003).

Surface roughness effect on flow was raised into concern in 1ate 1970s to 1980s with the increasing focus on the adsorbed wetting film and film flow on fractured rock surfaces.

Researchers realized that film flow on a rough surface was influenced by the combination of surface adsorption and capillary condensation (Bachmann & Van Der Ploeg, 2002; Hirasaki, 1991; Philip, 1977, 1978). At the time, fractal theory was also introduced with a novel perspective on the representation of surface roughness and a more sophisticated equation for flow on fractured surfaces (Brown, 1987, 1989; Majumdar & Bhushan, 1990; Schwartz et al., 1989; Thompson & Brown, 1991). Experimental studies of film flows on rough fractured surfaces were later developed with direct measurements on the matric potentials, hydraulic conductivity and surface roughness properties (Fourar et al., 1993; Rangel-German et al., 2006; Tokunaga & Wan, 1997).

In late 1990s to 2000s, Or and Tuller proposed a series of studies with the introduction of wetting film model into porous media using the bundle-of-cylindrical-capillaries (BCC) method (Tuller et al., 1999; Or & Tuller, 2000; Tuller & Or, 2001,2005). Their approaches generalized the two-dimensional geometric model of interaction between surface roughness and porous-media flows into three-dimensional pore space, and conducted explicit simulations on film flow and corner flow inside porous media. In the recent decades, more sophisticated conceptual models have been reported for the surface roughness impact on both fractured-surface and porous-media flows (e.g., Taylor et al., 2006; Liu et al., 2014; Ghanbarian et al., 2016; Torkzaban & Bradford, 2016).

Another important advance for the study of surface roughness effect on fluid and flow was the measurement or estimation of wetting film thickness. It is possible to directly study the interaction between wetting film and rough surface by comparing the magnitudes of their thickness respectively. Atomic force microscopy was the most common approach to directly measure the

adsorbed liquid film on natural surfaces (e.g., Beaglehole & Christenson, 1992; Basu & Sharma, 1996; Gibson et al., 2007; Gaebel et al., 2009; Kim et al., 2012). Another alternative method to measure wetting film thickness is synchrotron X-ray reflectivity (e.g., Tokunaga et al., 2000; Bohr et al., 2010). In addition, Tokunaga (2011) derived film thickness by normalizing the water volume content to solid surface area, and illustrated that the proportional contributions to film thickness from DLVO surface adsorption and capillary force were subjective to the change of matric potentials. Kim et al. (2012) measured the wetting-fluid thickness on both rough and smooth surfaces (R_{rms} = 330 nm and 1.6 nm, respectively) under confinement with supercritical CO_2, and found that the film thickness on both surfaces was strongly correlated to their surface roughness. Kibbey (2013) simulated wetting film controlled by the Young-Laplace equation on synthesized surfaces extracted from SEM images. By calculating the thickness predicted by DLVO adsorption, he argued that the proportion of capillary could be greater in the contribution of wetting film thickness so that the impact of surface roughness could be reduced, while the interfacial area of wetting film would exhibit little change. Zheng et al. (2015) proposed a novel BCC method to incorporate both film area and film thickness to a simple model of rough surfaces using the representation of roughness factor. Their method provided good prediction of hydraulic conductivity for multiple porous media.

Currently, most published studies on surface roughness effect on fluid and flow focus on traditional hydraulic properties such as soil water characteristic curve and hydraulic conductivity. Literature on film-associated interfacial area is limited, and comprehensive study on the

relationship between film thickness, film area and surface roughness has not yet been implemented on sufficient experimental results. The next section will be a summary of the experimental and simulation studies of fluid-fluid interfacial areas in porous media, with specific focus on the compatibility of surface roughness in current approaches.

1.3.2 Fluid-fluid Interfacial Area

1.3.2.1 Film and Meniscus Interfacial Area

The major governing mechanism of the distribution of nonwetting-wetting interfaces is the existence of two type of interfacial area: film and meniscus. Inside a porous medium, a small amount of wetting phases tends to spread throughout the grain surfaces of soil particles, forming thin films between the bulk non-wetting phases and grain surfaces. In contrast, the remaining bulk wetting phases form the capillary-held menisci against the non-wetting phases within the channels between pores (pore-throats). The two types of wetting behaviors generate the film- and meniscus-associated interfacial areas as in Figure I-4.

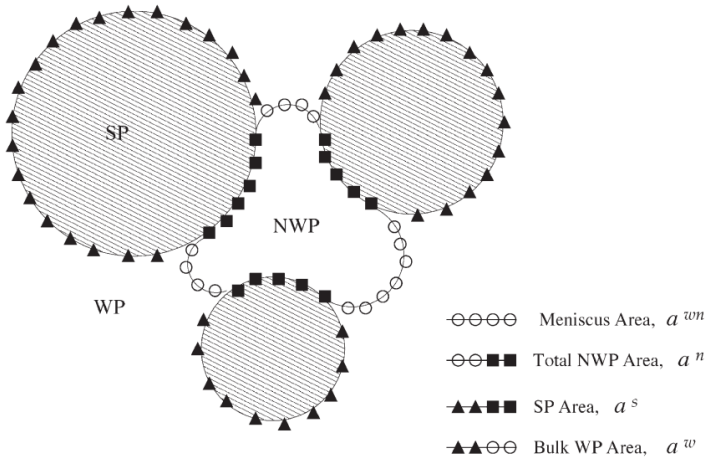

Figure I-4 Scheme of the film and meniscus interfacial area (after Dalla et al., 2002).

It is usually necessary to classify the different types of interfacial area in either experimental

or simulation studies. In addition, some modeling approaches (e.g., the pore network method) may be specified for only the capillary-associated interfacial area. However, a modeling study by Or & Tuller (1999) revealed that film-associated interfacial area surpassed meniscus-associated interfacial area by orders of magnitude. Later on, experimental evidence from the measurement of total air-water interfacial area showed an exponential increase at low saturations, which was attributed to solid surface roughness effects on film-associated interfacial area (Kim et al., 1999; Costanza-Robinson & Brusseau, 2002; Brusseau et al., 2006, 2007). Given film-associated interfacial areas comprise of the vast majority of total interfacial area, it is feasible to treat the measurement of total interfacial area to be primarily associated with the film proportion of interfaces in unsaturated porous media. It is also possible to study and characterize the information of grain surface roughness and its impact on porous-media fluids using the experimental results of fluid-fluid interfacial area.

As is discussed in section 1.3.1, the configuration of wetting film on natural surfaces has been under concern for decades. The competitive forces from DLVO surface adsorption and capillary control the formation of wetting films. Consequently, film thickness and film interfacial area are two significant variables that can be measured from experimental techniques based on the bulk media, and can be corresponded to matric potentials. Recent advances in experiments and simulations have shown that capillary forces play a significant role in the retention of wetting films, which modifies the previous assumption that the wetting films are primarily held by the van der Waals adsorption (Kim et al., 2012; Kibbey, 2013; Zheng et al., 2015). The existence of solid

surface roughness could be a significant source for the surface capillarity. Recent studies on film thickness have also revealed the complexity of the competitive mechanism between surface adsorption and capillary, as the influence of capillary forces can remain strong even at high matric potential (Kibbey, 2013), which implies that there are finer structures of surface roughness that controls the surface capillarity in film fluid. Nevertheless, measurement of film thickness needs to be constrained in relatively small areas for either AFM or other techniques, while interfacial area can be obtained from experiments on a full column of sample materials. Therefore, investigations from the perspective of film-associated interfacial area can provide a more comprehensive understanding on the configuration of wetting fluid on rough porous media under the competitive mechanism of surface adsorption and capillarity.

1.3.2.2 Experimental Methods for Measuring Interfacial Area

Experimental methods to measure fluid-fluid interfacial areas in porous media were developed in the late 1990s. The first series of successful experimental methods were based on soil column tests with interfacial partitioning chemicals, which is called interfacial partitioning tracer test (IPTT). In the early 2000s, another important experimental method: the X-ray computed microtomography (CMT), was developed to obtain the direct images of the structures of a variably saturated porous medium at micrometer-scales. Further, computer-aided algorithms can be applied to the CMT images to calculate the fluid-fluid interfacial area. So far, IPTT and CMT are the two

major experimental approaches to measure interfacial area. Aa brief literature review on the development of both methods is presented this section.

Interfacial Partitioning Tracer Test

The interfacial partitioning tracer test (IPTT) is an indirect method to measure the fluid-fluid interfacial area via the retention behaviors between different chemical agents. A typical miscible displacement experiment for IPTT requires a critical chemical that has strong affinity to the nonwetting-wetting fluid interface, which is called the interfacial partitioning tracer, and a non-reactive chemical as reference. In the test, fluids containing the interfacial partitioning tracer are injected into a packed column with a specific porous medium at a certain saturation (see Figure I-5). The effluent concentrations change over different pore volumes (retention time) of the tracer are then measured, and the fluid-fluid interfacial areas are derived from the degree of retardation from the breakthrough curves of the interfacial partitioning tracer in use.

Depending on the degree of saturation, there are two major types of IPTT systems: gas-phase IPTT and aqueous-phase IPTT. The difference between these two systems is the use of tracers. In gas-phase IPTT, an interfacial tracer gas (e.g., decane) and a non-reactive gas (e.g., methane) are injected and measured (Saripalli et al., 1997; Kim et al., 1999; Costanza & Brusseau, 2000; Costanza-Robinson & Brusseau, 2002; Peng & Brusseau, 2005). In aqueous-phase IPTT, a reactive solute (e.g., sodiumdodecylbenzene sulfonate) and a non-reactive solute (e.g., NaBr) are selected as the target tracers (Kim et al., 1997; Brusseau et al., 2007). In principle, gas-phase IPTT is more

suitable for drier media, and aqueous-phase IPTT is more appropriate for wetter media, depending on the accessibility of interfacial tracers to the fluid-fluid interfaces. Conversely, the aqueous-phase IPTT can be applied to various nonwetting-wetting fluid systems other than air-water, e.g., organic compounds (NAPL) / water systems, wherein gas-phase tracers are unable to be injected

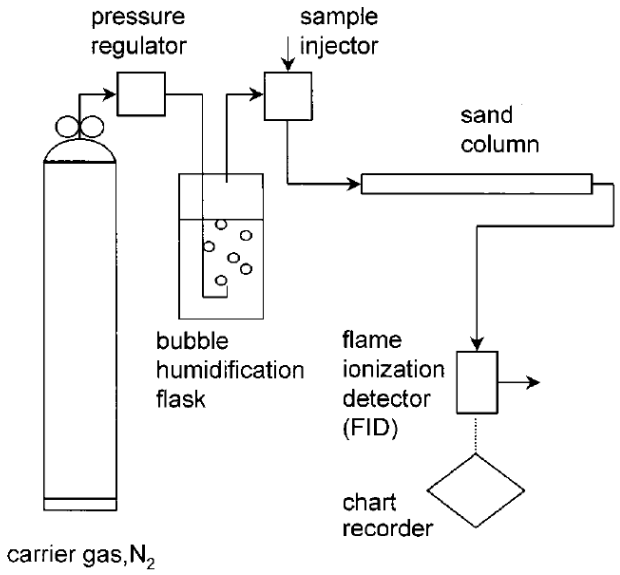

Figure I-5 Scheme of a gas-phase IPTT miscible displacement equipment. (after Kim et al., 1999)

.

Besides the miscible displacement methods, there are also other variations for IPTT setups. For example, the water mobilization method (Karkare & Fort, 1996; Silverstein & Fort, 1997) uses an insoluble surfactant that accumulates at the air-water interfaces. The critical concentration of the surfactant at the onset of water motion is measured to calculate air-water interfacial area. In addition, the drainage and redistribution method injects tracers into the soil column at first until equilibrium, and drains the column to generate a gravity-induced concentration distribution

(Anwar et al., 2000; Araujo et al., 2015; Chen & Kibbey, 2006; Schaefer et al., 2000). Interfacial areas are obtained via adsorption properties and the relationship between surface tension and concentration. In recent years, several novel methods were developed to improve the validity and feasibility of IPTT experiments, such as the dual-surfactant and the residual-air modifications of IPTT (Brusseau et al., 2015) and the gas-absorption/chemical-reaction method (Lyu et al., 2017).

For IPTT, an important challenge is determining the type of interfacial areas that were measured, given that fluid-fluid interfacial areas in porous media exist as either film-associated or meniscus (capillary)-associated. The major limitation in judging the type of areas is the measurable range of saturations. In the miscible displacement experiments, aqueous-phase IPTT is difficult to conduct at lower water saturations (< 40%), while gas-phase IPTT is unable to extend to higher water saturations (> 50%). By combining the measured data from both gas-phase and aqueous-phase IPTT, it has been noticed that the interfacial areas measured at low and high saturations present a large deviation (Kim et al., 1999; Costanza-Robinson & Brusseau, 2002; Brusseau et al., 2007). At lower saturations, the measured interfacial areas increase exponentially, trending toward the solid specific surface area of the porous media (Kim et al., 1999; Peng & Brusseau, 2005; Brusseau et al., 2006, 2007). The deviation between lower and higher saturations was attributed to the accessibility of water flow containing tracers to wetting films (Kim et al., 1997; Costanza-Robinson & Brusseau, 2002). Constaza and Brusseau (2000, 2002) discussed the issue of method-dependent, operationally defined interfacial areas and what they represent in detail, commenting on the importance of tracer accessibility and other issues. Kibbey & Chen (2012) used a pore-

network model to test the measured data from different IPTT approaches, and similarly concluded that the interpretation of type of interfacial area for tracer measurements can be challenging in typical aqueous-phase miscible displacement experiments, as the mechanism of tracer accessibility is unclear.

Brusseau et al. (2007) made a comparison between the results from IPTT and X-ray CMT for the same porous medium. The study extrapolated the measured data points from gas-phase IPTT, aqueous-phase IPTT and CMT to zero saturation. They concluded that the extrapolated maximum interfacial areas from CMT and gas-phase IPTT are close to the specific surface areas estimated by a smooth-spherical assumption, and measured via nitrogen-BET, respectively. In addition, the extrapolated aqueous-phase IPTT value resides between CMT and gas-phase IPTT. They attributed these differences to the resolution of CMT images, and assumed that surface roughness induced the exponential increase in gas-phase IPTT results. Later, Brusseau et al. (2010) compared the inverse median grain diameters, extrapolated maximum interfacial areas in oil-water systems, and the nitrogen-BET specific surface areas of multiple porous media. They found that the three parameters had a strong positive correlation, which demonstrated the role of solid surfaces in the exponential increase of interfacial areas.

The above overview shows that the studies conducted to date have not fully elucidated the relationship between IPTT and the film-associated interfacial area. However, the results indicate that wetting films in porous media are closely connected to solid surface roughness. Meanwhile, film-associated interfacial areas surpass meniscus-associated areas by a large extent at lower

saturations. Therefore, it is promising to use the experimental results of IPTT (especially the gas-phase IPTT) to study the properties of wetting films.

Computed Microtomography

The technology of synchrotron X-ray computed microtomography (CMT) for soil-hydraulic applications was also developed in late 1990s to early 2000s, which exploited a more accurate and explicit approach to directly visualize the 3-dimensional structures of porous media (Coles et al., 1998; Sutton et al., 2002; Wildenschild et al., 2002). Unlike the SEM-based image methods which require vacuum conditions, CMT can be implemented in normal porous media containing liquid and gas. In addition, CMT methods are able to reconstruct the whole porous structures in a broader 3-dimensional range. This advantage makes it possible to visualize the sophisticated shapes and distributions of fluids in porous media.

Wildenschild et al. (2002) compared the images from several X-ray CMT systems, and highlighted the potentials of CMT-based image methods in the applications on the characterizations of hydraulic properties for unsaturated porous media. A series of papers on the applications of CMT in soil studies soon emerged in the following few years. Culligan et al. (2004) then developed a direct method to measure the meniscus fluid-fluid interfacial area in a glass-bead system using CMT images. Later, Schnaar & Brusseau (2005, 2006) conducted CMT image-analyses in oil-water and oil-water-air systems for both sand and soil. Al-Raoush & Willson (2005) improved the image extraction technique to obtain morphological representation of the pore

structures from CMT results. Brusseau et al. (2006, 2007) measured the total and meniscus air-water interfacial area of a natural soil via CMT images, and compared the results with the as-obtained results from gas-phase and aqueous-phase IPTT in section 2.1.1. As mentioned in that section, results from CMT largely deviated from those from IPTT at lower saturations, which was believed to be due to the resolution limit at micrometers in CMT images, and its inability to characterize roughness-associated film area. Costanza-Robinson et al. (2008) proposed an empirical relationship for the interfacial areas and saturations measured in CMT images, and pinpoint the advantages of CMT at higher saturations due to the tracer accessibility in IPTT.

One of the major advantages of image-based method for interfacial area is the clear distinction between total and meniscus (capillary) area. The classification of total, film, and meniscus type of interfacial area has been briefly discussed in section 1.3.2.1. In CMT images, a clear visualization of solids, wetting fluids, and non-wetting fluids can be captured by X-rays (see Figure I-6). Wetting films and capillary-held menisci are also likely to be identified from images. The commonly-used equation to calculate meniscus-associated interfacial area is:

$$A_{wn} = \frac{1}{2}\left(A_w + A_n - A_s\right) \quad (1.2)$$

where A_w, A_n, and A_s is obtained by counting the length of the margin of wetting phases, non-wetting phases and solids, respectively. Wetting films are assumed to present on every solid surfaces. Thus, the film and meniscus area can be treated as the cumulative contact length between nonwetting/solid and nonwetting/wetting, respectively.

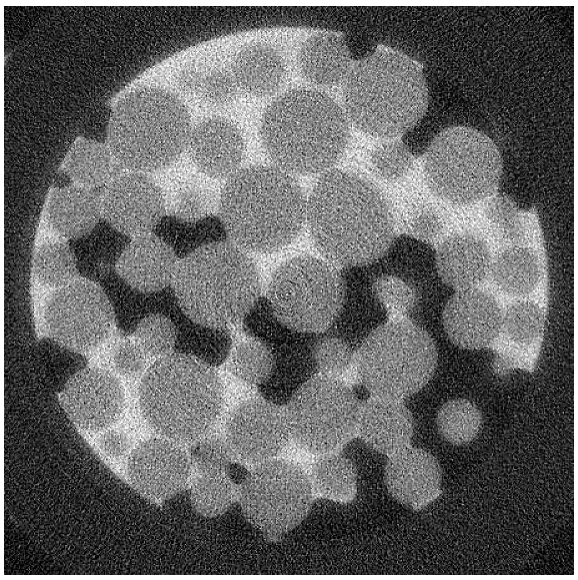

Figure I-6 Cross-section image of a glass-bead medium captured by X-ray computed microtomography (after Culligan et al., 2004).

Image processing is the major threshold for the accuracy of CMT methods used in interfacial areas. CMT images need to be segmented into specific regions for nonwetting, wetting, and solid phases in order to conduct the data analysis. The three-dimensional porous structure with the presence of all films and menisci will be finally generated based on the segmentation. Total and meniscus-associated interfacial areas are also calculated via equation (2). Given the capability of establishing three-dimensional structures, CMT methods are potential to collaborate with other modeling methods (e.g., pore-network or Lattice-Boltzmann) for a more sophisticated reconstruction of the porous structures.

Typical CMT images have a resolution at the magnitude of 10 micrometers (e.g., Culligan et al., 2004; Schnaar & Brusseau, 2006). More recently, synchrotron-based CMT technology has improved the resolution level to below 2 micrometers (e.g., Araújo & Brusseau, 2019). Voxels at

micrometer-scale are able to capture the traditional roughness associated with surface heights, but are still insufficient for the region of the fine levels of fractal roughness (at 1~10 nanometers). In terms of the definitions of surface roughness in section 1.3, the solid surfaces and wetting film interfaces in CMT images may be considered as mathematically smooth.

1.3.2.3 Simulation Methods for Interfacial Area

Prior to the measurement of fluid-fluid interfacial area, models and simulations for this important soil-hydraulic variable has originated for a long period. Early concept of interfacial area in porous media stemmed from the investigation of the thermodynamic behaviors associated with the capillary forces. The total interfacial area between wetting and nonwetting fluids is a critical element to determine the surface work or the change of surface energy. In 1990s, specific models for the porous structures and the distribution of fluids within were developed, including the pore-network models and idealized pore-geometry models (bundle of cylindrical capillaries). In 2000s, new modeling approaches, such as pore-morphology and Lattice-Boltzmann methods also came into use. Meanwhile, traditional approaches (thermodynamic, pore-network, idealized pore-geometry) were also renovated to be adapted in more cases. As an increasing number of experimental data from IPTT and CMT were published, it is likely to understand and predict interfacial areas in unsaturated porous media via comparisons between experiments and simulations.

Thermodynamic Method

The general concept of thermodynamic method for interfacial area originated in an early paper by Leverett (1941). In the basic thermodynamic assumption for a water-wet capillary process in porous solids, the capillary pressure P_c is considered to be the increase of free surface energy dF for per unit volume of water dV that transfers from sand to the water reservoir at the same level, such that $P_c = \partial F/\partial V$. For per unit water transferred out of the medium, the water saturation will equally decrease, making $dS_w = -dV$. Meanwhile, the free surface energy results in the increase of interfacial area dA in the same unit volume of water. The surface tension γ of water follows the equation: $\gamma = \partial F/\partial A$. Therefore, for per unit volume change of water in a porous medium, the changes in water saturation and interfacial area are connected by the change of free surface energy:

$$dF = -P_c dS_w = \gamma dA \quad (1.3)$$

Equation (1.3) can be rearranged to an integral form:

$$A_{nw}(S_w) = -\frac{n}{\gamma}\int_1^{S_w} P_c(s)\,ds \quad (1.4)$$

Here, n is the porosity of soil when interfacial area is expressed as the area in unit volume of soil. $A_{nw}(S_w)$ means the interfacial area at a certain water saturation. For a drainage soil water characteristic curve ($P_c - S_w$ curve) the integral in equation (1.4) means the under-curve area between the certain point and full saturation. Thus, as long as the $P_c - S_w$ curve of a porous medium is measured, its $A_{nw} - S_w$ curve can be directly predicted through the mentioned thermodynamic relationship.

However, due to the lack of experimental techniques, concerns on fluid-fluid interfacial area in the research of soil hydraulic topics only stayed on the stage of theoretical discussions in the following 50 years. Morrow (1970) extended Leverett's method to a detailed mechanism to demonstrate the immiscible displacement in porous media. Hassanizadeh & Gray (1993) noticed the physically unrealistic properties in the standard theories of capillary pressure, and used the mentioned thermodynamic relationship to highlight the significance of interfacial area. As a critical conclusion, they speculated that the normal hysteresis phenomena could be a projection of the $P_c - S_w - A_{nw}$ ternary relationship on the $P_c - S_w$ plate, which arose the discussion on interfacial area other than the traditional topics of soil water characteristics and hysteresis. Later, the general approach using equation (1.4) to obtain the $A_{nw} - S_w$ curve for a specific porous medium was proposed by Bradford & Leij (1997).

In the following decade, there are some studies working on modifying the general thermodynamic equation (1.4). For instance, Dobson et al. (2006) conducted interfacial partitioning tracer tests in an entrapped NAPL-water system with both drainage and imbibition tests. To verify the results, they plotted the drainage and imbibition $P_c - S_w$ curves together, and showed that the under-curve area used in equation (1.4) should be corrected as the area surrounded by the two curves. Grant & Gerhard (2007) modified the general equation (1.4) to calculate the meniscus-associated interfacial area, in which equation (1.4) was multiplied by an empirical saturation-related factor ψ and an "energy dissipation" factor E_d:

$$A_{nw} = -\psi \cdot E_d \cdot \frac{n}{\gamma} \int_1^{S_w} P_c(s)\, ds \quad (1.5)$$

This modification provided good prediction on the measured meniscus-A_{nw} vs saturation curve via CMT images. Schroth et al. (2008) extended the thermodynamic approach for entrapped NAPL blobs by Dobson et al. (2006) on arbitrary drainage-imbibition sequences and improved its performances by considering an "apparent wetting-fluid saturation".

Limitations of the general thermodynamic method have been mentioned in the first paper by Leverett (1941), in which the simple energy balance may not be applicable at all saturations. In addition, the film and capillary-meniscus domains of interfacial area are not clearly demonstrated in the thermodynamic relationship. Nevertheless, as a simple estimation method, the thermodynamic approach was often used to verify the results from other experimental and modeling work (e.g., Dalla et al., 2002; Dobson et al., 2006; Kibbey & Chen, 2012; Diamantopoulos et al., 2016). Preliminary results have shown that the simple thermodynamic assumption is valid at higher saturations. In principle, the basic thermodynamic relationship in equation (1.3) treats the energy exchange between interfaces as driven by capillary pressure. However, wetting films in natural grain surfaces are held by both surface adsorption and capillary forces. At lower saturations where surface adsorption dominates, the simple thermodynamic assumption may be insufficient.

Analytical Pore-Geometry Method (BCC)

Pore-geometric models are widely used in the simulations of soil-hydraulic properties. Among them, the **bundle-of-cylindrical-capillaries** (BCC) model is a highly developed approach to simplify the three-dimensional pore configurations to idealized geometric shapes, which can be conceptualized to two-dimension and quantified into analytical equations. Early BCC representation treated an unsaturated porous medium as a bundle of capillary tubes in different sizes that are filled with wetting liquids. Under a given matric potential expressed as a certain height, each tube has different height of liquid. Saturation is calculated by the area of filled tubes divided by the total area of tubes in the cross-section of that certain height (matric potential) (Markus Tuller & Or, 2004). However, this representation lacks the component of film-associated interfacial area. To make a BCC model work for interfacial area, Cary (1994) considered that all unfilled tubes at the specific matric potential are also coated with wetting films, and proposed an analytical method to predict the interfacial area for some imaginary soils. Oostrom et al. (2001) extended the method to an analytical model with the assumption of "free" and "entrapped" nonwetting fluids, which can calculate interfacial areas from the measured SWC data of porous media. Their estimations matched the measured $A_{nw} - S_w$ data set of glass beads, but presented some deviation to the sandy medium used by Kim et al. (1997).

There are also modeling attempts to modify the pore-space representation of traditional BCC to configure a more realistic formation of wetting films. A significant breakthrough was made by

Tuller et al. (1999) and Or & Tuller (1999), whose work defined each individual pore as a "unit cell". Each unit cell has a central pore in regular shape and two channels at the opposite sides of the pore (see Figure I-7). A partially drained pore has wetting films on the inner walls of channels and central pore, and capillary menisci on the corners of central pore. In the work specified for interfacial area (Or & Tuller, 1999), they assumed that the maximum air-water interfacial area in drainage should be equal to the specific solid surface area (*SA*) of the same soil, by which to estimate the pore-dimension parameters α and β. In their comparisons to measured data, they noted that using typical smooth-spherical *SA* via mean particle diameter would underestimate the interfacial-area curve, which they attributed to the existence of surface roughness. In addition, they calculated the proportions of film and capillary-meniscus interfacial area, respectively, and concluded that film-associated interfacial area could exceeded meniscus-associated area by orders of magnitudes. Likos & Jaafar (2013) proposed a unit cell BCC model based on the geometry of the irregular void space between packed spheres, in which they used the distribution of particle sizes to derive pore size distribution, and then obtain the related soil hydraulic properties including interfacial area, but they only included meniscus-associated interfacial area.

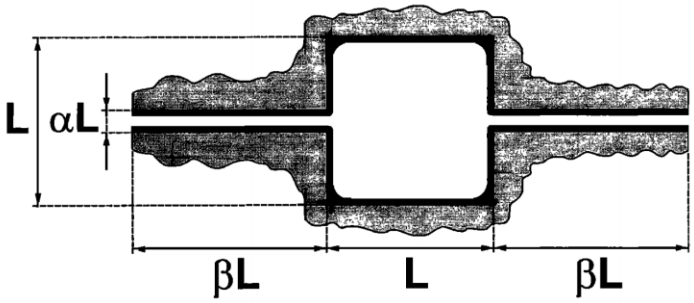

Figure I-7 BCC variation using a modified unit cell model (after Or & Tuller, 1999).

There is yet another BCC variation of pore geometry: the triangular pore space model (TPSM). In TPSM, the entire porous medium is treated as a bundle of triangular cylinders, where the wetting fluids are continuously distributed alongside of pore walls (see Figure I-8). Unlike the traditional BCC, TPSM-BCC provides a more realistic representation of wetting films and menisci: films are attached to the pore walls, and menisci are distributed to each pore corners. Both film and meniscus can move along the axial direction of cylindrical tubes, which makes TPSM approaches convenient to treat unsaturated flows. Besides, TPSM is also highly compatible with the as-mentioned surface roughness factor and fractal dimension in section 1.3.1.2. In literature, Helland & Skjaeveland (2007) applied TPSM for meniscus-associated interfacial area for a mixed-wet (water-oil) system and simulated primary and secondary drainages and imbibitions in their model. Their simulation verified the contact-angle hysteresis in the $P_c - S_w - A_{nw}$ ternary relationship. Diamantopoulos & Durner (2013) added adjustable contact angle to the geometric distribution of wetting fluid in TPSM for meniscus interfaces. In their follow-up work (Diamantopoulos et al., 2016), they used the model to test on the measured interfacial areas of different porous media. They found that an apparent contact angle greater than zero was necessary to compensate the measured meniscus interfacial area data for glass beads, while it was negligible for natural sand and soil.

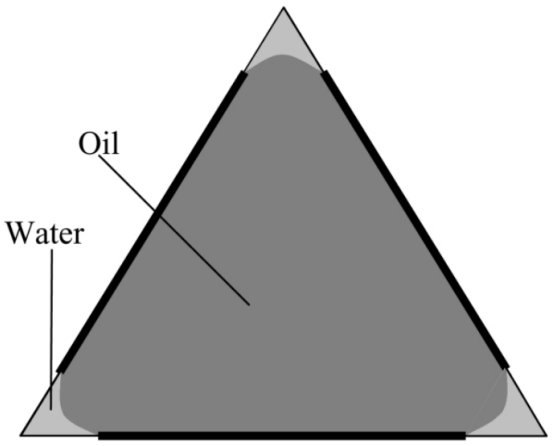

Figure I-8 Single pore with oil and water in the triangular pore space model (after Blunt, 2001).

Numerical Methods

Since natural 3D porous structures are complicated, a useful solution to simulate the fluids and flows is to use computer algorithms to generate an artificial structure, and then simulate the fluid distribution based on physical constraints such as the Young-Laplace equation. One of the most prevalent numerical-based methods is the **pore-network** model, which also uses idealization of the pore structures. The major difference between pore-network models and BCC models is the upscaling treatment from single pore to sample scale. In BCC models, upscaling is implemented by presuming a statistical distribution (gamma, lognormal, etc.) of pore sizes; conversely, pore-network models use specific algorithms to generate the pore structure with respect to the coordinates of each pore, and automatically build up the channels between pores. In pore-network models, a great advantage over idealized BCC methods is the full consideration of connectivity with the intersected channels, which is capable of simulating more sophisticated fluid distributions

(especially the wetting fluid menisci) and the dynamic flow patterns in porous media. However, consideration of film-associated interfacial area is not yet common in pore-network models based on this literature review.

Reeves & Celia (1996) first applied a pore-network model on interfacial area, in which they studied the $P_c - S_w - A_{nw}$ ternary relationship with respect to the hypothesis by Hassanizadeh & Gray (1993). They generated a regular 50 × 50 × 50 lattice with pore bodies and pore throats (channels), and specified the locations nonwetting-wetting menisci associated with drainage and imbibition. Their $P_c - S_w - A_{nw}$ ternary curves behaved consistently smooth, which indicated that $A_{nw} - S_w$ curve can be predicted from $P_c - S_w$ results. Gladkikh & Bryant (2003) improved the representativeness of pore-network by using a randomly-packed-sphere system with the known coordinates of each sphere. They simulated the interfacial areas during imbibition, especially the pore snap-off process and the entrapment of nonwetting phase, but found that the imbibition A_{nw} curves were not sensitive to these considerations. Then, Bryant & Johnson (2004) added the assumptions of wetting films and pore connectivity to the pore-network model, and illustrated that pore connectivity was significant for the determination of both total and meniscus interfacial area at lower saturations. Joekar-Niasar et al. (2008, 2010, 2012) published a series of papers with modified pore-network models and algorithms that can simulate the dynamic or non-equilibrium processes for the $P_c - S_w - A_{nw}$ relationship during drainage and imbibition, but their work were also specified for the meniscus-associated interfacial areas. Kibbey & Chen (2012) used a regular pore-network model that incorporated film-associated interfacial area in order to simulate the

adsorption of tracers in different types of IPTT experiments.

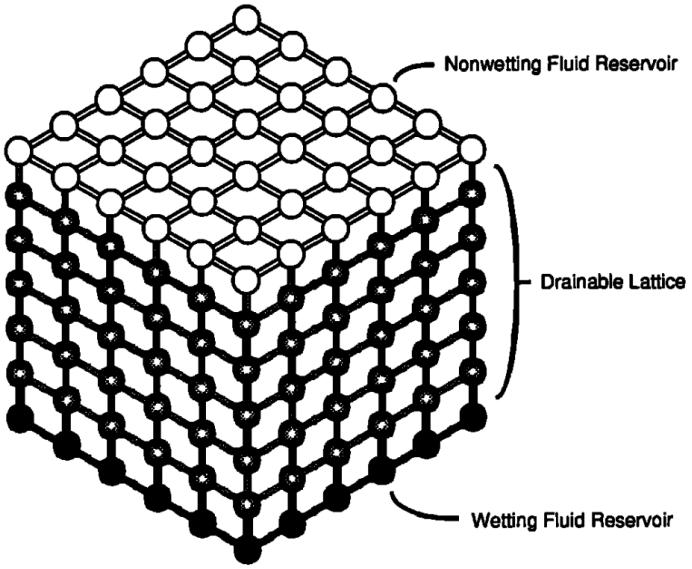

Figure I-9 Idealized cubic pore network used for interfacial areas (after Reeves & Celia, 1996).

Pore-network models are able to delineate the sophisticated shapes and locations of the capillary-held menisci using the geometric configuration of pore throats and pore bodies, which makes them the most common and effective approaches to simulate the behaviors of capillary menisci. However, treatment of film-associated areas could be problematic as the geometry of pore throats and bodies is seemingly idealized. Current pore-network models with wetting film (e.g., Gladkikh & Bryant, 2003; Kibbey & Chen, 2012) typically assume all void space within the network to be coated with wetting films. Nevertheless, since the magnitude of film-associated area at lower saturations can be much larger as indicated by BCC model, the representation of wetting films in pore-network models are still insufficient to reflect the realistic trend.

As BCC and pore-network models all require necessary simplifications in the pore structure,

alternative approaches to directly simulate the real pore-space information were developed over the past few decades. The method using an artificial pore-space generated by randomly-packed spheres and directly simulating the fluid configurations inside is called **pore morphology** method (Hazlett, 1995; Hilpert & Miller, 2001; Vogel & Roth, 2001). The major challenge in pore morphology models is to simulate the distribution of fluids under the constraint of physical laws such as the Young-Laplace equation in a realistic mapping of pore morphology. In the realm of interfacial area, Dalla et al. (2002) developed the first pore morphology model to calculate the quasi-static interfacial area curves in a digital porous medium generated by randomly-packed spheres. Their model was based on the pore-morphology-based fluid simulator by Hilpert & Miller (2001) to establish the wetting and nonwetting fluid regions, and used the standard marching-cube algorithm to compute interfacial areas. Their results were compared with multiple sources of interfacial-area data, including data from IPTT, the thermodynamic approach, and the pore-network-based approach by Reeves & Celia (1996), which were illustrated to reside somewhat between the results via IPTT and thermodynamic approach. Surface roughness was not included in their work, but they assumed that it had little impact on the results at $S_w > 0.2$. Chan & Govindaraju (2011) extended the pore-morphology model to include the entrapment of wetting and nonwetting phases and further simulations of drainage-imbibition scanning curves. They also improved the computation of interfacial area by using a voxel-based area estimator in place of the marching-cube algorithm.

More recently, Porter et al. (2009, 2010) employed the Lattice-Boltzmann method (LBM) on

high resolution CMT images to compute interfacial area, which opened a new pathway to make use of the realistic pore geometry. In their LBM, the physical constraint (Young-Laplace equation) was realized via a different principle from the pore morphology method, which was defined in the form of "interaction potential" between lattices. The model was implemented by balancing the fluid-fluid cohesive forces and fluid-solid adhesive forces between individual lattices. McClure et al. (2016) conducted LBM in a randomly-packed-sphere system to study the phase connectivity impact on the $P_c - S_w - A_{nw}$ relationship. Typical LBM simulations require a high volume of computations on the lattice equations. For example, Porter et al.'s CMT-based simulation took 1.25 days to run in a parallel-on-four CPU for a lattice domain containing 7 million voxels. McClure et al.'s simulation reduced the lattice domain to 43 thousand equations.

Comparison of Modeling Methods

As this dissertation focuses on the connections between interfacial area and surface roughness, the potentials for modifications with surface roughness in current models are of great interest. In this section, we make a brief comparison of all of the mentioned modeling approaches (Table 2.1), including their features (advantages and disadvantages) and their compatibility with surface roughness modifications.

Table I-2 Comparison of modeling methods for interfacial area and their compatibility with surface roughness modifications.

Method	Features	Compatibility of Surface roughness properties
Thermodynamic	• Analytical equations. • Depend on the measured $P_c - S_w$ data. • Can calculate meniscus-associated A_{nw} through an empirical relationship. • Not applicable at lower S_w.	• Surface roughness is contained in principle, but is probably very limited.
BCC	• Analytical equations. • Can simulate both P_c and A_{nw} curves in most cases. • Clearly differentiate film and meniscus. • Idealized pore geometry. • Easy to be modified (contact angle, imbibition, entrapment, etc.) • Lack pore connectivity.	• Not included in the original models. • But very convenient to be modified. Surface roughness can be directly transformed to quantified parameters. • Methodology has been reported in literature.
Pore network	• Require numerical treatment. • Can simulate both P_c and A_{nw} curves. • Idealized pore geometry. • Consider pore connectivity. • Well designed for the dynamic simulation of drainage and imbibition. • Film and meniscus are not well distinguished.	• As film area seems to be ambiguous in literature, the methodology to include surface roughness is not well discussed.
Pore morphology	• Require numerical treatment. • Can simulate both P_c and A_{nw} curves. • Realistic pore geometry.	• Literature records are all based on smooth spherical media. The scale of surface roughness is limited by the

	• Can generate the real-time images of porous media. • Use computer-aid image processing technique to calculate A_{nw}. • Film and meniscus can be differentiated. • Based on smooth spheres.	size of pixels or voxels.
Lattice Boltzmann	• Require numerical treatment. • Can simulate both P_c and A_{nw} curves. • Realistic pore geometry. • Start directly from the CMT image of real pore structures. • Use computer-aid image processing techniques to calculate A_{nw}. • Film and meniscus can be differentiated. • Require a huge magnitude of computations (usually over one day).	• The scale of surface roughness is limited by the resolution of CMT images. • Could be exerted to the model as an imaginary magnification of the areas in the image under specific conditions of P_c.

CHAPTER II. PRESENT STUDY

2.1 Dissertation Format

This dissertation contains two major chapters and four appendices. Chapter I is an introduction of the body of research, with an emphasis on two core topics in this dissertation: surface roughness and interfacial area. The chapter provides an overview of the background of the two topics, and a comprehensive literature review. The literature review has a particular focus on the potential connections between surface roughness and interfacial area based on the available results on experiments and simulations.

Chapter II is a summary of the major findings of the research presented in this dissertation. This chapter briefly discusses the development of surface roughness model for interfacial areas in porous media, which is the most significant contribution proposed in the dissertation. An overview of simulation results and major findings is also presented with respect to each manuscript given in the following Appendix section.

In the Appendix section, Appendix A and B are submitted manuscript to peer-review journals, which comprise of the main body of the modeling studies for this dissertation. Appendix C is a short article on one of the potential practical application of the proposed model – focusing on a type of emerging contaminant: per- and polyfluoroalkyl substances (PFAS). Appendix C provides a specific environmental perspective of the ongoing modeling studies, which highlight the contribution of this dissertation to current practice of environmental engineering and remediation.

Appendix D is the codes for MATLAB that is used to implement the model.

2.2 Summary of Results

The major body of the ongoing research for this dissertation is the development of an explicit model that is able to incorporate quantitative representation of surface roughness into current pore-space model used for interfacial area. Comprehensive experimental data from published papers are employed to test the performances of the model, and then to extend the scopes for model applications. The following contents are a summary on how the model is developed, and how the model can be validated and extended by existing experimental works.

2.2.1 Appendix A – Pore-Scale Modeling of Fluid-Fluid Interfacial Area in Variably Saturated Porous Media Containing Micro-Scale Surface Roughness

This manuscript developed a full modeling methodology to simulate nonwetting-wetting interfacial area in porous media under the influence of grain surface roughness. Solid surface roughness was realized by the representation of an area factor defined as the ratio of N_2/BET specific surface area over surface area estimated from pore geometry. The interfacial area of wetting film under the involvement of DLVO adsorption is also expressed by the interfacial area factor. The model quantitative the relationships of both film area and film thickness as a function of matric potential. Specifically, the equation for film area was given by a new logistic function,

which introduced explicit parameters that could be particularly associated with the fractal geometry of surfaces.

The sample-scale model was established upon the bundle-of-cylindrical-capillaries (BCC) method for the realization of pore space, in which each single pore is treated as an equilateral triangle following a lognormal distribution. Each specific sector in drainage or imbibition (fluid configuration in a pore, contact angle, critical pore size, air entry) was defined or discussed in the upscaling approach. Contributions from filled pore, corner fluid, and film fluid were derived for the final equations of sample-scale saturation and interfacial area (film and meniscus).

A sample calculation was conducted to illustrate the proportional contribution of each component in saturation and interfacial area. Sensitivity analysis on the surface roughness factor and pore size distribution was also given as illustrations of the impact of primary modeling parameters on interfacial-area profiles. Comprehensive experimental data sets from three porous media were then applied for the calibration of model parameters. The BCC model with surface roughness parameters showed good performance on real experimental data of total interfacial areas especially at low saturations, which had not been achieved by previous modeling studies. See Figure 7 in Appendix A.

Based on the simulation results, a significant finding was that the effect of grain surface roughness could be masked by the thickness of wetting film under specific conditions. The masking phenomenon corresponding to matric potentials was controlled by the micro-scale nature of surface roughness, and could be quantified by the proposed logistic function for film area factor.

Given the feasibility of BCC model in the experimental data of interfacial area, the methodology promises plenty of outlooks on environmental studies involving solid-fluid interactions. The modeling approach presented can be used to characterize a broad range of porous media with different solid surface structures. The generated surface-film characteristic can serve as a quantitative approach to characterize rough surfaces, and simulate the associated wetting films in pore-space modeling. This approach is anticipated to provide additional insight into surface roughness effects on porous-media systems.

2.2.2 Appendix B – Characterization of the Micro-scale Surface Roughness Effect on Immiscible Fluids and Interfacial Areas in Porous Media Using the Measurements of Interfacial Partitioning Tracer Tests

Based on the modeling methodology developed in Appendix A, this manuscript aimed at further examining the performance of the surface roughness–modified interfacial-area model for more porous media and more conditions. The manuscript focused on elucidating the nature of micro-scale grain surface roughness and how they could be reflected by the hydraulic behaviors of unsaturated porous media. The surface roughness effect on immiscible fluids was illustrated in typical $A_{nw} - S_w$ profiles as how the actual A_{nw} curves reside between two limiting curves, which was called “surface-fluid triangle” for the triangular shape surrounded by the two limiting curves (see Figure 1 in Appendix B). The limiting curves were the smooth-surface curve controlled by

the pore size distribution of solid media, and the maximum-roughness curve that incorporates the surface roughness factor. Theoretically, these two curves indicated that wetting films were held by only surface adsorption and only capillary, respectively. As the two limiting curves represented the free space for change of roughness (or fractal dimension) of a specific solid medium, characterization of grain surface roughness and its effect on fluids was realized by quantifying the change of film areas in the actual A_{nw} curve of the medium. The logistic function and its parameters proposed in Appendix A were demonstrated in detail in this manuscript, as it defined the quantitative pattern for the fractal iterations of a rough surface from the beginning as smooth surface to the scale of molecules.

The BCC-based modeling methodology was also implemented on experimental data from interfacial partitioning tracer tests, in which a total of five porous media were used to obtain the model parameters for each, especially the logistic parameters associated with micro-scale roughness. Sample-scale properties and the micro-scale surface roughness parameters were evaluated for potential relationships. Visual analysis of the SEM images of the selected porous media reinforced the results generated from model simulations, and validated the representation of micro-scale roughness defined in the model. In addition, the model was conducted on a data set of NAPL-water measurement, and provided good prediction of NAPL-water interfacial area from the fitted model parameters.

This study extended the potentials of measurements of fluid-fluid interfacial areas for natural porous media. Each porous medium has an inherent surface-fluid triangle and an interfacial area

profile containing the information of meso and micro–scale surface roughness. The BCC-based pore geometry model provides an approach to characterize surface roughness from sample-scale measurements (IPTT), which compensates the disadvantages of smaller measurable areas of traditional methods such as SEM and AFM. Characterization of the surface roughness effect from an interfacial area profile provides an experiment-simulation combined approach to analyze the configuration of wetting film and related environmental processes involving significant surface-fluid interactions.

2.2.3 Appendix C – Case Study: Modeling the Vadose Zone Transport of PFAS

This section is a brief feasibility analysis of one potential environmental application of the proposed model in this dissertation—the vadose zone transport of per- and poly-fluoroalkyl substances (PFAS). As a group of emerging contaminants of increasing concern, PFAS can be retained at either the fluid-fluid interfaces or be adsorbed to the solid surfaces in soils (Brusseau et al., 2019). The multi-phase partitioning and retention behaviors of PFAS provide a good example to employ the modeling methodology with the explicit characterization of surface-fluid interaction for a specific porous medium. Therefore, this section presents a brief discussion of the feasibility of generalizing the calibration-based modeling approach to a comprehensive environmental problem. The section contains the major theoretical equations derived from the

two manuscripts above. Future work of detailed simulations can be implemented under the guidance in the article.

The transport and retention model for PFAS was developed primarily upon the equations for saturation and total interfacial area in Appendix A. The manuscript has shown that the soil medium of the contaminated site can be parameterized into five critical variables (L_m, σ, X, k, h_m) from IPTT measurements. The unsaturated hydraulic conductivity of soil can also be derived from the proposed $P_c - S_w$ relationship. In addition, the inherent solid-phase parameters can determine the solid-fluid interactions for multiple fluids by simply adjusting the interfacial tension between fluid pairs. It can be also generalized to the three-phase-fluid (air/NAPL/water) system. Given the saturation-controlled relationships for interfacial area and hydraulic conductivity, the transport equations for PFAS can be derived from the typical Richards equation for soil water content, and the advective-dispersion equation for the transport of contaminant. The interfacial transport and retention of PFAS is represented by a retardation factor in the advective-dispersion equation.

Therefore, it is elucidated that a transport model for interface-active contaminants such as PFAS is feasible to establish starting from the measured inherent properties of soils. Besides PFAS, the model may be expected to have unique capability in some situations where film fluid is more significant (such as microbial habitats).

2.2.4 Appendix D – Example MATLAB Codes for Model Application of a Given Medium

This is an appendix of the MATLAB codes to conduct the proposed model for a given porous medium. The necessary input variables (as single numbers or as vectors) in MATLAB have been marked in the annotations. Typically, required input data include the measurement of $P_c - S_w$ function (soil water characteristic), the specific solid surface area via N2/BET, and the gas-phase IPTT data for air-water interfacial area (aqueous-phase IPTT may be also used). Function files in MATLAB (.m files) are listed ahead of the main body of codes.

To run the code in MATLAB, it is suggested to conduct a trial test on the $P_c - S_w$ data with a small value of X in the "main codes" file, and then input the fitted results of L_m and σ in the "surface area" file and manually adjust the actual value of X to match of specific surface area via N2/BET. With this value of X as the input in the "main codes" file, the fitted results for $P_c - S_w$ and $A_{nw} - S_w$ can be generated and all significant parameters can be obtained.

2.3 Conclusions and Future Work

The dissertation developed a full methodology to simulate the fluid-fluid interfacial area with an explicit model of the surface roughness effect on wetting fluid. The representation of surface roughness and the resultant impact on wetting fluid took advantage of the more sophisticated surface roughness model, such as the fractal geometry of natural rough surfaces,

which surpassed the capability of traditional relative surface height. The proposed logistic function for the changing film interfacial area was proved feasible from simulation results, which provided an effective quantitative approach to delineate the competitive film-holding mechanism between DLVO surface adsorption and capillary force. The two competitive forces create a "surface-fluid" triangle, and an inherent interfacial-area profile controlled by the micro-scale surface roughness of porous media.

A large number of simulations with either pre-determined or lab-measured input data have been conducted to examine the performances of the model. The sensitivity of all the five critical parameters—L_m, σ, X, k, h_m —on the output of $P_c - S_w$ and $A_{nw} - S_w$ curves has been thoroughly investigated. In addition, a total of five natural porous media have been used for model applications on actual experimental data via IPTT. Simulation results showed reasonable sensitivity profiles for each parameter, as well as good match to the experimental data in the full saturation range upon parameteric optimization, while other traditional approaches (e.g., the thermodynamic method) failed.

Further analysis on simulation results revealed more interesting findings. For instance, the predominant contributors to the $P_c - S_w$ and $A_{nw} - S_w$ functions were different, meaning simulations for both curves were highly independent. This phenomenon helped in minimizing the uncertainties of optimization. Comparison with surface SEM images provided visual examples of the complexity of natural grain surface roughness. Thus, the importance of

conducting interfacial-area measurements in the study of soils and porous media was highlighted.

The development of model in this dissertation incorporates a number of simplifications and idealizations, and possessed some limitations at the current stage. For example, the BCC-based pore geometry may overestimate the magnitude of total specific surface area, which has been observed from the simulation result of one sample medium. However, the general approach for the surface-film interaction model is compatible with more sophisticated pore-space representation. One potential variation of model methodology is using the actual pore-space images from X-ray microtomography, and exerting the surface-film model via more accurate computations such as the Lattice-Boltzmann method. In addition, the model also can be modified to incorporate factors such as non-zero contact angle, imbibition cycle, and residual saturation. It will be interesting to analyze the impacts of these variables in future work to generate the comprehensive profile for the film-area-response to specific physiochemical properties.

Finally, as is briefly introduced in Appendix C, the application of the methodology to one specific practical case—PFAS transport has been evaluated. The results indicated the feasibility of the model for this problem. More practical-oriented works of the model can be undertaken for environmental processes involving the transport phenomena between solid-liquid-atmosphere interfaces. Overall, the research developed herein is anticipated to contribute to our understanding of fluid-solid interactions for natural porous media, and how they impact the configuration and magnitude of fluid-fluid interfaces.

REFERENCES

Adam, N. K., & Jessop, G. (1925). Angles of Contact and Polarity of Solid Surfaces. *Journal of the Chemical Society, Transactions*, *127*, 1863–1868.

Al-Raoush, R. I., & Willson, C. S. (2005). Extraction of physically realistic pore network properties from three-dimensional synchrotron X-ray microtomography images of unconsolidated porous media systems. *Journal of Hydrology*, *300*(1–4), 44–64. https://doi.org/10.1016/j.jhydrol.2004.05.005

Anwar, A. H. M. F., Bettahar, M., & Matsubayashi, U. (2000). A method for determining air-water interfacial area in variably saturated porous media. *Journal of Contaminant Hydrology*, *43*(2), 129–146. https://doi.org/10.1016/S0169-7722(99)00103-5

Araujo, J. B., Mainhagu, J., & Brusseau, M. L. (2015). Measuring air–water interfacial area for soils using the mass balance surfactant-tracer method. *Chemosphere*, *134*, 199–202.

Araújo, J. B., & Brusseau, M. L. (2019). Novel fluid-fluid interface domains in geologic media. *Environmental Science: Processes and Impacts*, *21*(1), 145–154. https://doi.org/10.1039/c8em00343b

Bachmann, J., & Van Der Ploeg, R. R. (2002). A review on recent developments in soil water retention theory: Interfacial tension and temperature effects. *Journal of Plant Nutrition and Soil Science*, *165*(4), 468–478.

Basu, S., & Sharma, M. M. (1996). Measurement of critical disjoining pressure for dewetting of solid surfaces. *Journal of Colloid and Interface Science*, *181*(2), 443–455. https://doi.org/10.1006/jcis.1996.0401

Beaglehole, D., & Christenson, H. K. (1992). Vapor adsorption on mica and silicon: Entropy effects, layering, and surface forces. *Journal of Physical Chemistry*, *96*(8), 3395–3403. https://doi.org/10.1021/j100187a040

Beil, W., & Carlsen, I. C. (1991). Surface reconstruction from stereoscopy and "shape from shading" in SEM images. *Machine Vision and Applications*, *4*(4), 271–285. https://doi.org/10.1007/BF01815304

Blunt, M. J. (2001). Flow in porous media - pore-network models and multiphase flow. *Current Opinion in Colloid & Interface Science*, *6*, 197–207. https://doi.org/10.1016/S1359-0294(01)00084-X

Bohr, J., Wogelius, R. A., Morris, P. M., & Stipp, S. L. S. (2010). Thickness and structure of the water film deposited from vapour on calcite surfaces. *Geochimica et Cosmochimica Acta*, *74*(21), 5985–5999. https://doi.org/10.1016/j.gca.2010.08.003

Bradford, S. A., & Leij, F. J. (1997). Estimating interfacial areas for multi-fluid soil systems. *Journal of Contaminant Hydrology*, *27*(1–2), 83–105.

Brown, S. R. (1987). A note on the description of surface roughness using fractal dimension. *Geophysical Research Letters*, *14*(11), 1095–1098.

Brown, S. R. (1989). Transport of Fluid and Electric Current Through a Single Fracture. *Geophysical Research Letters*, *94*(2), 9429–9438.

Brusseau, M. L. (2018). Assessing the potential contributions of additional retention processes to PFAS retardation in the subsurface. *Science of the Total Environment*, *613–614*, 176–185. https://doi.org/10.1016/j.scitotenv.2017.09.065

Brusseau, M. L., Peng, S., Schnaar, G., & Costanza-Robinson, M. S. (2006). Relationships among air-water interfacial area, capillary pressure, and water saturation for a sandy porous medium. *Water Resources Research*, *42*(3).

Brusseau, M. L., Peng, S., Schnaar, G., & Murao, A. (2007). Measuring air− water interfacial areas with x-ray microtomography and interfacial partitioning tracer tests. *Environmental Science & Technology*, *41*(6), 1956–1961.

Brusseau, M. L., Narter, M., & Janousek, H. (2010). Interfacial partitioning tracer test measurements of organic-liquid/water interfacial areas: application to soils and the influence of surface roughness. *Environmental Science & Technology*, *44*(19), 7596–7600.

Brusseau, M. L., El Ouni, A., Araujo, J. B., & Zhong, H. (2015). Novel methods for measuring air–water interfacial area in unsaturated porous media. *Chemosphere*, *127*, 208–213.

Brusseau, M. L., Yan, N., Van Glubt, S., Wang, Y., Chen, W., Lyu, Y., et al. (2019). Comprehensive retention model for PFAS transport in subsurface systems. *Water Research*, *148*, 41–50. https://doi.org/10.1016/j.watres.2018.10.035

Bryant, S. L., & Johnson, A. (2004). Bulk and film contributions to fluid/fluid interfacial area in granular media. *Chemical Engineering Communications*, *191*(12), 1660–1670. https://doi.org/10.1080/00986440490472742

Cary, J. W. (1994). Estimating the surface area of fluid phase interfaces in porous media. *Journal of Contaminant Hydrology*, *15*(4), 243–248.

Cassie, A. B. D., & Baxter, S. (1944). Wettability of porous surfaces. *Transactions of the Faraday Society*, *40*, 546–551.

Chan, T. P., & Govindaraju, R. S. (2011). Pore-morphology-based simulations of drainage and wetting processes in porous media. *Hydrology Research*, *42*(2–3), 128–149.

Chen, L., & Kibbey, T. C. G. (2006). Measurement of air-water interfacial area for multiple

hysteretic drainage curves in an unsaturated fine sand. *Langmuir*, *22*(16), 6874–6880. https://doi.org/10.1029/2004WR003278.(1)

Coles, M. E., Hazlett, R. D., Spanne, P., Soll, W. E., Muegge, E. L., & Jones, K. W. (1998). Pore level imaging of fluid transport using synchrotron X-ray microtomography. *Journal of Petroleum Science and Engineering*, *19*(1–2), 55–63. https://doi.org/10.1016/S0920-4105(97)00035-1

Costanza-Robinson, M. S., & Brusseau, M. L. (2002). Air-water interfacial areas in unsaturated soils: Evaluation of interfacial domains. *Water Resources Research*, *38*(10), 13-1-13–17. https://doi.org/10.1029/2001wr000738

Costanza-Robinson, M. S., Harrold, K. H., & Lieb-Lappen, R. M. (2008). X-ray microtomography determination of air− water interfacial area− water saturation relationships in sandy porous media. *Environmental Science & Technology*, *42*(8), 2949–2956.

Costanza-Robinson, M. S., & Brusseau, M. L. (2002). Air-water interfacial areas in unsaturated soils: Evaluation of interfacial domains. *Water Resources Research*, *38*(10).

Costanza, M. S., & Brusseau, M. L. (2000). Contaminant vapor adsorption at the gas− water interface in soils. *Environmental Science & Technology*, *34*(1), 1–11.

Culligan, K. A., Wildenschild, D., Christensen, B. S. B., Gray, W. G., Rivers, M. L., & Tompson, A. F. B. (2004). Interfacial area measurements for unsaturated flow through a porous medium. *Water Resources Research*, *40*(12).

Dalla, E., Hilpert, M., & Miller, C. T. (2002). Computation of the interfacial area for two-fluid porous medium systems. *Journal of Contaminant Hydrology*, *56*(1–2), 25–48.

Diamantopoulos, E, Durner, W., & Harter, T. (2016). Prediction of capillary air-liquid interfacial area vs. saturation function from relationship between capillary pressure and water saturation. *Advances in Water Resources*, *97*, 219–223.

Diamantopoulos, Efstathios, & Durner, W. (2013). Physically-based model of soil hydraulic properties accounting for variable contact angle and its effect on hysteresis. *Advances in Water Resources*, *59*, 169–180.

Dobson, R., Schroth, M. H., Oostrom, M., & Zeyer, J. (2006). Determination of NAPL-water interfacial areas in well-characterized porous media. *Environmental Science and Technology*, *40*(3), 815–822. https://doi.org/10.1021/es050037p

Dullien, F. A. L., Zarcone, C., Macdonald, I. F., Collins, A., & Bochard, R. D. E. (1989). The effects of surface roughness on the capillary pressure curves and the heights of capillary rise in glass bead packs. *Journal of Colloid and Interface Science*, *127*(2), 362–372.

Fourar, M., Bories, S., Lenormand, R., & Persoff, P. (1993). 2-Phase Flow in Smooth and Rough

Fractures - Measurement and Correlation. *Water Resources Research*, *29*(11), 3699–3708. https://doi.org/10.1029/93WR01529

Gaebel, C., Lead, J. R., Renshaw, J. C., & Tellam, J. H. (2009). Preliminary indications from atomic force microscopy of the presence of rapidly-formed nanoscale films on aquifer material surfaces. *Journal of Contaminant Hydrology*, *108*(1–2), 46–53. https://doi.org/10.1016/j.jconhyd.2009.05.006

Ghanbarian, B., Hunt, A. G., & Daigle, H. (2016). Fluid flow in porous media with rough pore-solid interface. *Water Resources Research*, *52*(3), 2045–2058.

Gibson, C. T., Turner, I. J., Roberts, C. J., & Lead, J. R. (2007). Quantifying the dimensions of nanoscale organic surface layers in natural waters. *Environmental Science and Technology*, *41*(4), 1339–1344. https://doi.org/10.1021/es061726j

Gladkikh, M., & Bryant, S. (2003). Prediction of interfacial areas during imbibition in simple porous media. *Advances in Water Resources*, *26*(6), 609–622.

Grant, G. P., & Gerhard, J. I. (2007). Simulating the dissolution of a complex dense nonaqueous phase liquid source zone: 1. Model to predict interfacial area. *Water Resources Research*, *43*(12).

Gvirtzman, H., & Roberts, P. V. (1991). Pore scale spatial analysis of two immiscible fluids in porous media. *Water Resources Research*, *27*(6), 1165–1176.

Hassanizadeh, S. M., & Gray, W. G. (1993). Thermodynamic basis of capillary pressure in porous media. *Water Resources Research*, *29*(10), 3389–3405.

Hazlett, R. D. (1995). Simulation of capillary-dominated displacements in microtomographic images of reservoir rocks. *Transport in Porous Media*, *20*(1–2), 21–35. https://doi.org/10.1007/BF00616924

Helland, J. O., & Skjaeveland, S. M. (2007). Relationship between capillary pressure, saturation, and interfacial area from a model of mixed-wet triangular tubes. *Water Resources Research*, *43*(12).

Hilpert, M., & Miller, C. T. (2001). Pore-morphology-based simulation of drainage in totally wetting porous media. *Advances in Water Resources*, *24*(3–4), 243–255. https://doi.org/10.1016/S0309-1708(00)00056-7

Hirasaki, G. J. (1991). Wettability: fundamentals and surface forces. *SPE Formation Evaluation*, *6*(2), 217–226. https://doi.org/10.2118/17367-PA

Huh, C., & Mason, S. G. (1977). Effects of surface roughness on wetting (theoretical). *Journal of Colloid And Interface Science*, *60*(1), 11–38. https://doi.org/10.1016/0021-9797(77)90251-X

Joekar-Niasar, V, Hassanizadeh, S. M., & Leijnse, A. (2008). Insights into the relationships

among capillary pressure, saturation, interfacial area and relative permeability using pore-network modeling. *Transport in Porous Media*, *74*(2), 201–219.

Joekar-Niasar, Vahid, & Hassanizadeh, S. M. (2012). Uniqueness of Specific Interfacial Area-Capillary Pressure-Saturation Relationship Under Non-Equilibrium Conditions in Two-Phase Porous Media Flow. *Transport in Porous Media*, *94*(2), 465–486. https://doi.org/10.1007/s11242-012-9958-3

Joekar-Niasar, V., Prodanović, M., Wildenschild, D., & Hassanizadeh, S. M. (2010). Network model investigation of interfacial area, capillary pressure and saturation relationships in granular porous media. *Water Resources Research*, *46*(6).

Johnsen, A. R., Wick, L. Y., & Harms, H. (2005). Principles of microbial PAH-degradation in soil. *Environmental Pollution*, *133*(1), 71–84.

Karkare, M. V., & Fort, T. (1996). Determination of the air-water interfacial area in wet "Unsaturated" porous media. *Langmuir*, *12*(8), 2041–2044.

Kibbey, T. C. G. (2013). The configuration of water on rough natural surfaces: Implications for understanding air-water interfacial area, film thickness, and imaging resolution. *Water Resources Research*, *49*(8), 4765–4774.

Kibbey, T. C. G., & Chen, L. (2012). A pore network model study of the fluid-fluid interfacial areas measured by dynamic-interface tracer depletion and miscible displacement water phase advective tracer methods. *Water Resources Research*, *48*(10).

Kim, H., Rao, P. S. C., & Annable, M. D. (1997a). Determination of effective air-water interfacial area in partially saturated porous media using surfactant adsorption. *Water Resources*, *33*(12), 2705–2711.

Kim, H., Rao, P. S. C., & Annable, M. D. (1997b). Determination of effective air-water interfacial area in partially saturated porous media using surfactant adsorption. *Water Resources Research*, *33*(12), 2705–2711.

Kim, H., Rao, P. S. C., & Annable, M. D. (1999a). Gaseous tracer technique for estimating air–water interfacial areas and interface mobility. *Soil Science Society of America Journal*, *63*(6), 1554–1560.

Kim, H., Rao, P. S. C., & Annable, M. D. (1999b). Gaseous Tracer Technique for Estimating Air–Water Interfacial Areas and Interface Mobility. *Soil Science Society of America Journal*, 1554–1560.

Kim, T. W., Tokunaga, T. K., Shuman, D. B., Sutton, S. R., Newville, M., & Lanzirotti, A. (2012). Thickness measurements of nanoscale brine films on silica surfaces under geologic CO2 sequestration conditions using synchrotron X-ray fluorescence. *Water Resources Research*,

48(9), 1–13. https://doi.org/10.1029/2012WR012200

Leverett, M. (1941). Capillary behavior in porous solids. *Transactions of the AIME*, *142*(01), 152–169.

Likos, W. J., & Jaafar, R. (2013). Pore-scale model for water retention and fluid partitioning of partially saturated granular soil. *Journal of Geotechnical and Geoenvironmental Engineering*, *139*(5), 724–737.

Liu, G., Zhang, M., Ridgway, C., & Gane, P. (2014). Pore wall rugosity: The role of extended wetting contact line length during spontaneous liquid imbibition in porous media. *Colloids and Surfaces A: Physicochemical and Engineering Aspects*, *443*, 286–295. https://doi.org/10.1016/j.colsurfa.2013.11.033

Lyu, Y., Brusseau, M. L., El Ouni, A., Araujo, J. B., & Su, X. (2017). The Gas-Absorption/Chemical-Reaction Method for Measuring Air-Water Interfacial Area in Natural Porous Media. *Water Resources Research*, *53*(11), 9519–9527. https://doi.org/10.1002/2017WR021717

Lyu, Y., Brusseau, M. L., Chen, W., Yan, N., Fu, X., & Lin, X. (2018). Adsorption of PFOA at the Air-Water Interface during Transport in Unsaturated Porous Media. *Environmental Science and Technology*, *52*(14), 7745–7753. https://doi.org/10.1021/acs.est.8b02348

Majumdar, A., & Bhushan, B. (1990). Role of fractal geometry in roughness characterization and contact mechanics of surfaces. *Journal of Tribology*, *112*(2), 205–216. https://doi.org/10.1115/1.2920243

McClure, J. E., Berrill, M. A., Gray, W. G., & Miller, C. T. (2016). Influence of phase connectivity on the relationship among capillary pressure, fluid saturation, and interfacial area in two-fluid-phase porous medium systems. *Physical Review E*, *94*(3), 33102.

Morrow, N. R. (1970a). Irreducible wetting-phase saturations in porous media. *Chemical Engineering Science*, *25*(11), 1799–1815. https://doi.org/10.1016/0009-2509(70)80070-7

Morrow, N. R. (1970b). Physics dnd Thermodyndmics of Cdpilldry Action in Porous Medid. *Industrial & Engineering Chemistry*, *62*(6), 32–56.

Oliver, J. P., Huh, C., & Mason, S. G. (1980). An experimental study of some effects of solid surface roughness on wetting. *Colloids and Surfaces*, *1*(1), 79–104.

Oostrom, M., White, M. D., & Brusseau, M. L. (2001). Theoretical estimation of free and entrapped nonwetting–wetting fluid interfacial areas in porous media. *Advances in Water Resources*, *24*(8), 887–898.

Or, D. (2002). Physical Processes Affecting Microbial Habitats and Activity in Unsaturated

Porous Media. *Journal of Agricultural and Marine Sciences [JAMS]*, *7*(2), 39. https://doi.org/10.24200/jams.vol7iss2pp39-45

Or, D., Smets, B. F., Wraith, J. M., Dechesne, A., & Friedman, S. P. (2007). Physical constraints affecting bacterial habitats and activity in unsaturated porous media - a review. *Advances in Water Resources*, *30*(6–7), 1505–1527. https://doi.org/10.1016/j.advwatres.2006.05.025

Or, Dani, & Tuller, M. (1999). Liquid retention and interfacial area in variably saturated porous media: Upscaling from single-pore to sample-scale model. *Water Resources Research*, *35*(12), 3591–3605.

Or, Dani, & Tuller, M. (2000). Flow in unsaturated fractured porous media: Hydraulic conductivity of rough surfaces. *Water Resources Research*, *36*(5), 1165–1177.

Peng, S., & Brusseau, M. L. (2005). Impact of soil texture on air-water interfacial areas in unsaturated sandy porous media. *Water Resources Research*, *41*(3).

Philip, J. R. (1977). Unitary approach to capillary condensation and adsorption. *The Journal of Chemical Physics*, *66*(11), 5069–5075. https://doi.org/10.1063/1.433814

Philip, J. R. (1978). Adsorption and capillary condensation on rough surfaces. *Journal of Physical Chemistry*, *82*(12), 1379–1385. https://doi.org/10.1021/j100501a012

Porter, M. L., Schaap, M. G., & Wildenschild, D. (2009). Lattice-Boltzmann simulations of the capillary pressure–saturation–interfacial area relationship for porous media. *Advances in Water Resources*, *32*(11), 1632–1640.

Porter, M. L., Wildenschild, D., Grant, G., & Gerhard, J. I. (2010). Measurement and prediction of the relationship between capillary pressure, saturation, and interfacial area in a NAPL-water-glass bead system. *Water Resources Research*, *46*(8), 1–10. https://doi.org/10.1029/2009WR007786

Pyrak-Nolte, L. J., Nolte, D. D., Chen, D., & Giordano, N. J. (2008). Relating capillary pressure to interfacial areas. *Water Resources Research*, *44*(6).

Rangel-German, E., Akin, S., & Castanier, L. (2006). Multiphase-flow properties of fractured porous media. *Journal of Petroleum Science and Engineering*, *51*(3–4), 197–213. https://doi.org/10.1016/j.petrol.2005.12.010

Reeves, P. C., & Celia, M. A. (1996). A functional relationship between capillary pressure, saturation,and interfacial area as revealed by a pore-scale network model. *Water Resources Research*, *32*(8), 2345–2358.

Saripalli, K. P., Kim, H., Rao, P. S. C., & Annable, M. D. (1997). Measurement of specific fluid-fluid interfacial areas of immiscible fluids in poreus media. *Environmental Science and*

Technology, *31*(3), 932–936. https://doi.org/10.1021/es960652g

Schaefer, C. E., DiCarlo, D. A., & Blunt, M. J. (2000). Determination of water-oil interfacial area during 3-phase gravity drainage in porous media. *Journal of Colloid and Interface Science*, *221*(2), 308–312. https://doi.org/10.1006/jcis.1999.6604

Schnaar, G., & Brusseau, M. L. (2005). Pore-scale characterization of organic immiscible-liquid morphology in natural porous media using synchrotron x-ray microtomography. *Environmental Science and Technology*, *39*(21), 8403–8410. https://doi.org/10.1021/es0508370

Schnaar, G., & Brusseau, M. L. (2006). Characterizing Pore-Scale Configuration of Organic Immiscible Liquid in Multiphase Systems With Synchrotron X-Ray Microtomography. *Vadose Zone Journal*, *5*(2), 641. https://doi.org/10.2136/vzj2005.0063

Schroth, M. H., Oostrom, M., Dobson, R., & Zeyer, J. (2008). Thermodynamic Model for Fluid–Fluid Interfacial Areas in Porous Media for Arbitrary Drainage–Imbibition Sequences. *Vadose Zone Journal*, *7*(3), 966. https://doi.org/10.2136/vzj2007.0185

Schwartz, L. M., Sen, P. N., & Johnson, D. L. (1989). Influence of rough surfaces on electrolytic conduction in porous media. *Physical Review B*, *40*(4), 2450–2458. https://doi.org/10.1103/PhysRevB.40.2450

Shuttleworth, R., & Bailey, G. L. J. (1948). The spreading of a liquid on a rough solid surface. *Discussions of the Faraday Society 3*, 16–22. https://doi.org/10.1017/S0022112083001214

Silverstein, D. L., & Fort, T. (1997). Studies in air-water interfacial area for wet unsaturated particulate porous media systems. *Langmuir*, *13*(17), 4758–4761.

Skopp, J. (1985). Oxygen Uptake and Transport in Soils: Analysis of the Air-water Interfacial Area 1. *Soil Science Society of America Journal*, *49*(6), 1327–1331.

Sutton, S. R., Bertsch, P. M., Newville, M., Rivers, M., Lanzirotti, A., & Eng, P. (2002). Microfluorescence and Microtomography Analyses of Heterogeneous Earth and Environmental Materials. *Reviews in Mineralogy and Geochemistry*, *49*(1), 429–483. https://doi.org/10.2138/rmg.2002.49.8

Taylor, J. B., Carrano, A. L., & Kandlikar, S. G. (2006). Characterization of the effect of surface roughness and texture on fluid flow—past, present, and future☆. *International Journal of Thermal Sciences*, *45*(10), 962–968.

Thompson, M. E., & Brown, S. R. (1991). The effect of anisotropic surface roughness on flow and transport in fractures. *Journal of Geophysical Research: Solid Earth*, *96*(B13), 21923–21932.

Tokunaga, T. K. (2011). Physicochemical controls on adsorbed water film thickness in unsaturated geological media. *Water Resources Research*, *47*(8).

Tokunaga, T. K., & Wan, J. (1997). Water film flow along fracture surfaces of porous rock. *Water Resources Research*, *33*(6), 1287–1295. https://doi.org/10.1029/97WR00473

Tokunaga, T. K., Wan, J., & Sutton, S. R. (2000). Transient film flow on rough fracture surfaces. *Water Resources Research*, *36*(7), 1737–1746.

Tokunaga, T. K., Olson, K. R., & Wan, J. (2003). Moisture characteristics of Hanford gravels. *Vadose Zone Journal*, *2*(3), 322–329.

Torkzaban, S., & Bradford, S. A. (2016). Critical role of surface roughness on colloid retention and release in porous media. *Water Research*, *88*, 274–284. https://doi.org/10.1016/j.watres.2015.10.022

Tuller, M., & Or, D. (2001). Hydraulic conductivity of variably saturated porous media: Film and corner flow in angular pore space. *Water Resources Research*, *37*(5), 1257–1276. https://doi.org/10.1029/2000WR900328

Tuller, Markus, & Or, D. (2004). Retention of water in soil and the soil water characteristic curve. *Encyclopedia of Soils in the Environment*, *4*, 278–289.

Tuller, Markus, & Or, D. (2005). Water films and scaling of soil characteristic curves at low water contents. *Water Resources Research*, *41*(9), 1–6. https://doi.org/10.1029/2005WR004142

Tuller, Markus, Or, D., & Dudley, L. M. (1999). Adsorption and capillary condensation in porous media: Liquid retention and interfacial configurations in angular pores. *Water Resources Research*, *35*(7), 1949–1964.

Vogel, H. J., & Roth, K. (2001). Quantitative morphology and network representation of soil pore structure. *Advances in Water Resources*, *24*(3–4), 233–242. https://doi.org/10.1016/S0309-1708(00)00055-5

Wan, J., Wilson, J. L., & Kieft, T. L. (1994). Influence of the gas-water interface on transport of microorganisms through unsaturated porous media. *Applied and Environmental Microbiology*, *60*(2), 509–516.

Wenzel, R. N. (1936). Resistance of solid surfaces to wetting by water. *Industrial & Engineering Chemistry*, *28*(8), 988–994.

Wildenschild, D., Hopmans, J. W., Vaz, C. M. P., Rivers, M. L., Rikard, D., & Christensen, B. S. B. (2002). Using X-ray computed tomography in hydrology: systems, resolutions, and limitations. (Special Issue: Non-invasive methods in hydrology). *Journal of Hydrology*, *267*, 285–297.

Yan, S., Adegbule, A., & Kibbey, T. C. G. (2017). A hybrid 3D SEM reconstruction method optimized for complex geologic material surfaces. *Micron*, *99*(February), 26–31.

https://doi.org/10.1016/j.micron.2017.03.018

Zheng, W., Yu, X., & Jin, Y. (2015). Considering surface roughness effects in a triangular pore space model for unsaturated hydraulic conductivity. *Vadose Zone Journal*, *14*(7), 1–13. https://doi.org/10.2136/vzj2014.09.0121

APPENDICES

Appendix A

Pore-Scale Modeling of Fluid-Fluid Interfacial Area in Variably Saturated Porous Media Containing Micro-Scale Surface Roughness

Hao Jiang[1], Bo Guo[2] and Mark L. Brusseau[2,3,*]

[1]Department of Chemical and Environmental Engineering
University of Arizona
1133 E James E Rogers Way
Tucson, Arizona 85721, USA

[2]Department of Hydrology and Atmospheric Sciences
University of Arizona
1133 E James E Rogers Way
Tucson, Arizona 85721, USA

[3]Department of Environmental Science
School of Earth and Environmental Sciences
University of Arizona
429 Shantz Bldg.
Tucson, AZ 85721, USA

Published in:
Water Resources Research

Citation:
Jiang, H., Guo, B., & Brusseau, M. L. (2020). Pore-scale modeling of fluid-fluid interfacial area in variably saturated porous media containing microscale surface roughness. Water Resources Research, 56, e2019WR025876. https://doi.org/10.1029/2019WR025876

*Corresponding author

Abstract

A pore-scale model is developed to simulate fluid-fluid interfacial area in variably saturated porous media, with a specific focus on incorporating the effects of solid-surface roughness. The model is designed to quantify total (film and meniscus) fluid-fluid interfacial area (A_{nw}) over the full range of wetting-phase fluid saturation (S_w) based on the inherent properties of the porous medium. The model employs a triangular pore space bundle of cylindrical capillaries (BCC) framework, modified with three surface roughness-related parameters. The first parameter (surface roughness factor) represents the overall magnitude of surface roughness, whereas the other two parameters (interface growth factor and critical adsorptive film thickness) reflect the micro-scale structure of surface roughness. A series of sensitivity analyses was conducted for the controlling variables, and the efficacy of the model was tested using air-water interfacial area data measured for three natural porous media. The model produced good simulations of the measured A_{nw} data over the full range of saturation. The results demonstrate that total interfacial areas for natural media are typically much larger than those for ideal media comprising smooth surfaces due to the substantial contribution of surface roughness to wetting-film interfacial area. The degree to which fluid-fluid interfacial area is influenced by roughness is a function of fluid-retention characteristics and the nature of the rough surfaces. The full impact of roughness may be masked to some degree due to the formation of thick wetting films, which is explicitly quantified by the model. Application of the model provides insight into the importance of the interplay between pore-scale distribution and configuration of wetting fluid and the surface properties of solids.

Key points

- A triangular pore space BCC model is developed to simulate the impact of solid surface roughness on fluid-fluid interfacial area.
- Model efficacy is tested with air-water interfacial area data measured for three natural porous media.
- The model presents a means by which to quantify fluid-fluid interfacial area for natural porous media in multiphase fluid systems.

Key Words: Interfacial area; surface roughness; bundle-of-cylindrical-capillaries (BCC); pore geometry

1. Introduction

The interface between immiscible fluids in porous media is a fundamental property for mass and energy transfer, contaminant retention, and biogeochemical reactions, which play a significant role in many disciplines including hydrology, environmental science, petroleum engineering, and soil mechanics (e.g., Leverett, 1941; Skopp, 1985; Gvirtzman & Roberts, 1991; Hassanizadeh & Gray, 1993; Costanza & Brusseau, 2000; Pyrak-Nolte et al., 2008). Fluid-fluid interfaces in porous media are typically considered to comprise two types: one consisting of films of wetting fluid associated with the solid surfaces (film-associated interface) and the other consisting of capillary-supported menisci residing in inter-granular pore space (capillary or meniscus interface). The film-associated interfaces typically comprise a large fraction of total interfacial area at most wetting-phase saturations for natural porous media, often exceeding the capillary meniscus contributions by several orders of magnitude (Or & Tuller, 1999, Brusseau et al., 2006, 2007).

Surface roughness of natural grains is one of the most important properties affecting fluid-solid interactions in porous media. It encompasses different sources and types of features that span a wide range of spatial scales from nanometer to micrometer. The impacts of surface roughness on the displacement and distribution of fluids in porous media have been investigated for decades. For example, researchers have shown that surface roughness can affect fluid behavior by changing the degree of wettability (Wenzel, 1936; Cassie & Baxter, 1944; Oliver et al., 1980; AlRatrout et al., 2018). In addition, researchers have studied whether surface roughness has direct impacts on drainage and imbibition as measured with the soil water characteristic (SWC) curve (Dullien et al., 1989; Tokunaga et al., 2003). The relationship between grain surface roughness and hydraulic conductivity of porous media has also been investigated (Brown, 1987; Thompson & Brown, 1991; Tokunaga & Wan, 1997; Lampurlanés & Cantero-Martínez, 2006).

The influence of surface roughness on fluid-fluid interfaces in natural porous media has been discussed in prior experimental studies. For example, exponential increases in air-water interfacial area were measured at low water saturations with the gas-phase interfacial partitioning tracer test (IPTT) method (Kim et al., 1999; Costanza-Robinson & Brusseau, 2002; Peng & Brusseau, 2005). These measured interfacial areas are orders-of-magnitude greater than geometric-based solid surface areas calculated with the smooth-surface assumption. Conversely, they are consistent with specific solid surface areas measured

using the N_2-BET method, which incorporates surface roughness. Interfacial areas measured with aqueous-phase IPTT methods have also been shown to be larger than geometric smooth-surface solid surface areas (Saripalli et al., 1997; Schaefer et al., 2000; Brusseau et al., 2007, 2008, 2015; Zhong et al., 2016). In addition, the total interfacial areas measured with both gas-phase and aqueous-phase IPTT methods are much larger than interfacial areas measured with X-ray computed microtomography (CMT), which has a resolution limit at the micrometer level (Brusseau et al., 2006, 2007, 2008, 2010; McDonald et al., 2016). These observations were attributed to the impact of surface roughness and its contribution to film-associated interfacial area. In contrast, interfacial areas measured with CMT and IPTT methods were identical to each other and to the geometric smooth-surface solid surface area and the N_2-BET solid surface area for a glass-bead medium that has no measurable surface roughness (Narter & Brusseau, 2010; Zhong et al., 2016; Lyu et al., 2017).

Prior studies have developed several quantitative approaches for representing the influence of surface roughness on fluid-solid interactions. For example, the specific solid surface area (*SA*) has been used as a variable to implicitly incorporate surface roughness, and relationships between the maximum fluid-fluid interfacial area and *SA* have been developed (e.g., Or & Tuller, 1999; Peng & Brusseau, 2005; Brusseau et al., 2010). However, these efforts did not employ specific information about the surface-roughness structures. Conversely, other investigators have proposed quantitative descriptions of the structure of surface roughness. For example, Philip (1978) used such a description to examine the influence of roughness on film thickness for adsorbed and capillary condensed wetting fluid. Or and Tuller (2000) proposed a quantitative description of surface roughness, using a statistical distribution for the depth of pits to predict the hydraulic conductivity for film flow. They then generalized the model to the sample scale using a BCC network model in follow-up work (Tuller & Or, 2001). More recently, Zheng et al. (2015) simplified the quantification of roughness in a BCC-based model for producing SWC curves and predicting hydraulic conductivity. In their approach, the surface roughness was represented as the ratio between rough and smooth surface areas. These latter studies did not examine the relationship between surface roughness and fluid-fluid interfaces specifically. Hence, quantitative approaches still need to be developed to explicitly delineate the impact of surface roughness on fluid-fluid interfaces.

Over the past decades, a number of approaches have been used for the simulation of fluid-fluid interfaces in porous media, including (a) idealized pore-geometry models (e.g., Cary, 1994; Or & Tuller, 1999; Oostrom et al., 2001; Diamantopoulos & Durner, 2013; Likos & Jaafar, 2013); (b) thermodynamic-based models (e.g., Leverett, 1941; Bradford & Leij, 1997; Grant & Gerhard, 2007; Schroth et al., 2008); (c) pore-scale network models (e.g., Reeves & Celia, 1996; Kawanishi et al., 1998; Joekar-Niasar et al., 2010; Kibbey & Chen, 2012); (d) pore-morphology models (e.g., Dalla et al., 2002; Chan & Govindaraju, 2011); and (e) direct pore-scale numerical simulations using the Lattice Boltzmann Method (e.g., Porter et al., 2009, 2010; McClure et al., 2016). Models developed with the first two approaches can be expressed as analytical equations, while the other approaches require numerical treatments. Most prior studies have either focused only on meniscus-associated interfacial area—ignoring films—or included thin films but without considering the impact of solid surface roughness. In addition, performance testing of the models by comparison to measured interfacial-area data has to date been restricted to simple porous media such as glass beads or sands that have minimal to relatively small magnitudes of surface roughness, and to limited ranges of water saturations (>20%).

In the present study, a pore-geometry approach based on the triangular-pore BCC framework is used to develop a model to simulate total (film and meniscus) fluid-fluid interfacial area. The methodology incorporates and modifies the approach used by Zheng et al. (2015) to represent surface roughness, and extends it to specific quantification of fluid-fluid interfacial area. The influence of the controlling variables is illustrated via example simulations and a sensitivity analysis for model parameters. The efficacy of the model is evaluated by application to air-water interfacial area data measured for three natural media. The simulation results are used to illustrate the influence of surface roughness on the magnitude of fluid-fluid interfacial area.

2. Model Development

2.1 Incorporating Surface Roughness

Traditional concepts of surface roughness are usually related to a surface elevation profile where each point on the surface has a vertical height relative to a reference plane.

The arithmetic average (R_a) or root mean square (R_{rms}) of the relative heights at all points is often used to represent the surface roughness. However, researchers have raised concerns that this approach does not adequately represent the fractal geometry of rough surfaces (e.g., Ghanbarian et al., 2016), in which the actual surface structures may have a fractal growth that greatly exceeds the scale of traditional roughness. An alternative approach to define the effective roughness of a surface has been suggested as a "surface roughness factor", which defines the magnitude of "actual or effective" surface area versus the geometric-base smooth surface area in one unit surface (e.g., Wenzel, 1936; Kamusewitz & Possart, 2003; Santamaría et al., 2012; Zheng et al., 2015). By definition, the geometric-base surface area is a low-resolution characteristic and is typically treated as smooth, whereas the actual surface area incorporates the effects of surface roughness across a range of higher-resolution scales. The term "rugosity" has also sometimes been used to emphasize its difference from traditional roughness (e.g., Beyhan et al., 2007; Liu et al., 2014).

A general approach to incorporate surface roughness for any given solid surface is used for this study, based on and revised from the methods employed by Zheng et al. (2015). By definition, the geometric base of a surface has a surface area defined as L_0 in its one-dimensional cross-section, which is termed the geometric smooth surface area (Figure 1a~1c). A rough surface is considered to have a surface area specified as L_r, representing the topological surface area. The surface roughness factor, X, is then defined as the actual surface area (L_r) divided by the corresponding geometric smooth surface area (L_0) for any unit of surface:

$$X = L_r / L_0 \qquad (1a)$$

This factor can be considered as an index characterizing the degree to which the surface of a solid deviates from a functionally smooth surface. When wetting film is present on the same geometric base (Figure 1a~1c), its upper interfacial area (L_f), i.e., the fluid-fluid interfacial area, can be specified and compared to the same geometric base L_0. This produces an interfacial area factor, X_a, defined as:

$$X_a = L_f / L_0 \qquad (1b)$$

where $1 \leq X_a \leq X$ at any saturation (Zheng et al., 2015). It is assumed that the system is homogeneous such that X is the same for all surfaces.

For rough surfaces, the involvement of capillary forces can in some cases retain

additional wetting fluid beyond that of adsorption, producing thicker films (e.g., Philip, 1978; Israelachvili, 2011; Tokunaga, 2011). It is therefore assumed that under certain conditions the thicknesses of the wetting films will be sufficient to mask the full impact of roughness on interfacial area. The impact of roughness may be fully masked for some systems, particularly at higher wetting-phase saturations, which would result in smooth fluid-fluid interfaces (referred to as thick film as shown in Figure 1a). In this case, there is no roughness effect on interfacial area and $L_f = L_0$. At very low wetting-phase saturations where the matric potential is high, it is assumed that adsorptive forces dominate over capillary forces such that the film is only a few molecules thick (referred to as thin film as shown in Figure 1c) (e.g., Or and Tuller, 1999; Resureccion et al., 2011; Tokunaga, 2011). Under this condition, the interfacial area is equivalent to the actual solid surface area, i.e., $L_f = L_r = XL_0$. Under intermediate-saturation conditions, the combination of surface adsorption and capillary retention results in films of intermediate thickness and folded and uneven interfaces (Figure 1b), whose cumulative length is between [L_0, XL_0]. Hence, depending on the magnitude of matric potential, the local configuration of the wetting fluid, and the balance between adsorption and capillary forces, there are three types of wetting films in a typical nonwetting-wetting system (e.g., air-water, oil-water) in porous media: thick film, intermediate film, and thin film (Figure 1a~1c).

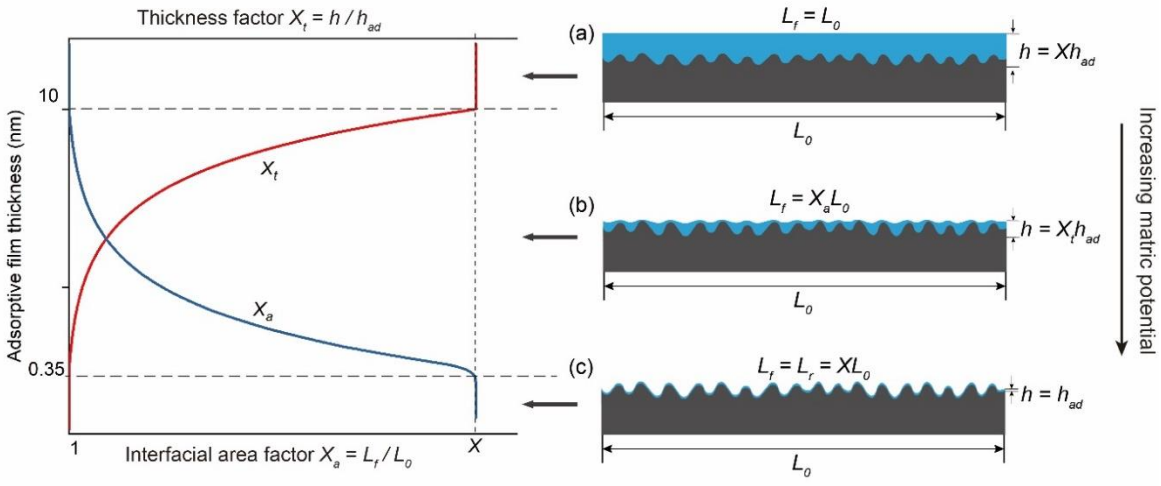

Figure 10. The functional relationship between the surface roughness factor X, film thickness factor X_t, interfacial area factor X_a, equivalent film thickness h, and the adsorptive film thickness h_{ad} (in a log-scale axis). The wetting film configurations under different

matric potentials are divided into three regimes: (a) thick film (b) intermediate film (c) thin film. Modified from the scheme in Zheng et al. (2015).

Based on the three types of wetting films, a liquid film is assumed to have a normalized equivalent thickness in order to calculate its volume. The equivalent thickness, h, is a function of the matric potential, and represented with a thickness factor X_t, defined as in Zheng et al. (2015):

$$h(\mu) = X_t h_{ad}(\mu) = X_t \sqrt[3]{\frac{A_{svl}}{6\pi\rho\mu}} \quad (2)$$

where $h_{ad}(\mu)$ is the thickness of the adsorptive film (m) given by the empirical equation above (Iwamatsu & Horii, 1996; Or & Tuller, 1999), μ is the matric potential (J/kg), ρ is the liquid density (998.21 kg/m^3 for water), and A_{svl} is the Hamaker constant (J). For air-water-soil systems, the Hamaker constant is usually set at 6×10^{-20} J (Or & Tuller, 1999; Tokunaga, 2011). As discussed by Tuller et al. (1999), this formulation is considered to incorporate the molecular component of disjoining pressure. The terms matric potential μ (J/kg), capillary pressure P_c (Pa), and water pressure head H (cm H_2O) in this study are equivalent. Their unit conversions follow: $\mu=gH$ (g = 9.81 m/s^2) and $P_c = \rho gH = \rho\mu$ (ρ = 998.21 kg/m^3 for water). We adopt the same assumption used by Zheng et al. (2015) that the upper limit of the film thickness factor is set equal to the surface roughness factor, i.e., $X_t = X$ at high wetting saturations (thick film). Their simulations and our following work both show that this simplified definition is acceptable for model applications.

The functional relationship between the surface roughness factor X, film thickness factor X_t, interfacial area factor X_a, and the adsorptive film thickness h_{ad} is presented in Figure 1. It is observed that with increasing matric potential, the film thickness factor X_t decreases from X to 1, while X_a increases from 1 to X. At very low wetting saturations (thin film), it is assumed that the wetting phase is retained only by adsorption to the solid surface, i.e., $h = h_{ad}$. In this case, $X_t = 1$ and $X_a = X$. For the special case of smooth solid surfaces, $X = X_t = X_a = 1$. At high wetting saturations, $X_t = X$ and $X_a = 1$. For the intermediate film on a rough surface, we use Zheng et al. (2015)'s exponential equation for the thickness factor:

$$X_t = \begin{cases} X & h_{ad} \geqslant 10\,\text{nm} \\ X\left(\dfrac{h_{ad}(\mu)}{10}\right)^{\ln X/(\ln 200 - \ln 7)} & 0.35\,\text{nm} < h_{ad} < 10\,\text{nm} \\ 1 & h_{ad} \leqslant 0.35\,\text{nm} \end{cases} \qquad (3)$$

The adsorptive film thickness $h_{ad}(\mu)$ is a function of only matric potential. The two empirical limits of 10 nm (wet end) and 0.35 nm (dry end) given in Zheng et al. (2015) correspond to matric potentials μ_1 = -3.19 J/kg (-32.5 cm H_2O) and μ_2 = -7.44×10^4 J/kg (-758400 cm H_2O).

The two factors X_a and X_t were considered dependent ($X = X_a X_t$) in Zheng et al. (2015). In contrast, we propose a different approach to quantify X_a, based on the observed relationship between interfacial area and matric potential (Kim et al., 1997; Brusseau et al., 2006; Porter et al., 2009; Peng & Brusseau, 2012). The equation is a generalized logistic curve (Figure 2):

$$X_a = \frac{X + e^{k(h_{ad} - h_m)}}{1 + e^{k(h_{ad} - h_m)}} \qquad (4)$$

The parameters h_m and k are related to the microscale structure of the roughness and its impact on interfacial area. h_m is the critical adsorptive film thickness that corresponds to an interfacial area factor (X+1)/2, which is close to half of the total surface area roughness factor. h_m can vary between 0.35 nm and 10 nm in the intermediate film regime. k is a "growth rate" factor representing the exponential increase of interfacial area during drainage ($k > 0$). In equations (3) and (4), we use the adsorptive film thickness $h_{ad}(\mu)$ as the argument, instead of matric potential μ, because the values of μ are inconvenient to adjust given $\mu \propto 1/h_{ad}^3$. Upon these definitions, X_a and X_t are independent functions of matric potential for a given porous medium, and both range within [1, X].

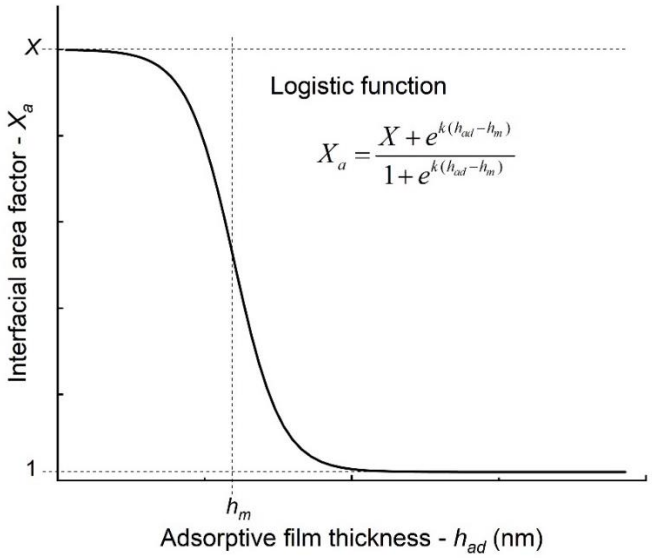

Figure 11. Schematic of the logistic curve for the interfacial area factor (X_a) as a function of adsorptive film thickness (h_{ad}).

2.2 Pore Scale Model

The bundle-of-cylindrical-capillaries (BCC) method has been used to model soil hydraulic properties for many decades. The BCC approach provides a simple yet effective idealization of pore structure to support the development of conceptual and mathematical models (e.g., Dullien, 1992). Modifications to the standard BCC model have been made to improve the accuracy of simulations, such as employing triangular rather than cylindrical pores (e.g., Tuller et al., 1999; Helland & Skjœveland, 2006). BCC-based models have been successful in simulating a variety of phenomenon for many different applications, such as simulating dynamic effects in the capillary-pressure/saturation relationship (Dahle et al., 2005), the flow of water in frozen soil (Watanabe and Flury, 2008), and the influence of biofilms on hydraulic properties of soil (Brangari et al., 2017).

We apply the triangular-pore BCC method with the roughness modifications presented in section 2.1 to determine total fluid-fluid interfacial area in one pore. The cross-section of each pore is treated as an equilateral triangle with a side length of L (Figure 3), and the whole porous medium is approximated as a bundle of triangular tubes, similar to previous studies such as Helland & Skjaeveland (2007) and Diamantopoulos & Durner (2013).

In the present study, we simulate only fluid behavior in the main drainage process.

Drainage in a triangular pore is assumed to follow a centrally-symmetric advance/retreat mechanism (Celia et al., 1995; Blunt, 2001; Helland & Skjaeveland, 2007; Diamantopoulos & Durner, 2013). In a non-wetting/wetting system (typically air/water or oil/water), the non-wetting fluid in a pore is idealized as a symmetric blob located in the center of the pore and the wetting fluid is displaced to the sides and corners. During drainage, the invading non-wetting fluid rapidly displaces the wetting fluid from the center of a filled pore, forming a blob whose dimensions correspond to the pore dimensions (i.e., the onset of drainage). For a partially-drained pore, the central blob grows as matric potential increases, pushing the wetting films towards each corner. At steady state, the wetting fluid is present as films on each side and as capillary menisci at each corner. Under complete drainage, corner wetting fluids are fully displaced and only wetting film remains

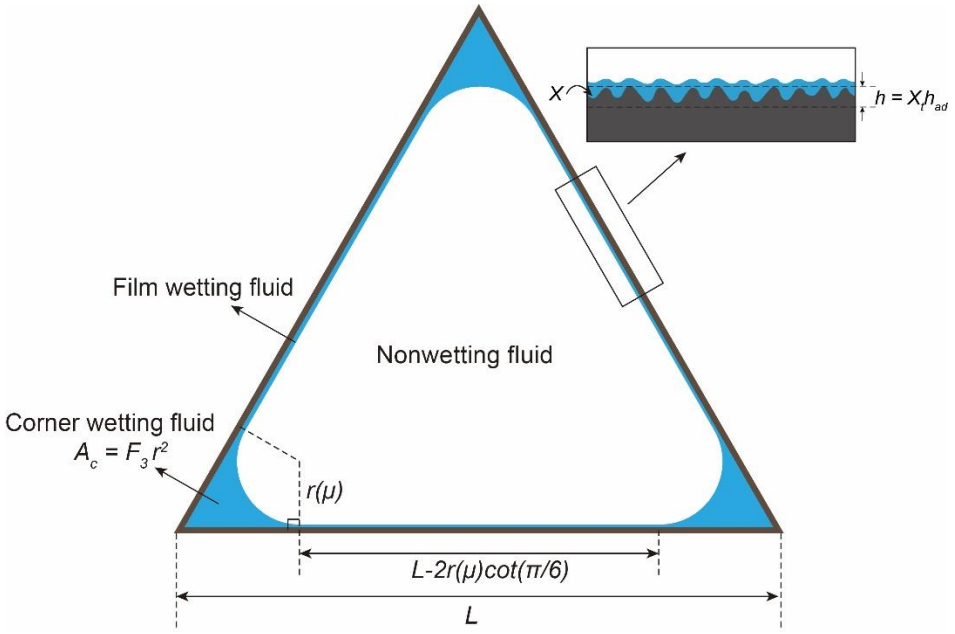

Figure 12. Cross-sectional scheme of a partially-drained equilateral triangular pore and the distribution of corner and film water.

The geometrical relationships within a partially-drained triangular pore are depicted in Figure 3. Diamantopoulos et al. (2016) showed that in a glass-bead medium the transition points between films and menisci might have a contact angle (θ) greater than zero, which reduces the actual meniscus radius. Nevertheless, they also showed that the wettability of natural grain surfaces is sufficiently high such that assuming zero contact angle is

acceptable for many cases. Thus, the present approach is based on a completely wet surface with $\theta = 0$ for all pores. Under this assumption, the meniscus wetting fluid at each corner has a curvature radius of $r(\mu)$ corresponding to the matric potential, which follows the Young-Laplace equation:

$$r(\mu) = -\frac{\gamma}{\rho\mu} \qquad (5)$$

where μ is the matric potential in unit J/kg and γ is the surface tension of the liquid (for air-water $\gamma = 0.0728$ N/m). The area surrounded by the meniscus and two sides of an angle—the corner water saturation of one angle—can be calculated for any regular n-polygons as $A_c = F_n r^2$ (Or & Tuller, 1999). For equilateral triangles, $F_n = 3\sqrt{3} - \pi$. The length of one meniscus curve, which is $\pi r/2$, is the meniscus-associated interfacial area for one corner. It is noted that a non-zero contact angle can be incorporated by including the specified value in equation (5).

The entire inner solid surface of a pore is assumed to have the same surface roughness everywhere with a constant surface roughness factor X and two logistic parameters k and h_m, all of which are considered to be inherent properties of a specific porous medium. For each given matric potential and associated h_{ad}, there is a unique set of X_t and X_a derived from equations (3) and (4), respectively. The length of wetting film on one side is determined by the meniscus radius $r(\mu)$ (shown in Figure 3). Thus, the saturation and interfacial area of wetting film can be determined for one side. The saturation and specific interfacial area of wetting fluid in a single pore is determined as the combination of the wetting fluid in the three sides and three corners (Figure 3).

The saturation of wetting phase (S_{wc} and S_{wf}) and the interfacial area between non-wetting and wetting fluids (A_{nwc} and A_{nwf}) in one pore can be derived using the following equations:

$$S_{wc} = \frac{3F_3 r^2(\mu)}{A_3 L^2} \qquad (6)$$

$$S_{wf} = \frac{3h(\mu)\left[L - 2r(\mu)\cot(\pi/6)\right]}{A_3 L^2} \qquad (7)$$

$$A_{nwc} = \frac{3\pi r(\mu)}{2A_3 L^2} \qquad (8)$$

$$A_{nwf} = \frac{3X_a[L - 2r(\mu)\cot(\pi/6)]}{A_3 L^2} \quad (9)$$

where the subscripts "c" and "f" mean corner wetting fluid and film wetting fluid, respectively. A_n is the pore area coefficient to make $A = A_n L^2$ for a regular n-gon with side length L, which is $\sqrt{3}/4$ for equilateral triangles. F_3 is $3\sqrt{3} - \pi$ as mentioned above.

2.3 Sample-Scale Equations

The equations representing a single pore are upscaled to the sample scale using an assumption of a lognormal distribution of pore sizes (e.g., Or & Tuller, 1999; Diamantopoulos & Durner, 2013). The lognormal distribution is a good approximation for the pore-size distribution of a broad range of porous materials (e.g., Diamantopoulos & Durner, 2015). The probability density function of lognormal distribution for variable pore side length (L) is:

$$f(L) = \frac{1}{L\sigma\sqrt{2\pi}} \exp\left(-\frac{[\ln(L/L_m)]}{2\sigma^2}\right) \quad (10)$$

where L_m is the mean pore side length (m) and σ is the standard deviation of ln(L).

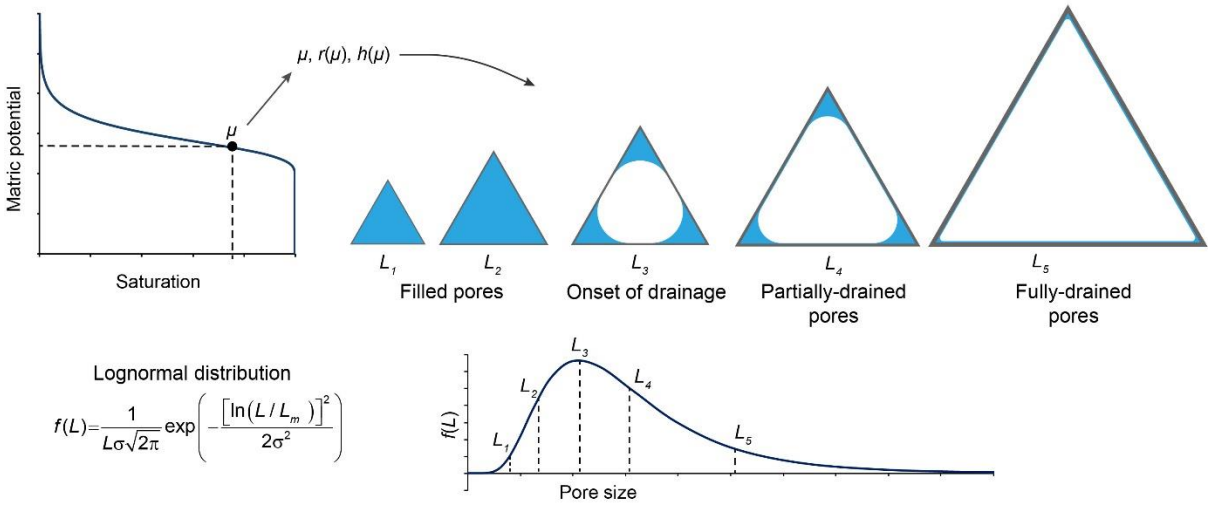

Figure 13. The liquid filling states in a porous medium under a lognormal pore size distribution and a given matric potential in a SWC curve.

The relationship between pore size, drainage, and wetting-fluid distribution is shown in Figure 4. Under a specific matric potential, pores can be fully-filled or partially-drained depending on their sizes. The critical pore size, i.e., the pore size that corresponds to the onset of drainage, can be determined as:

$$L_1 = \frac{\gamma}{\rho \mu} C_3 \quad (11)$$

where C_n is the drainage radius coefficient for any regular n-gons. The value for equilateral triangles is $C_3 = 2\left[\sqrt{3} + \sqrt{\pi/\sqrt{3}}\right]$ (Tuller & Or, 2001). The smallest pore size can be set at a random small number such as 5 nm (Or & Tuller, 1999). The largest pore side length ($L_{\max}$) corresponds to the onset of drainage for the largest pore, which is defined by the air entry matric potential μ_d. The expression for $L_{\max}$ is given in Or and Tuller (1999) and Tuller and Or (2001):

$$L_{\max} = L_1(\mu) + 2h(\mu_d) \quad (12)$$

For sample-scale saturation, the total contributions are from fully-filled pores (ducts), corner wetting fluid, and film wetting fluid. The upscaling equations of saturation as a function of matric potential yields:

$$S_w = S_{wd}(\mu) + S_{wf}(\mu) + S_{wc}(\mu) \quad (13)$$

$$S_{wd}(\mu) = \int_{L_{\min}}^{L_1(\mu)} f(L)\, dL \quad (14)$$

$$S_{wc}(\mu) = \int_{L_1(\mu)}^{L_{\max}} \frac{3F_3 r^2(\mu)}{A_3 L^2} f(L)\, dL \quad (15)$$

$$S_{wf}(\mu) = \int_{L_1(\mu)}^{L_{\max}} \frac{3h(\mu)\left[L - 2r(\mu)\cot(\pi/6)\right]}{A_3 L^2} f(L)\, dL \quad (16)$$

For sample-scale fluid-fluid interfacial area, there are only contributions from drained pores, including meniscus and film interfaces. Thus, the equations for total fluid-fluid interfacial areas are:

$$A_{nw} = A_{nwf}(\mu) + A_{nwc}(\mu) \quad (17)$$

$$A_{nwc}(\mu) = \int_{L_1(\mu)}^{L_{\max}} \frac{3\pi r(\mu)}{2A_3 L^2} f(L)\, dL \quad (18)$$

$$A_{nwf}(\mu) = \int_{L_1(\mu)}^{L_{\max}} \frac{3X_a[L - 2r(\mu)\cot(\pi/6)]}{A_3 L^2} f(L)\,dL \qquad (19)$$

The specific solid surface area (SA) is determined as:

$$SA = \int_{L_{\min}}^{L_{\max}} \frac{3XL}{A_3 L^2} f(L)\,dL \qquad (20)$$

When $X = 1$, the SA corresponds to a geometric smooth surface area.

Inspection of equation (20) shows that SA is a function of X and pore-size distribution. The total interfacial area in equation (17) attains its maximum value under ultra-high matric potentials where $X_a \rightarrow X$ and $r(\mu) \rightarrow 0$, and it is assumed to be equal to the specific surface area of the solid. Similar assumptions have been used in previous studies such as Or & Tuller (1999) and Peng & Brusseau (2005).

2.4 Limitations of Model Formulation

The use of the triangular-pore BCC approach brings some inherent limitations to the model. Specifically, the geometric smooth surface area determined with equation (20) will typically be larger than the standard geometric smooth-surface values due to the use of the simplified pore geometry. However, the present work focuses on systems with significant surface roughness and film interfacial areas. Hence, the errors in geometric surface areas associated with the BCC approach will have minimal overall impact on application of the model to most natural porous media.

The simplified fluid distribution of three menisci for each pore (Figure 3) may not be representative for all systems because of pore connectivity and merging of menisci. This effect of pore connectivity is not considered in the BCC model, which may affect calculated meniscus interfacial areas. However, this will have minimal impact on determination of total interfacial areas because the contribution of meniscus interfacial area to total interfacial area is typically very small compared to that of film interfacial area (Or & Tuller, 1999; Brusseau et al., 2006, 2007).

Irreducible wetting-fluid saturation, i.e., residual corner wetting fluid, is not present in the standard BBC model. In developing the model, we have attempted to strike a balance between model effectiveness and the number of input parameters. The focus was placed on parameters that are most critical to characterizing interfacial area behavior. Therefore, in

the interest of simplicity, no additional modification is made to incorporate residual wetting saturation. The presence of residual saturation would affect primarily meniscus interfacial area, with minimal impact on film interface.

A logistic function is used to describe X_a, which represents the relationship between interfacial area and matric potential, whereas a simpler exponential function is used for X_t (film thickness factor). While a logistic function could be used for X_t similar to the treatment of X_a, it would add additional parameters. It is also noted that X_t affects the simulation of only film saturation and has no impact on the simulation of interfacial area.

We have limited the present formulation to drainage only to focus on the measured data sets. It is straightforward to include imbibition in the BCC approach. The critical point is to determine the geometry of the pore snap-off for imbibition, which can be changed in the variable C_3 in Equation 11.

3. Applications

3.1 Model Parameterization

The model is implemented by determining values for all of the critical parameters, including the air-entry matric potential μ_d, the surface roughness factor X, the pore-size distribution parameters L_m and σ, and the micro-scale logistic parameters k and h_m. All of the applications presented herein are specific to air-water systems. The influence of these parameters, especially the surface roughness factor, on both $P_c - S_w$ and $A_{nw} - S_w$ curves is examined through a series of simulations. First, the contributions associated with film, meniscus, and duct (filled pore) to total saturation and interfacial area are examined. Second, a sensitivity analysis is conducted for the critical parameters X, L_m, and σ to illustrate their influence and effective range. Third, tests are conducted with measured $P_c - S_w$ (SWC) and air-water $A_{nw} - S_w$ data for three natural porous media to investigate the ability of the model to simulate measured data.

Measured data for the SWC curve and solid surface area are required to apply the model to a specific porous medium. The first step is to determine the air-entry matric potential (μ_d), which in this case was determined via the traditional Brooks & Corey (1964) analysis of the measured SWC curve. The optimized values for L_m, σ, and X are then

obtained in a two-step process. First, a random initial value for X is selected, and L_m and σ are optimized by application of the model to the measured SWC data. The optimized values are then substituted into equation (20), via equation (10), to derive the best value of X (with SA measured as note above). The as-obtained X is then used in place of the initial X value, and L_m and σ are optimized again. This iteration is repeated to obtain final optimized values of X, L_m, and σ. The objective function for this optimization is:

$$\Delta S_w = \sqrt{\frac{\sum_{i=1}^{n} \left(S_{wm} - S_{ws} \right)^2}{n}} \qquad (21)$$

where S_{wm} is the measured saturation and S_{ws} is the simulated saturation via equation 13. This optimization is performed with the non-linear optimization toolbox in MATLAB.

The simulation of $A_{nw} - S_w$ curves requires the function between the interfacial area factor X_a and matric potential to be determined. With the "simple-exponential" assumption for X_a proposed by Zheng et al. (2015), $X_a = X/X_t = f(P_c)$, without additional parameters. Conversely, our proposed logistic function for X_a assumes $X_a = f(P_c, k, h_m)$, with two logistic parameters, k and h_m, for the micro-scale roughness. The values of k and h_m for a porous medium can be optimized on a set of measured A_{nw} *vs* P_c data with equations (17-19). Since measured data sets are usually reported in the form of A_{nw} *vs* S_w, each measured S_w can be substituted in the fitted $P_c - S_w$ curve to derive the corresponding P_c for each measured A_{nw} data point.

The total interfacial area is also calculated using the thermodynamic-based method of Leverett (1941) for comparison with our model. The thermodynamic method is a theoretical approach to estimate total fluid-fluid interfacial areas based on the SWC curve of the porous medium. The interfacial area can be computed as:

$$A_{nw}(S_w) = \frac{n}{\gamma} \int_{S_w}^{1} P_c(s)\, ds \qquad (22)$$

where $P_c(s)$ is the capillary pressure vs saturation function and S_w is one given point on the curve, n is porosity, and γ is surface/interfacial tension.

3.2 Measured Data Sets

The efficacy of the model is tested by comparing simulated $A_{nw} - S_w$ curves with

measured data sets of total A_{nw} measured with both gas-phase and aqueous-phase IPTT methods. The combined data sets provide measured A_{nw} values for a full range of water saturation. No prior efforts to our knowledge have simulated measured data sets over this full saturation range, especially for very dry conditions ($S_w < 0.2$). The tests will evaluate if the model is able to reproduce the interfacial area over the full range of saturation, including the exponential increase observed at low saturations.

Measured data sets for three porous media are employed: Accusand 40/50, which is a commercial quartz sand, Vinton soil, a surface soil collected in Pima County, AZ, and a natural sandy material reported by Kim et al. (1997, 1999). Properties of the porous media are presented in Table 1. All three media are considered water wetting. Brusseau and colleagues (unpublished data) measured the specific solid surface area and SWC data for Accusand. The full-range of $A_{nw} - S_w$ data were collected from the gas-phase IPTT measurements reported by Peng and Brusseau (2005), the aqueous-phase IPTT measurements reported in Brusseau et al. (2015), and the mass-balance (MB) surfactant tracer measurements reported in Araujo et al. (2015). For Vinton soil, the specific solid surface area and SWC curve were reported by Peng & Brusseau (2012). Combined data from aqueous-phase and gas-phase IPTT were reported in Costanza-Robinson & Brusseau (2002), Peng & Brusseau (2005), and Brusseau et al. (2007). In addition, another data set of combined gas-phase and aqueous-phase IPTT measurements along with the specific solid surface area and SWC curves, reported by Kim et al. (1997, 1999), was selected.

The measured specific solid surface areas for Vinton (soil) and the other two materials (sand) differ by more than an order of magnitude, providing favorable conditions for evaluating the effect of surface roughness on interfacial area. It is noted that the largest measured air-water interfacial areas obtained with the gas-phase IPTT method for all three media are consistent with specific solid surface areas measured by the nitrogen-BET method. This consistency provides verification of the accuracy of the gas-phase IPTT data and illustrates the significant impact of surface roughness on interfacial area.

Table 3. Physical properties of the selected porous media.

Medium	Mean diameter d_m (mm)	Porosity n	Bulk density (g/cm^3)	Specific solid surface area (cm^{-1})[a]	Smooth-surface surface area (cm^{-1}) [b]	Air-entry matric potential μ_d (cm)[c]

Accusand	0.350	0.42	1.65	2800	99.4	14.6
Vinton	0.234	0.46	1.46	51684	138.5	22.3
Kim et al. [d]	0.250	0.36	1.72	2000	153.6	24.3

[a]All data were measured via the nitrogen-BET method.

[b]Determined with the commonly-used expression of the specific solid surface area assuming smooth-spherical media, calculated as $6(1\text{-}n)/d_m$.

[c]Calculated by the Brooks & Corey method.

[d]Reported in Kim et al. (1997, 1999).

4. Results

4.1 Example Simulations

An example set of simulations of both drainage $P_c - S_w$ and $A_{nw} - S_w$ curves for an air-water system is presented in Figure 5, showing the contributions from film, corner, and duct (filled-pore) water for surface roughness factors X = 10 and 1000. Fully-filled pores are the primary contributor to total water saturation, as expected. Film and corner water both contribute a small amount to total saturation, but at X = 10, the film-associated saturation is very low. The $A_{nw} - S_w$ curves are similar to the examples presented in Or and Tuller (1999) and Brusseau et al. (2007), in which film-associated interfacial area surpasses the meniscus area by more than one order of magnitude at almost all saturation values. The calculated meniscus (corner) interfacial area in Figure 5b may be overestimated because the BCC model neglects pore connectivity. Nevertheless, it is several orders of magnitude smaller than the film interfacial area for both X = 10 and 1000. The uncertainty in total interfacial area due to pore-connectivity effects on simulated meniscus interface can be calculated from the magnitude of meniscus interfacial area in Figure 5b.

Increasing the roughness factor by 100 results in changes in both the $P_c - S_w$ and $A_{nw} - S_w$ functions. The impact of surface roughness on the $P_c - S_w$ curves is relatively small because of the small volume of film-associated water. Conversely, X has a much greater influence on the $A_{nw} - S_w$ relationship. The total interfacial area ranges from 0.5 to 2 logs greater for X = 1000 compared to X = 10. The significant increase in interfacial area is observed only for the film contribution, consistent with the fact that surface roughness only

affects the film-associated interfaces.

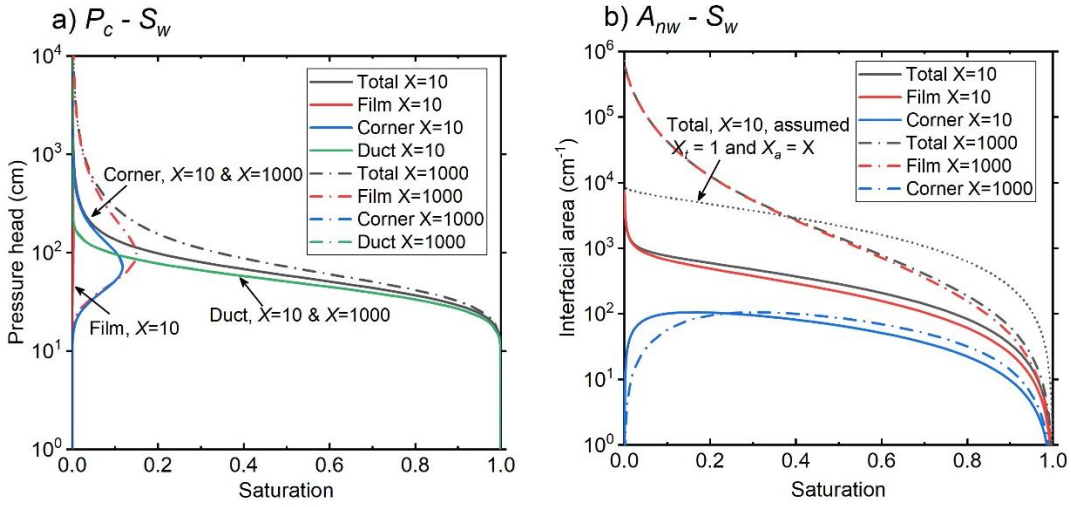

Figure 14. Example calculations of the contributions from duct (filled pores), film, and corner water to the total saturation and air-water interfacial area, with $X = 10$ and $X = 1000$ and other parameters fixed. The input parameters are set at L_m = 90 μm, σ = 0.5, μ_d = -1 J/kg, k = 1, and h_m = 2 nm.

4.2 Sensitivity Analysis

A sensitivity analysis was conducted following the example simulations in section 4.1 by varying the parameters X, L_m, and σ over broader ranges. All default parameters are the same as used for the simulations in section 4.1 unless otherwise specified. The resulting drainage $P_c - S_w$ and $A_{nw} - S_w$ curves are shown in Figure 6.

The $P_c - S_w$ curves are generally not very sensitive to the roughness factor X, but a rougher solid surface does have a relatively higher capability to retain water, causing the $P_c - S_w$ curve to shift slightly upward. In contrast, the $P_c - S_w$ curves are more sensitive to L_m and σ as would be anticipated. Increasing the mean pore size leads to less filled pores for a given matric potential and decreases the fluid retention of the medium. The standard deviation controls the dry-end and wet-end of the simulated $P_c - S_w$ curves. Increasing σ makes the curve "narrower" and sometimes yields a maximum saturation lower than 1 due to the fixed air-entry potential.

The simulations presented in Figure 6 clearly demonstrate that the presence of solid surface roughness, i.e., $X > 1$, increases the magnitude of film interfacial area compared to

the case of a smooth surface ($X = 1$). Larger X values produce larger interfacial areas for a given set of conditions, as a larger X represents a larger specific solid surface area due to greater magnitude of surface roughness. These results are consistent with prior experiment-based studies that have reported larger interfacial areas for media with greater surface roughness (Costanza and Brusseau, 2000, 2002; Peng and Brusseau, 2005; Brusseau et al., 2008,2009,2010,2015; Costanza-Robinson et al., 2008; Zhong et al., 2016).

The sensitivity of interfacial area curves to the roughness factor is complicated. Inspection of the linear-scale insert of Figure 6a shows that the $A_{nw} - S_w$ functions for media with smooth surfaces ($X = 1$) are essentially linear over the full saturation range. The curve for this condition defines one theoretical limiting case for the $A_{nw} - S_w$ function, establishing the minimum values of A_{nw} for a given porous medium. Note that this case is functionally equivalent to the theoretical case wherein the wetting films are sufficiently thick to produce smooth film interfaces for all S_w. The special case wherein the surfaces are rough and the thicknesses of the wetting films remain sufficiently thin such that the effect of roughness remains at its maximum for all S_w (i.e., $X_t = 1$ and $X_a = X$) defines the other theoretical limiting case, establishing the maximum A_{nw} values. An example of this second case is provided in Figure 5b for $X = 10$ with the constraint $X_t = 1$ and $X_a = X$, and other parameters the same as for the original simulation. It is observed that A_{nw} values for this case are larger than for the $X = 1000$ simulation at $S_w > 0.4$, even though the latter system has an equivalent 100-times greater surface roughness. The actual $A_{nw} - S_w$ function observed for a given porous medium will typically reside somewhere between the two limiting cases. This is illustrated by the observation that the A_{nw} values produced for the original $X = 10$ simulation are an order of magnitude smaller than those for the theoretical maximum simulation. This is a result of thicker wetting films partially masking the impact of roughness on film interfacial area.

Generally, all A_{nw} curves with $X > 1$ greatly increase at a certain saturation due to the impact of surface roughness causing an exponential increase of film-associated interface. For a given set of conditions, the critical saturation is smaller for smaller X (Figure 6). The impact of surface roughness on A_{nw} is masked to some degree at higher saturations because of the presumed presence of thicker wetting films. This masking effect is greater for smaller X for a given set of conditions. The degree to which surface-roughness impacts are masked, and the resultant shape of the $A_{nw} - S_w$ curve, for a given medium will depend upon its fluid-retention characteristics and the nature of the surface roughness, and how they

influence pore-scale wetting-fluid distribution and configuration. More detailed discussions of the roughness factor and natural grain surfaces are given in section 5.

For the analyses of the effect of L_m and σ, two reference simulations with smooth media ($X = 1$) were first performed, and the subsequent simulations for rough media ($X = 50$) were set within the parameter range of the reference simulations. As expected, decreasing L_m increases SA due to smaller grain size, which results in larger A_{nw} for the full-range of saturations. These results are consistent with prior experiment- and model-based studies that have reported larger interfacial areas for media with smaller grain diameters (Cary, 1994; Anwar et al., 2000; Costanza and Brusseau, 2000, 2002; Cho and Annable, 2005; Dobson et al., 2006; Schnaar and Brusseau, 2006; Brusseau et al., 2008,2009,2010; Zhong et al., 2016). The relative impact of surface roughness on A_{nw} is greater for smaller L_m, as illustrated by comparing the two sets of simulations for $X = 1$ and $X = 50$ for $L_m = 10$ versus 160 μm (Figure 6b). For $L_m = 10$, the difference in A_{nw} for $X = 1$ and $X = 50$ is greater than 0.5 log for $S_w < 0.9$. Conversely, the difference in A_{nw} is very small until much lower S_w for $L_m = 160$. These results reflect the relationship between surface area and grain size, wherein the magnitude of L_m (i.e., pore size) correlates to grain size.

Increasing the pore-size standard deviation for smooth media only slightly increases SA, but it causes the $A_{nw} - S_w$ function to become more nonlinear for larger σ (Figure 6c). For rough media, the influence of σ is similar to that observed for the $P_c - S_w$ curves, where increasing σ simultaneously increases the low-saturation A_{nw} for $S_w < 0.3$ and decreases the medium-to-high-saturation A_{nw} at $S_w > 0.3$. Similar to the L_m simulations, it is observed that the deviation between the $A_{nw} - S_w$ curves for the $X = 1$ and $X = 50$ cases is greater for $\sigma = 1.2$ than for $\sigma = 0.1$ at low saturation. This reflects the greater proportion of smaller pores present with larger pore-size (grain-size) distributions. Inspection of the insert in Figure 6c shows that the magnitudes of the impact of σ are relatively smaller than those of X and L_m.

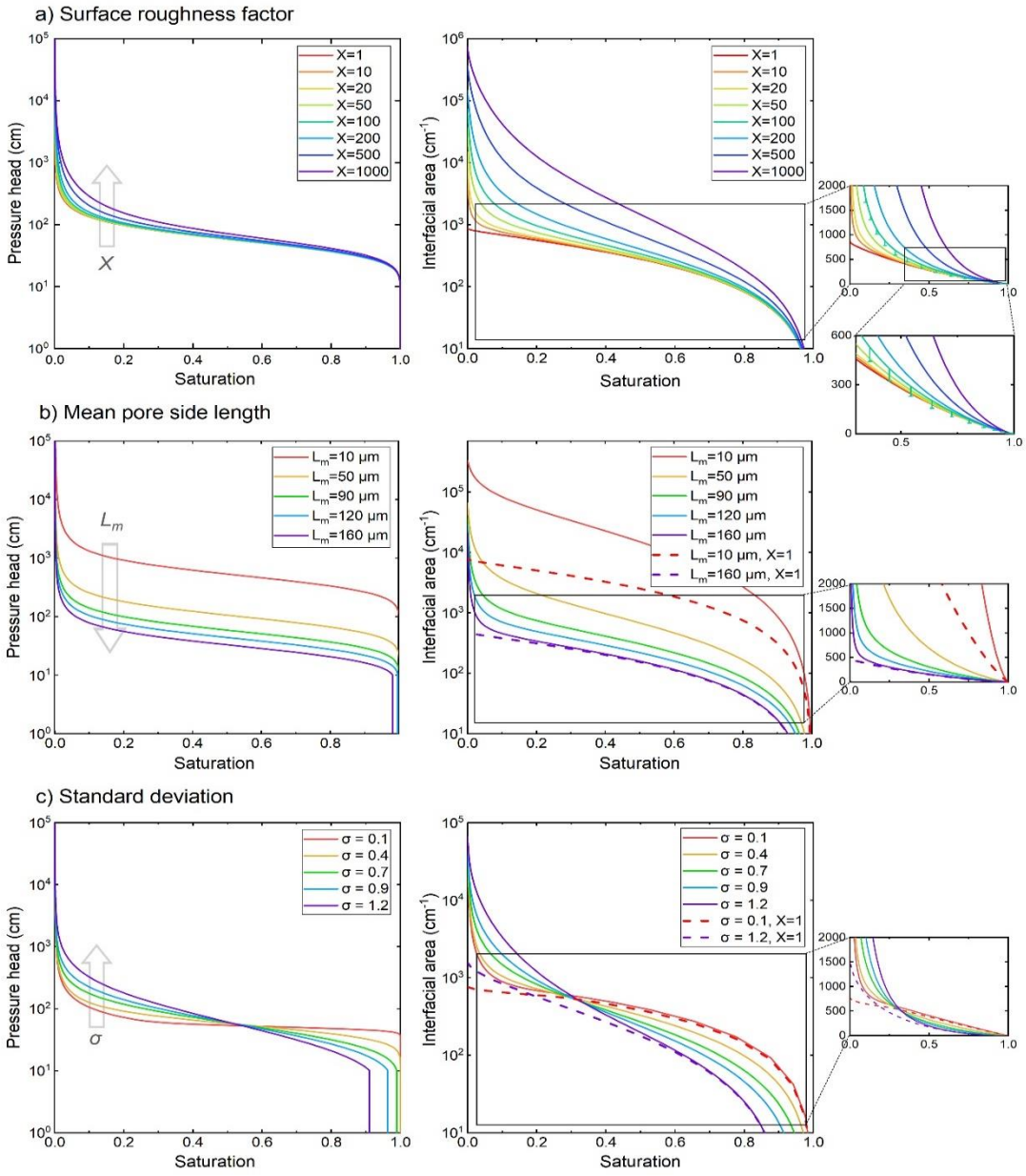

Figure 15. Sensitivity analysis of the roughness-modified BCC model for drainage matric potential curves and total interfacial area curves on logarithmic scales. The default parameter values for all cases are $X = 50$, $L_m = 90$ μm, $\sigma = 0.5$, $\mu_d = -1$ J/kg, $k = 1$, and $h_m = 2$ nm unless specified otherwise. Adjusted parameters are (a) surface roughness factor; (b) mean pore side length (with two dashed reference curves for the maximum and minimum inputs, respectively, under the same conditions except with $X = 1$) (c) standard deviation (with the same reference curves as (b) for the maximum and minimum inputs). Each interfacial-area figure has an amplified insert showing the curves on linear scales for

A_{nw} < 2000 cm^{-1}. The A_{nw} insert in Figure 6a has a further magnification for saturations over 30%, and the errors due to meniscus-interfaces on the X = 100 curve are marked.

4.3 Tests with Measured Data

The results for model testing with the three measured data sets are shown in Figure 7. The left column in Figure 7 presents the final fit of the SWC curves. The optimized curves produce good matches to the measured data for high and medium saturations, but do not match the measured data at the lowest saturations primarily because residual saturation is not incorporated. Following the methodology in section 3.1, the results for roughness factor X and pore size parameters L_m and σ of the three media are presented in Table 2. Inspection of Table 2 shows that L_m is smallest for Vinton, intermediate for the Kim sand, and largest for Accusand. This is consistent with the mean grain diameters of the three media. Diamantopoulos et al. (2016) tested a lognormal triangular-BCC model without surface roughness using the same SWC data reported for Vinton soil in Brusseau et al. (2006), yielding values of L_m = 90 μm and σ = 0.9. Their values are similar to ours.

Table 4. Pore size distribution and surface roughness-controlling parameters of the selected soil samples.

Medium	Mean pore side length L_m (μm)	Standard deviation σ	Surface roughness factor X	Growth rate factor k	Critical adsorptive film thickness h_m (nm)
Accusand	212.7	0.303	8.7	3.0	10
Vinton	93.6	0.685	58	1.8	5.2
Kim et al.	171.0	0.164	5.0	2.1	6.3

The model simulations of $A_{nw} - S_w$ incorporating the logistic parameters k and h_m are presented in the right column of Figure 7. It is observed that the model simulations provide good matches to the measured data over the entire saturation range for the accusand and Vinton media. Conversely, the simulated curve over-predicts measured A_{nw} values at mid-to-high saturations for the Kim et al. data. This may reflect in part greater uncertainty in

the model representativeness of the pore structure for this latter system. In addition, it is noted that this medium has the smallest interfacial areas and surface-roughness effects, conditions for which errors in representing the pore structure and smooth surface area would have the most impact.

The measured and simulated interfacial areas for Vinton soil are much greater than for the two sands. Vinton soil has a much larger X compared to the other two media (Table 2), consistent with its much larger specific solid surface area a measured by the nitrogen-BET method (Table 1). Hence, these results illustrate that X controls the overall magnitude of total interfacial area. It is further observed that the logistic parameters k and h_m also influence the impact of surface roughness on A_{nw}. They are correlated to the surface-roughness masking phenomenon described in the discussion of Figures 5 and 6. The k term controls the slope of the $A_{nw} - S_w$ curves for the exponential-increase stage, and h_m determines the critical saturation at which A_{nw} begins to increase exponentially. Inspection of Table 2 shows that k and h_m vary somewhat amongst the three test materials, most likely reflecting differences in the specific structure of surface roughness. Therefore, a minimum of three controlling parameters (X, k and h_m) are needed to quantify the surface-fluid interactions on rough surfaces, and all three are intrinsic properties of the porous medium. Among them, X represents the overall magnitude of surface roughness (roughness capacity), whereas k and h_m are parameters representing the micro-scale structure of surface roughness and its interactions with wetting fluid (and ultimately the resultant impact on interfacial area).

For comparison, Figure 7 also shows the simulations obtained through the simple-exponential equation via $X_a = X/X_t$, where X_t is defined by the exponential equation (3). Both simulated curves are consistent and reasonably match the measured interfacial-area data at medium to high saturations ($S_w > 0.5$) for the sand and Vinton soil. However, the measured exponential increases at low saturations are only accurately characterized by incorporating the two logistic parameters k and h_m. The two simulations are very similar over the majority of the saturation range for the Kim data; however, both simulations deviate from the measured data at higher saturations. These errors exceed the range of menisci uncertainties (at about -10%), and may be attributed to the simplified triangular pore geometry, as noted above, and to possible uncertainties in the measured Kim et al. aqueous-phase IPTT data discussed by the original authors.

The $A_{nw} - S_w$ results obtained with the thermodynamic method are also shown in Figure

7. It is clear that the thermodynamic method greatly underestimates both measured and simulated data sets at lower saturations. The limitations of the base thermodynamic method have been discussed in prior studies, which noted that the method may oversimplify the energy exchange and solid-fluid interactions in real porous media (e.g., Leverett, 1941; Dobson et al., 2006; Grant & Gerhard, 2007; Schroth et al., 2008). If the thermodynamic estimation is considered to provide a first-order representation of the $A_{nw} - S_w$ function for smooth-surface media, the results suggest that Accusand and Vinton have less roughness masking compared to the Kim sand. These results illustrate that the surface-roughness masking effect is different for different porous media.

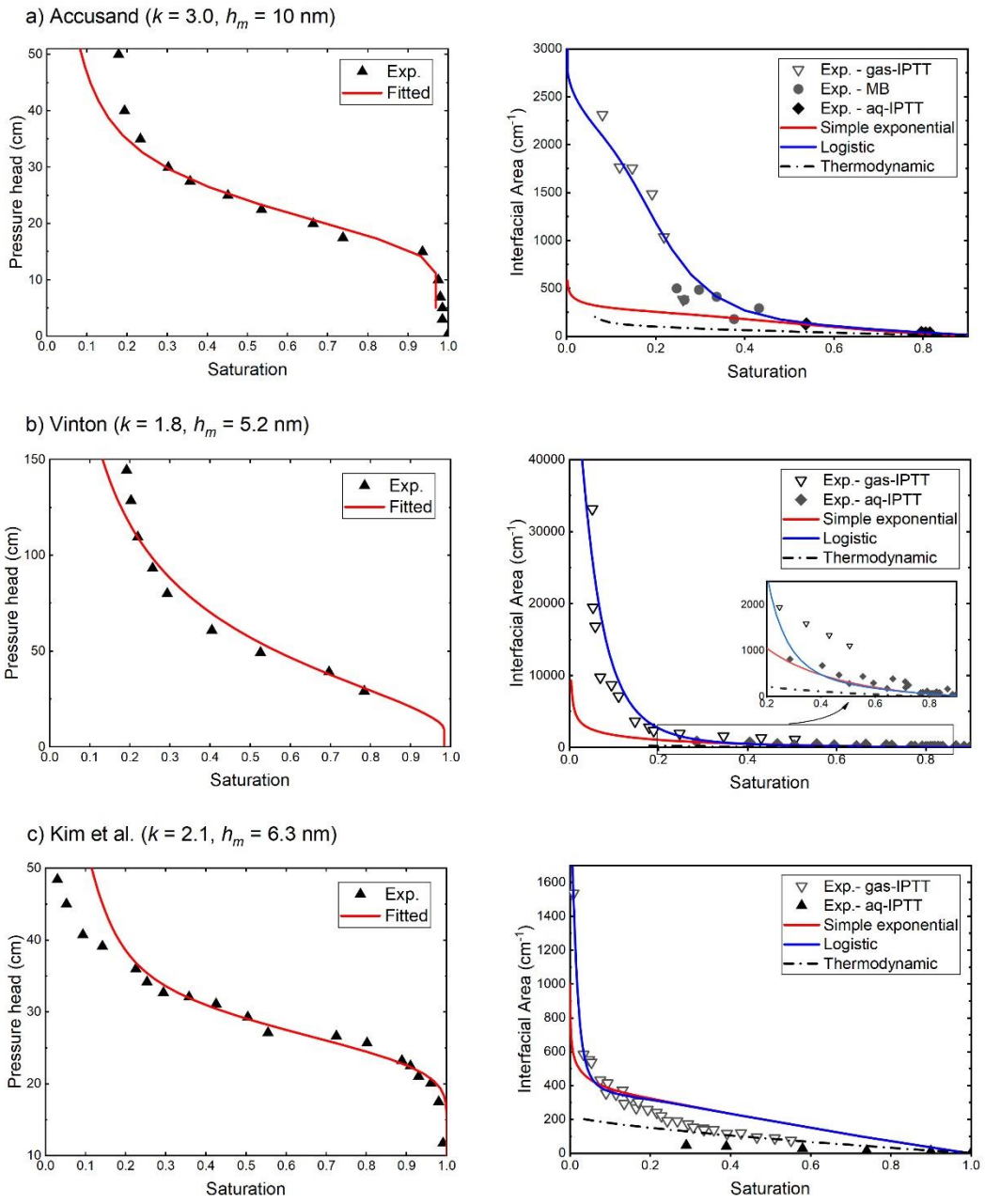

Figure 16. Model simulations of the $P_c - S_w$ and $A_{nw} - S_w$ curves compared to measured data for three natural porous media using the simple-exponential and logistic assumptions for the interfacial area factor X_a. Results produced by the thermodynamic estimation method are also plotted.

4.4 Validity of Model Assumptions

Inspection of Figure 7 shows that the optimized curves do not fully match the measured data at the lowest (< 0.2) saturations for the $P_c - S_w$ data, which may indicate limitations associated with model assumptions (e.g., simplified pore geometry and fluid distribution, no residual saturation). However, the determination of model parameters L_m, σ, and X, is controlled primarily by the higher-saturation (> 0.2) data range. Furthermore, determination of parameters k and h_m are based on application to the $A_{nw} - S_w$ data. Thus, any potential model limitations affecting simulation of the $P_c - S_w$ data do not significantly influence determination of interfacial area. This is supported by the excellent matches obtained between the simulated and measured curves for the $A_{nw} - S_w$ data in Accusand and Vinton.

The model assumptions of simplified pore geometry and fluid distribution and of no residual wetting fluid affect primarily the meniscus interfacial area. As discussed above, film-associated interfacial area dominates total fluid-fluid interfacial area at essentially all saturations. Thus, potential uncertainty in meniscus area will have minimal impact on determination of total interfacial area, the focus of this study.

The $P_c - S_w$ function is not very sensitive to surface roughness and wetting-film status, given the relatively small fluid volumes involved. In addition, as noted above, there can be uncertainty in simulation of this function at lower saturations. Thus, our approach of treating X_a independent from X_t and determining it from the $A_{nw} - S_w$ data appears to be robust.

5. Discussion

5.1 The Masking of the Surface Roughness Effect

The illustrative results in Figures 5-7 all indicate that surface roughness can have a substantial impact on the magnitude of air-water interfacial area. As discussed above, the impact may be masked to some extent depending upon media properties and fluid conditions. The masking phenomenon is illustrated in linear-scale coordinates in Figure 8. The two limiting cases for the $A_{nw} - S_w$ function are shown as the “maximum roughness” and “smooth surface” curves. The curve for the smooth surface ($X = 1$) is anchored to the

smooth solid surface area for $S_w = 0$. Curves for $X > 1$ are anchored to the actual (rough) solid surface area. The dashed curves in Figure 8 demonstrate the maximum roughness effect on the $A_{nw} - S_w$ function for a given medium, where all of the wetting films are thin at all S_w ($X_t = 1$ and $X_a = X$). The surface roughness effect can be obscured if the wetting film is sufficiently thick. The solid curves in Figure 8 represent one possible realization of the actual drainage $A_{nw} - S_w$ function, wherein the impact of surface roughness is masked to some degree compared to the maximum-roughness curves.

The typical $A_{nw} - S_w$ curve is "L"-shaped in linear coordinates, with a flat linear stage at higher saturations and a steep exponential stage at lower saturations. Surface roughness may be considerably masked by thick wetting films in the linear stage, causing the actual $A_{nw} - S_w$ curve to reside closer to the theoretical smooth-surface curve. In the exponential stage, the decreasing wetting-film thickness causes an enormous increase in the magnitude of fluid-fluid interfacial area such that the actual $A_{nw} - S_w$ curve approaches the theoretical maximum curve. The nature of surface roughness and its interaction with wetting fluid determines the relative proportion of linear and exponential stages over the full saturation range. From the simulations of the measured data presented in Figure 7, it can be observed that different materials have different proportions of linear and exponential stages. For instance, the linear range for Kim's sand extends to ~30% saturation, whereas it extends to only ~70%-80% for Accusand and Vinton. Such results indicate that the masking of surface roughness is more significant for Kim's sand than for Accusand and Vinton soil.

As noted above, the degree to which surface-roughness impacts are masked and the resultant shape of the $A_{nw} - S_w$ curve for a specific porous medium will depend upon the interplay between wetting-film configuration, matric potential (saturation), and surface roughness. The shape of the $A_{nw} - S_w$ curves can be explained in accordance with the five controlling parameters in the model: L_m, σ, X, k, and h_m. The lognormal pore-size-distribution parameters L_m, and σ define the geometric base solid surface area and determine the location of the smooth-surface fluid-fluid interfacial area curve. Combining the surface roughness factor X with the smooth-surface curve defines the maximum-roughness fluid-fluid interfacial area curve for a given medium. These two limiting curves determine the full range of possible outcomes of surface roughness effects on fluid-fluid interfacial area for a specific medium. The parameters k and h_m, which represent the micro-structure of solid surfaces and its interaction with wetting fluid, influence the shape of the curve within the limiting range and the proportion of the linear and exponential stages. For

media with rough solid surfaces, the $A_{nw} - S_w$ curve will always reside between the smooth-surface curve and the maximum-roughness curve, and the magnitudes of the three roughness-related parameters (X, k, and h_m) will mediate the overall impacts of surface roughness on A_{nw} under different matric potentials (wetting saturations) and thus the overall shape of the $A_{nw} - S_w$ curve.

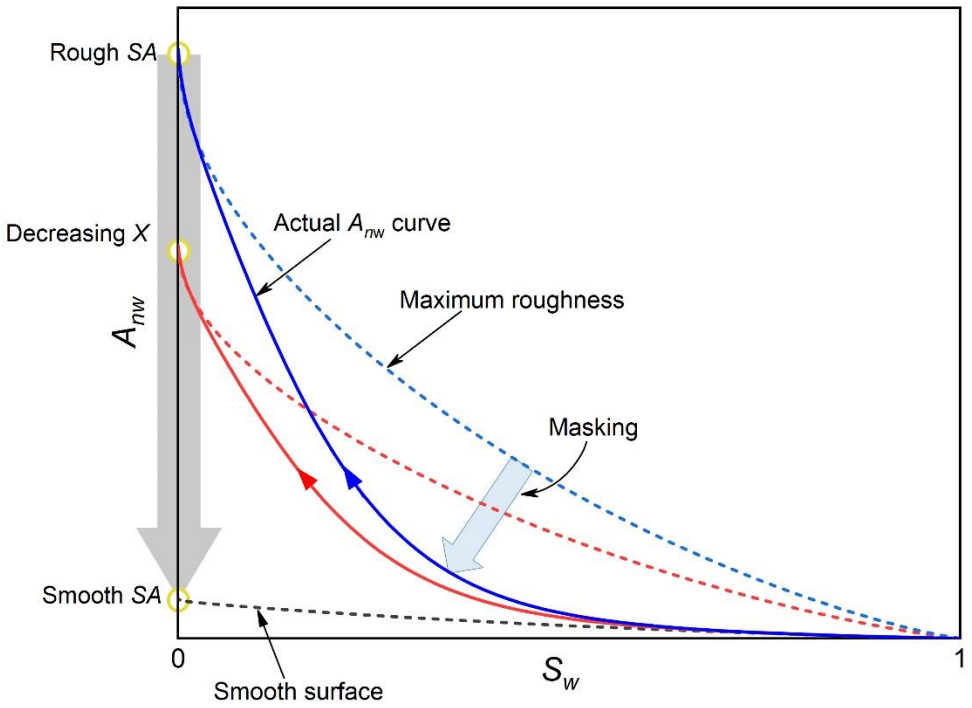

Figure 17. Illustration of the masking phenomenon of the surface roughness effect on $A_{nw} - S_w$ curves. The blue and red curves represent two media with different magnitudes of surface roughness, but the same smooth surface area (SA).

The following strategies can be implemented to improve the characterization of surface roughness effects on nonwetting-wetting interfaces. First, increase the extent of drainage to reach as low a saturation as possible. This will entail the use of additional measurement methods beyond the standard ones typically used to determine soil-water characteristic curves (e.g., Arthur et al., 2013). Second, test various porous media with a broad range of physical properties. One major implication of this work is that natural soils and sediments are anticipated to exhibit a great range of properties and associated $A_{nw} - S_w$ behavior. Thus, we would expect that the importance of film-associated interfacial area and

the impacts of surface roughness to vary from media to media. Third, use a definition of surface roughness that compares the rough and geometric solid surface areas under different scales, rather than only a single absolute value of specific surface area or relative height (root-mean-square roughness).

5.2 Relating Surface Roughness Effect to Solid Surface Micro-structure

The impact of surface roughness on the $A_{nw} - S_w$ function can be explained using concepts of fractal geometry. In the scheme of a fractal surface (Figure 9), there are multiple layers of roughness structures within a defined space. The primary roughness layer, as indicated by the root mean square roughness (R_{rms}), is quantifiable by traditional measurements. For natural materials, its spatial scale is usually in the range of 0.1~1 μm or even larger (e.g., Tokunaga et al., 2003; Alshibli & Alsaleh, 2004; Adams et al., 2012; Kim et al., 2012; Kibbey, 2013; Araújo & Brusseau, 2019). At higher water saturations, the film thickness can be close to the magnitude of the primary roughness layer (Philip, 1978; Kim et al., 2012; Kibbey, 2013; Zheng et al., 2015). Under this condition the smaller-scale roughness does not impact film interfacial area. Conversely, adsorbed wetting-film thickness under low-saturation conditions can be 1~10 nm (Tokunaga et al., 2003; Resurreccion et al., 2011; Tokunaga, 2011), which can be several orders of magnitude smaller than the scale of the primary roughness. When the wetting film thickness is reduced to the scale of a certain roughness layer, as shown in the inset of Figure 9, it reflects the micro-scale surface topography. The transition between scales causes the film interfacial area to increase dramatically, resulting in the exponential stage of the $A_{nw} - S_w$ function. When S_w approaches zero, the film attains the fractal dimensions of the solid surface, where the thickness factor $X_t = 1$ and the interfacial area factor $X_a = X$. These sub-levels of roughness are regarded as "micro-scale roughness" in the present study in distinction to traditional root-mean-square surface roughness (R_{rms}).

The role of the surface roughness factor X can be further interpreted in accordance with the fractal nature of the solid surface. In this case, X can be viewed to represent the potential of surface fractal growth, i.e., the potential for existence of additional scales of roughness that will typically be operationally defined by specific measurement methods (such as nitrogen-BET). The logistic parameters k and h_m reflect the impact of solid fractal structures on the disposition of liquid films. The exponential growth-rate parameter k may

indicate the fractal complexity of the surface roughness, especially the difference of average heights between two adjacent roughness layers. The critical adsorptive film thickness h_m –corresponding to a specific matric potential– may represent the average micro-scale triggering point of the exponential increase of film interfaces. The parameters k and h_m relate to the masking of surface roughness by wetting films, and can be used to quantify the degree of masking. The impacts of the three parameters X, k, and h_m are superimposed on the absolute magnitude of solid surface available, which is controlled by the texture of the porous medium (mean grain size, grain-size distribution).

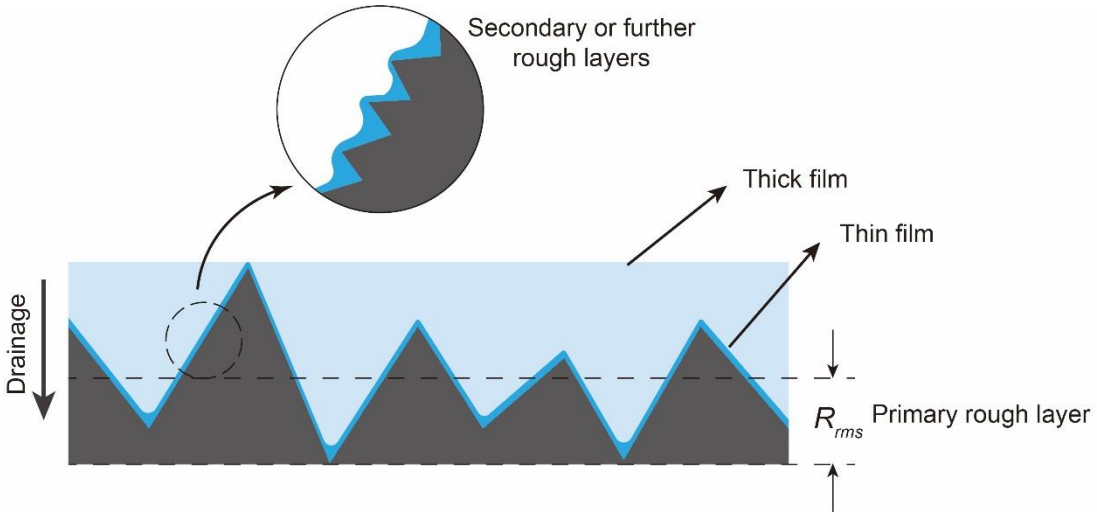

Figure 18. Scheme of a rough solid surface with multiple layers of roughness. The root-mean-square roughness defines the roughness of the primary layer. When matric potential increases, the water film thickness may reduce to the scale of the secondary or further micro-roughness levels, which provides additional surface and interfacial areas.

5. Conclusions

A triangular-pore BCC-based model with explicit representation of surface roughness was developed to characterize the impacts of surface roughness on fluid-fluid interfaces in porous media. The model can compute both the film and meniscus $A_{nw} - S_w$ profiles for a specified porous medium under the assumption of a lognormal pore-size distribution. The model contains three roughness-related parameters: the solid surface roughness factor X,

and the micro-scale film-interface parameters k and h_m, which are all considered to be inherent properties of the porous medium.

The results demonstrated that the model is able to reproduce measured air-water interfacial area data across a full-saturation range, which was not examined in previous modeling studies. The simulations also showed that the exponential increases in A_{nw} measured with the gas-phase IPTT method can be explained by the impact of surface roughness on film-associated interfacial area. While the applications presented herein were specific to air-water systems, the model and reported outcomes are relevant for any nonwetting-wetting fluid pairs. The significance of solid surface properties in mediating fluid-fluid interfacial area observed in this study is consistent with prior research illustrating the role of surface properties on vapor adsorption, water evaporation, and soil-water retention at very high matric potentials (e.g., Shahraeeni and Or, 2012; Song and Boily, 2013; Leao and Tuller, 2014).

The degree to which fluid-fluid interfacial area is influenced by roughness is a function of fluid-retention characteristics and the nature of the rough surfaces, which mediate the distribution and configuration of wetting fluid within the pores and on the surfaces of the solids. The $A_{nw} - S_w$ function observed for a particular porous medium ranges between an upper theoretical maximum, defined for the case wherein the wetting films remain thin for all S_w, and the lower theoretical minimum defined for the case of smooth solid surfaces (and equivalently wherein wetting films remain sufficiently thick for all S_w). The specific behavior is defined with the five controlling parameters in the model: L_m, σ, X, k, and h_m.

The lognormal pore-size-distribution parameters L_m, and σ define the geometric base solid surface area and determine the location of the smooth-surface fluid-fluid interfacial area curve. The surface roughness factor X superimposed on the smooth-surface curve determines the maximum-roughness curve for a given medium. These two limiting curves define the full range of possible outcomes of surface roughness effects on fluid-fluid interfacial area for a specific medium. The parameters k and h_m, which represent the micro-structure of solid surfaces and its interaction with wetting fluid, mediate the shape of the curve within the limiting range and the proportion of the linear and exponential stages. The influence of wettability, solution chemistry, and other factors is implicitly incorporated in the model through these parameters. Sensitivity analyses were conducted for L_m, σ, and X to examine their influence on system behavior. Because of their hypothesized relationship

to the specific nature of surface roughness, we have reserved detailed analysis of k and h_m to a future study wherein the model will be applied to a larger number of porous media beyond the three used in the present study.

The impact of surface roughness on fluid-fluid interfacial area for natural porous media is likely to be masked to some degree due to the presence of wetting films. The extent to which this masking phenomenon occurs will depend on the specific properties of the medium as well as fluid conditions, as illustrated by the results presented herein for the simulation of the measured data sets. It is anticipated that natural porous media will display a wide range of masking potentials considering the extreme variability in physical and geochemical properties exhibited across the spectrum of soils and sediments.

The triangular-pore BCC approach used in this work has limitations that may impose constraints to the representativeness for some systems. This may lead to uncertainties in the magnitudes of simulated meniscus interfaces, the geometric solid surface area, and the fitting of SWC curves at low saturations. However, these potential uncertainties do not limit the capability of the model to characterize the impact of surface roughness on fluid-fluid interfacial area, as shown by application to the measured data sets presented herein. Some of the assumptions used in the present study can be relaxed, for example by implementing consideration of pore-connectivity or effects of non-zero contact angles. In addition, the model can be extended to characterize the imbibition A_{nw} curves by modifying the pore geometry for the onset of pore snap-off.

The modeling approach presented can be used to characterize a broad range of porous media with different solid surface structures. In principle, the $A_{nw} - S_w$ function can be viewed as a "surface-film characteristic curve", containing information about the properties of surface roughness and solid (surface)–fluid (film) interactions. The surface-film characteristic curve can serve as a quantitative approach to characterize rough surfaces, and simulate the associated wetting films in pore-space modeling. This approach is anticipated to provide additional insight into surface roughness effects on porous-media systems.

Acknowledgements

This research was supported in part by a grant from the NIEHS Superfund Research

Program (P42 ES04940). No new measured data sets are used in this work. The measured data sets used are available in the cited prior-published works. We thank the reviewers and editors for their constructive comments.

References

Adams, T., Grant, C., & Watson, H. (2012). A simple algorithm to relate measured surface roughness to equivalent sand-grain roughness. Journal ISSN, 2929, 2724.

AlRatrout, A., Blunt, M. J., & Bijeljic, B. (2018). Wettability in complex porous materials, the mixed-wet state, and its relationship to surface roughness. Proceedings of the National Academy of Sciences, 115(36), 8901–8906.

Alshibli, K. A., & Alsaleh, M. I. (2004). Characterizing surface roughness and shape of sands using digital microscopy. Journal of Computing in Civil Engineering, 18(1), 36–45.

Araujo, J. B., Mainhagu, J., & Brusseau, M. L. (2015). Measuring air–water interfacial area for soils using the mass balance surfactant-tracer method. Chemosphere, 134, 199–202.

Araújo, J. B., & Brusseau, M. L. (2019). Novel fluid–fluid interface domains in geologic media. Environmental Science: Processes & Impacts.

Arthur, E., Tuller, M., Moldrup, P., & de Jonge, L. W. (2013). Rapid and Fully Automated Measurement of Water Vapor Sorption Isotherms: New Opportunities for Vadose Zone Research. Vadose Zone Journal, 13(1). https://doi.org/10.2136/vzj2013

Beyhan, S., Bilecen, K., Salama, S. R., Casper-Lindley, C., & Yildiz, F. H. (2007). Regulation of rugosity and biofilm formation in Vibrio cholerae: comparison of VpsT and VpsR regulons and epistasis analysis of vpsT, vpsR, and hapR. Journal of Bacteriology, 189(2), 388–402.

Blunt, M. J. (2001). Flow in porous media—pore-network models and multiphase flow. Current Opinion in Colloid & Interface Science, 6(3), 197–207.

Bradford, S. A., & Leij, F. J. (1997). Estimating interfacial areas for multi-fluid soil systems. Journal of Contaminant Hydrology, 27(1–2), 83–105.

Brangari, A. C., Sanchez-Vila, X., Freixa, A., Romani, A. M., Rubol, S., & Fernandez-Garcia, D. (2017). A mechanistic model (BCC-PSSICO) to predict changes in the hydraulic properties for bio-amended variably saturated soils. Water Resources Research, 53, 93–109. https://doi.org/10.1029/eo066i003p00017-03

Brooks, R., & Corey, T. (1964). HYDRAU uc properties of porous media. Hydrology

Papers, Colorado State University, 24, 37.

Brown, S. R. (1987). Fluid flow through rock joints: the effect of surface roughness. Journal of Geophysical Research: Solid Earth, 92(B2), 1337–1347.

Brusseau, M. L., Narter, M., Schnaar, G., & Marble, J. (2009). Measurement and estimation of organic-liquid/water interfacial areas for several natural porous media. Environmental Science and Technology, 43(10), 3619–3625. https://doi.org/10.1021/es8020827

Brusseau, Mark L., Janousek, H., Murao, A., & Schnaar, G. (2008). Synchrotron X-ray microtomography and interfacial partitioning tracer test measurements of NAPL-water interfacial areas. Water Resources Research, 44(1), 1–9. https://doi.org/10.1029/2006WR005517

Brusseau, Mark L, Peng, S., Schnaar, G., & Costanza-Robinson, M. S. (2006). Relationships among air-water interfacial area, capillary pressure, and water saturation for a sandy porous medium. Water Resources Research, 42(3).

Brusseau, Mark L, Peng, S., Schnaar, G., & Murao, A. (2007). Measuring air− water interfacial areas with x-ray microtomography and interfacial partitioning tracer tests. Environmental Science & Technology, 41(6), 1956–1961.

Brusseau, Mark L, Narter, M., & Janousek, H. (2010). Interfacial partitioning tracer test measurements of organic-liquid/water interfacial areas: application to soils and the influence of surface roughness. Environmental Science & Technology, 44(19), 7596–7600.

Brusseau, Mark L, El Ouni, A., Araujo, J. B., & Zhong, H. (2015). Novel methods for measuring air–water interfacial area in unsaturated porous media. Chemosphere, 127, 208–213.

Cary, J. W. (1994). Estimating the surface area of fluid phase interfaces in porous media. Journal of Contaminant Hydrology, 15(4), 243–248.

Cassie, A. B. D., & Baxter, S. (1944). Wettability of porous surfaces. Transactions of the Faraday Society, 40, 546–551.

Celia, M. A., Reeves, P. C., & Ferrand, L. A. (1995). Recent advances in pore scale models for multiphase flow in porous media. Reviews of Geophysics, 33(S2), 1049–1057.

Chan, T. P., & Govindaraju, R. S. (2011). Pore-morphology-based simulations of drainage and wetting processes in porous media. Hydrology Research, 42(2–3), 128–149.

Cho, J., & Annable, M. D. (2005). Characterization of pore scale NAPL morphology in homogeneous sands as a function of grain size and NAPL dissolution. Chemosphere, 61(7), 899–908. https://doi.org/10.1016/j.chemosphere.2005.04.042

Costanza-Robinson, M. S., Harrold, K. H., & Lieb-Lappen, R. M. (2008). X-ray microtomography determination of air− water interfacial area− water saturation

relationships in sandy porous media. Environmental Science & Technology, 42(8), 2949–2956.

Costanza-Robinson, M. S., & Brusseau, M. L. (2002). Air-water interfacial areas in unsaturated soils: Evaluation of interfacial domains. Water Resources Research, 38(10).

Costanza, M. S., & Brusseau, M. L. (2000). Contaminant vapor adsorption at the gas−water interface in soils. Environmental Science & Technology, 34(1), 1–11.

Dahle, H. K., Celia, M. A., & Hassanizadeh, S. M. (2005). Bundle-of-tubes model for calculating dynamic effects in the capillary-pressure-saturation relationship. Transport in Porous Media, 58, 5–22. https://doi.org/10.1007/1-4020-3604-3_2

Dalla, E., Hilpert, M., & Miller, C. T. (2002). Computation of the interfacial area for two-fluid porous medium systems. Journal of Contaminant Hydrology, 56(1–2), 25–48.

Diamantopoulos, E, Durner, W., & Harter, T. (2016). Prediction of capillary air-liquid interfacial area vs. saturation function from relationship between capillary pressure and water saturation. Advances in Water Resources, 97, 219–223.

Diamantopoulos, Efstathios, & Durner, W. (2013). Physically-based model of soil hydraulic properties accounting for variable contact angle and its effect on hysteresis. Advances in Water Resources, 59, 169–180.

Diamantopoulos, Efstathios, & Durner, W. (2015). Closed-form model for hydraulic properties based on angular pores with lognormal size distribution. Vadose Zone Journal, 14(2).

Dobson, R., Schroth, M. H., Oostrom, M., & Zeyer, J. (2006). Determination of NAPL-water interfacial areas in well-characterized porous media. Environmental Science and Technology, 40(3), 815–822. https://doi.org/10.1021/es050037p

Dullien, F. A. L. (1992), Porous Media: Fluid Transport and Pore Structure, 2nd ed., 574 pp., Academic, San Diego, CA.

Dullien, F. A. L., Zarcone, C., Macdonald, I. F., Collins, A., & Bochard, R. D. E. (1989). The effects of surface roughness on the capillary pressure curves and the heights of capillary rise in glass bead packs. Journal of Colloid and Interface Science, 127(2), 362–372.

Ghanbarian, B., Hunt, A. G., & Daigle, H. (2016). Fluid flow in porous media with rough pore-solid interface. Water Resources Research, 52(3), 2045–2058.

Grant, G. P., & Gerhard, J. I. (2007). Simulating the dissolution of a complex dense nonaqueous phase liquid source zone: 1. Model to predict interfacial area. Water Resources Research, 43(12).

Gvirtzman, H., & Roberts, P. V. (1991). Pore scale spatial analysis of two immiscible fluids

in porous media. Water Resources Research, 27(6), 1165–1176.

Hassanizadeh, S. M., & Gray, W. G. (1993). Thermodynamic basis of capillary pressure in porous media. Water Resources Research, 29(10), 3389–3405.

Helland, J O, & Skjaeveland, S. M. (2007). Relationship between capillary pressure, saturation, and interfacial area from a model of mixed-wet triangular tubes. Water Resources Research, 43(12).

Helland, Johan O., & Skjœveland, S. M. (2006). Physically based capillary pressure correlation for mixed-wet reservoirs from a bundle-of-tubes model. SPE Journal, 11(2), 171–180. https://doi.org/10.2118/89428-PA

Israelachvili, J. N. (2011). Intermolecular and surface forces. Academic press.

Iwamatsu, M., & Horii, K. (1996). Capillary condensation and adhesion of two wetter surfaces. Journal of Colloid and Interface Science, 182(2), 400–406.

Joekar-Niasar, V., Prodanović, M., Wildenschild, D., & Hassanizadeh, S. M. (2010). Network model investigation of interfacial area, capillary pressure and saturation relationships in granular porous media. Water Resources Research, 46(6).

Kamusewitz, H., & Possart, W. (2003). Wetting and scanning force microscopy on rough polymer surfaces: Wenzel's roughness factor and the thermodynamic contact angle. Applied Physics A, 76(6), 899–902.

Kawanishi T., H. Y. R. P. V. B. M. J. (1998). Fluid-fluid interfacial area during two and three phase fluid displacement in porous media: A network model study. IAHS-AISH Publication, 250(250), 89–96.

Kibbey, T. C. G. (2013). The configuration of water on rough natural surfaces: Implications for understanding air-water interfacial area, film thickness, and imaging resolution. Water Resources Research, 49(8), 4765–4774.

Kibbey, T. C. G., & Chen, L. (2012). A pore network model study of the fluid-fluid interfacial areas measured by dynamic-interface tracer depletion and miscible displacement water phase advective tracer methods. Water Resources Research, 48(10).

Kim, H., Rao, P. S. C., & Annable, M. D. (1997). Determination of effective air-water interfacial area in partially saturated porous media using surfactant adsorption. Water Resources Research, 33(12), 2705–2711.

Kim, H., Rao, P. S. C., & Annable, M. D. (1999). Gaseous tracer technique for estimating air–water interfacial areas and interface mobility. Soil Science Society of America Journal, 63(6), 1554–1560.

Kim, T. W., Tokunaga, T. K., Shuman, D. B., Sutton, S. R., Newville, M., & Lanzirotti, A. (2012). Thickness measurements of nanoscale brine films on silica surfaces under geologic

CO2sequestration conditions using synchrotron X-ray fluorescence. Water Resources Research, 48(9).

Lampurlanés, J., & Cantero-Martínez, C. (2006). Hydraulic conductivity, residue cover and soil surface roughness under different tillage systems in semiarid conditions. Soil and Tillage Research, 85(1–2), 13–26.

Leão, T. P., & Tuller, M. (2014). Relating soil specific surface area, water film thickness, and water vapor adsorption. Water Resources Research, 30, 7873–7885. https://doi.org/10.1111/j.1752-1688.1969.tb04897.x

Leverett, M. (1941). Capillary behavior in porous solids. Transactions of the AIME, 142(01), 152–169.

Likos, W. J., & Jaafar, R. (2013). Pore-scale model for water retention and fluid partitioning of partially saturated granular soil. Journal of Geotechnical and Geoenvironmental Engineering, 139(5), 724–737.

Liu, G., Zhang, M., Ridgway, C., & Gane, P. (2014). Pore wall rugosity: the role of extended wetting contact line length during spontaneous liquid imbibition in porous media. Colloids and Surfaces A: Physicochemical and Engineering Aspects, 443, 286–295.

Lyu, Y., Brusseau, M. L., El Ouni, A., Araujo, J. B., & Su, X. (2017). The Gas-Absorption/Chemical-Reaction Method for Measuring Air-Water Interfacial Area in Natural Porous Media. Water Resources Research, 53(11), 9519–9527. https://doi.org/10.1002/2017WR021717

McClure, J. E., Berrill, M. A., Gray, W. G., & Miller, C. T. (2016). Influence of phase connectivity on the relationship among capillary pressure, fluid saturation, and interfacial area in two-fluid-phase porous medium systems. Physical Review E, 94(3), 33102.

McDonald, K., Carroll, K. C., & Brusseau, M. L. (2016). Comparison of fluid-fluid interfacial areas measured with X-ray microtomography and interfacial partitioning tracer tests for the same samples. Water Resources Research, 52(7), 5393–5399.

Narter, M., & Brusseau, M. L. (2010). Comparison of interfacial partitioning tracer test and high-resolution microtomography measurements of fluid-fluid interfacial areas for an ideal porous medium. Water Resources Research, 46(8), 1–7. https://doi.org/10.1029/2009WR008375

Oliver, J. P., Huh, C., & Mason, S. G. (1980). An experimental study of some effects of solid surface roughness on wetting. Colloids and Surfaces, 1(1), 79–104.

Oostrom, M., White, M. D., & Brusseau, M. L. (2001). Theoretical estimation of free and entrapped nonwetting–wetting fluid interfacial areas in porous media. Advances in Water Resources, 24(8), 887–898.

Or, D., & Tuller, M. (1999). Liquid retention and interfacial area in variably saturated porous media: Upscaling from single-pore to sample-scale model. Water Resources Research, 35(12), 3591–3605.

Or, D., & Tuller, M. (2000). Flow in unsaturated fractured porous media: Hydraulic conductivity of rough surfaces. Water Resources Research, 36(5), 1165–1177.

Peng, S., & Brusseau, M. L. (2005). Impact of soil texture on air-water interfacial areas in unsaturated sandy porous media. Water Resources Research, 41(3).

Peng, S., & Brusseau, M. L. (2012). Air-Water Interfacial Area and Capillary Pressure: Porous-Medium Texture Effects and an Empirical Function. Journal of Hydrologic Engineering, 17(7), 829–832.

Philip, J. R. (1978). Adsorption and capillary condensation on rough surfaces. Journal of Physical Chemistry, 82(12), 1379–1385. https://doi.org/10.1021/j100501a012

Porter, M. L., Schaap, M. G., & Wildenschild, D. (2009). Lattice-Boltzmann simulations of the capillary pressure–saturation–interfacial area relationship for porous media. Advances in Water Resources, 32(11), 1632–1640.

Porter, M. L., Wildenschild, D., Grant, G., & Gerhard, J. I. (2010). Measurement and prediction of the relationship between capillary pressure, saturation, and interfacial area in a NAPL-water-glass bead system. Water Resources Research, 46(8), 1–10. https://doi.org/10.1029/2009WR007786

Pyrak-Nolte, L. J., Nolte, D. D., Chen, D., & Giordano, N. J. (2008). Relating capillary pressure to interfacial areas. Water Resources Research, 44(6).

Reeves, P. C., & Celia, M. A. (1996). A functional relationship between capillary pressure, saturation, and interfacial area as revealed by a pore-scale network model. Water Resources Research, 32(8), 2345–2358.

Resurreccion, A. C., Moldrup, P., Tuller, M., Ferré, T. P. A., Kawamoto, K., Komatsu, T., & De Jonge, L. W. (2011). Relationship between specific surface area and the dry end of the water retention curve for soils with varying clay and organic carbon contents. Water Resources Research, 47(6).

Santamaría, J., Brusseau, M. L., Araujo, J., Orosz-Coghlan, P., Blanford, W. J., & Gerba, C. P. (2012). Transport and retention of Cryptosporidium parvum oocysts in sandy soils. Journal of Environmental Quality, 41(4), 1246–1252.

Saripalli, K. P., Kim, H., Rao, P. S. C., & Annable, M. D. (1997). Measurement of specific fluid-fluid interfacial areas of immiscible fluids in poreus media. Environmental Science and Technology, 31(3), 932–936. https://doi.org/10.1021/es960652g

Schaefer, C.E., DiCarlo, D.A., Blunt, M.J., 2000. Experimental measurement of air–water

interfacial area during gravity drainage and secondary imbibition in porous media. Water Resour. Res. 36, 885–890.

Schnaar, G., & Brusseau, M. L. (2006). Characterizing Pore-Scale Configuration of Organic Immiscible Liquid in Multiphase Systems With Synchrotron X-Ray Microtomography. Vadose Zone Journal, 5(2), 641. https://doi.org/10.2136/vzj2005.0063

Schroth, M. H., Oostrom, M., Dobson, R., & Zeyer, J. (2008). Thermodynamic Model for Fluid–Fluid Interfacial Areas in Porous Media for Arbitrary Drainage–Imbibition Sequences. Vadose Zone Journal, 7(3), 966. https://doi.org/10.2136/vzj2007.0185

Shahraeeni, E., & Or, D. (2012). Pore-scale evaporation-condensation dynamics resolved by synchrotron x-ray tomography. Physical Review E - Statistical, Nonlinear, and Soft Matter Physics, 85(1), 1–8. https://doi.org/10.1103/PhysRevE.85.016317

Skopp, J. (1985). Oxygen Uptake and Transport in Soils: Analysis of the Air-water Interfacial Area. Soil Science Society of America Journal, 49(6), 1327–1331.

Song, X., & Boily, J. F. (2013). Water vapor adsorption on goethite. Environmental Science and Technology, 47(13), 7171–7177. https://doi.org/10.1021/es400147a

Thompson, M. E., & Brown, S. R. (1991). The effect of anisotropic surface roughness on flow and transport in fractures. Journal of Geophysical Research: Solid Earth, 96(B13), 21923–21932.

Tokunaga, T. K. (2011). Physicochemical controls on adsorbed water film thickness in unsaturated geological media. Water Resources Research, 47(8).

Tokunaga, T. K., & Wan, J. (1997). Water film flow along fracture surfaces of porous rock. Water Resources Research, 33(6), 1287–1295.

Tokunaga, T. K., Olson, K. R., & Wan, J. (2003). Moisture characteristics of Hanford gravels. Vadose Zone Journal, 2(3), 322–329.

Tuller, M., & Or, D. (2001). Hydraulic conductivity of variably saturated porous media: Film and corner flow in angular pore space. Water Resources Research, 37(5), 1257–1276.

Tuller, M., Or, D., & Dudley, L. M. (1999). Adsorption and capillary condensation in porous media: Liquid retention and interfacial configurations in angular pores. Water Resources Research, 35(7), 1949–1964.

Watanabe, K., & Flury, M. (2008). Capillary bundle model of hydraulic conductivity for frozen soil. Water Resources Research, 44(12), 1–9. https://doi.org/10.1029/2008WR007012

Wenzel, R. N. (1936). Resistance of solid surfaces to wetting by water. Industrial & Engineering Chemistry, 28(8), 988–994.

Zheng, W., Yu, X., & Jin, Y. (2015). Considering surface roughness effects in a triangular pore space model for unsaturated hydraulic conductivity. Vadose Zone Journal, 14(7).

Zhong, H., El Ouni, A., Lin, D., Wang, B., & Brusseau, M. L. (2016). The two-phase flow IPTT method for measurement of nonwetting-wetting liquid interfacial areas at higher nonwetting saturations in natural porous media. Water Resources Research, 52(7), 5506–5515. https://doi.org/10.1002/2016WR018783.

Appendix B

Characterization of the Micro-scale Surface Roughness Effect on Immiscible Fluids and Interfacial Areas in Porous Media Using the Measurements of Interfacial Partitioning Tracer Tests

Hao Jiang[1], Bo Guo[2] and Mark L. Brusseau[2,3,*]

[1]Department of Chemical and Environmental Engineering
University of Arizona
1133 E James E Rogers Way
Tucson, Arizona 85721, USA

[2]Department of Hydrology and Atmospheric Sciences
University of Arizona
1133 E James E Rogers Way
Tucson, Arizona 85721, USA

[3]Department of Environmental Science
University of Arizona
429 Shantz Bldg.
Tucson, AZ 85721, USA

Submitted to:

Science of the Total Environment

January 2020

*Corresponding author

Abstract

This study presents a model-based methodology to characterize the surface roughness effect on immiscible fluids in porous media using the measurements obtained with the gas-phase interfacial partitioning tracer test (IPTT). The characterization approach captures how adsorbed wetting film configuration on grain surfaces influences fluid-fluid interfaces in unsaturated porous media. The method established a novel representation of surface and interface roughness that delineated the micro-scale fractal nature of grain surfaces and the fluid-surface interactions at these scales. The method was tested using reported experimental data for several soils. The results showed that the methodology was effective for various natural media. Comparisons between characterized parameters of different media revealed that micro-scale surface roughness was only partially correlated to soil texture properties. Images of the test media obtained with scanning electron microscopy (SEM) illustrated the complexity of micro-scale surface roughness, and its variability among different media. Tests with an organic liquid–water system validated the generalness of surface roughness properties generated by the model. The proposed methodology is anticipated to provide a means to characterize and quantify the effects of surface roughness on fluid-solid interaction and fluid-fluid interfacial area, which are critical to various environmental disciplines.

Key points

- A model-based methodology to characterize the surface roughness effect on wetting film configuration and interfacial area in porous media is presented.

- The method captures the complicated nature of grain surface roughness and its effect on immiscible fluids with explicit parameters.

- The method shows good performance for the interfacial areas in both air-water and NAPL-water systems.

Key words

Interfacial area; Surface roughness effect; Wetting film; Surface adsorption and capillarity.

1. Introduction

In many environmental processes, the interactions between immiscible fluids and rough solid surfaces play a significant role in the determination of various soil and hydraulic properties. It has been shown that surface roughness has significant impacts on the wettability of solid surfaces (Wenzel, 1936; Cassie & Baxter, 1944; Hirasaki, 1991; Oliver et al., 1980), which is closely associated with the configuration of fluids in soil. It has also been demonstrated that surface roughness can influence the resistance of flow over fractured surfaces in unsaturated media (Brown, 1987; Lampurlanés & Cantero-Martínez, 2006; Or & Tuller, 2000; Thompson & Brown, 1991; Tokunaga & Wan, 1997), which is a critical factor for the hydraulic conductivity of fluid flow. Wetting-fluid configuration on rough surfaces can also affect the shape of wetting films, which can affect both film interfacial area and film thickness (Kibbey, 2013; Kim et al., 2012; Tokunaga, 2011; Zheng et al., 2015). In natural soil systems, the solid phases can typically be treated as constant for most flow conditions. Thus, it is reasonable to define the solid surface roughness as an inherent property of soil, and establish quantitative relationships between surface roughness and other fluid and flow properties, which can be extended to simulate realistic environmental systems.

The complex nature of surface roughness poses challenges to develop a universal fluid-surface function for the great variety of natural porous media. Typically, surface roughness can be defined from three different viewpoints (Ghanbarian et al., 2016; Wenzel, 1936), each of which represents a specific principle for the interactions with fluids. The three approaches are conceptualized in the left column of Figure 1.

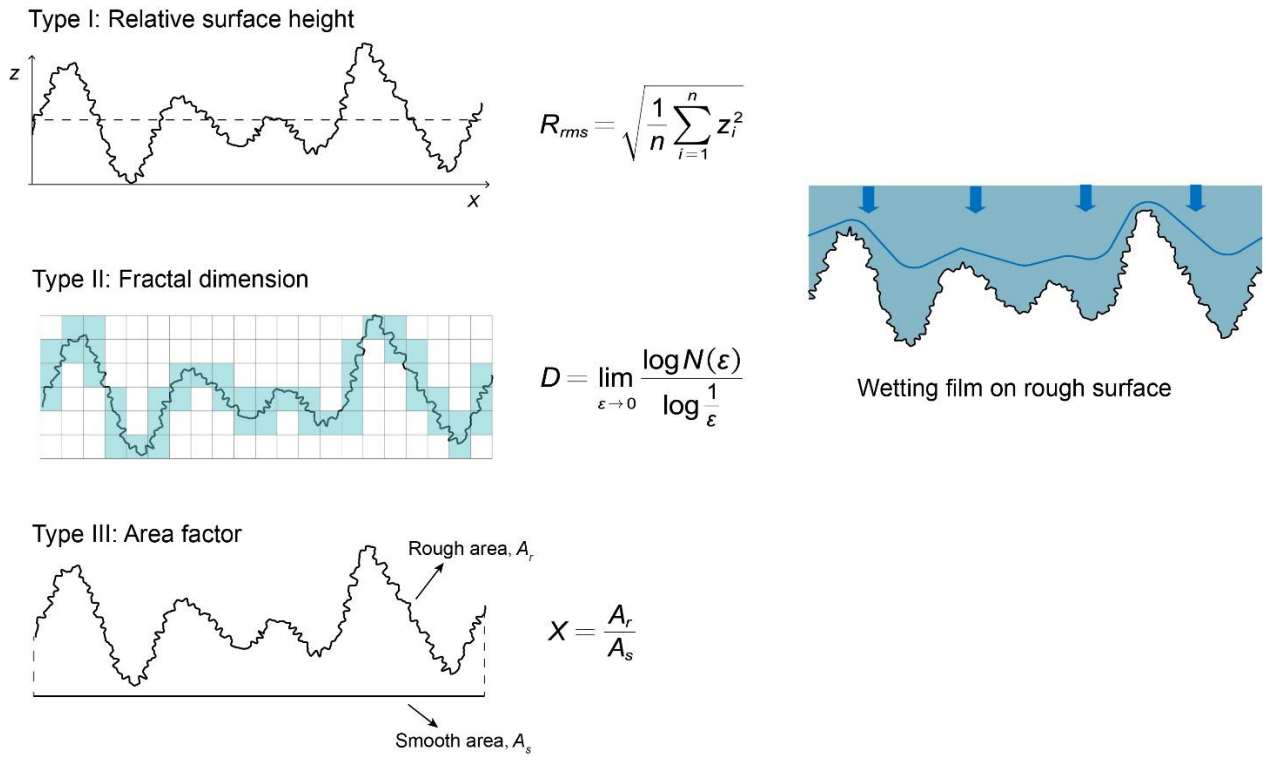

Figure 19. Types of representations of surface roughness. (i) Relative surface height, calculated as the average elevation (usually root-mean-square, R_{rms}) to a reference coordinate axle. (ii) Fractal dimension (D), shown as the box-counting dimension, which is calculated by covering the fractal curve with box grids of equal side length (ε) and counting the number of boxes required (N). (iii) Area factor (X), calculated as the ratio of the cumulative rough area (A_r) over a reference smooth area (A_s). Configuration of a wetting film on rough surface is plotted in the right column.

The traditional definition of surface roughness is based on the average value of measured vertical coordinates compared to a reference level (relative surface height), e.g., arithmetic roughness (R_a) or root-mean-square roughness (R_{rms}). However, the relative surface height definition was found insufficient in practice due to the lack of fractal topology (Brown, 1987, 1989; Ghanbarian et al., 2016). The second definition of surface roughness originates from the basic concept of fractal geometry (Mandelbrot, 1983), in which either the pore surfaces (2D) or the entire porous medium (3D) are modified with corrections of fractal dimension, resulting in higher dimensions for surfaces (Brown, 1987; Ghanbarian et al., 2016) or lower dimensions for entire media (Crawford, 1994; Giménez

et al., 1997; Toledo et al., 1990). The third definition was proposed by Wenzel (1936), in which surface roughness was defined as an area factor, e.g., the ratio of "actual surface area" over "geometric surface area". Some studies have used this definition to modify flow equations (e.g., Philip, 1978; Liu et al., 2014; Zheng et al., 2015; Jiang et al., 2019).

Another challenge for an explicit fluid-surface function is the method of characterization of surface roughness, especially for the inner pore surfaces of natural porous media. Most reports of grain surface roughness based on relative surface height are obtained by direct measurements, such as laser profilometry and atomic force microscopy (AFM) (e.g., Tokunaga et al., 2003; Kim et al., 2012), or photogrammetric reconstruction on images from scanning electron microscopy (SEM) (e.g., Kibbey, 2013). However, these methods have very small fields of view (e.g., less than 100 μm in one dimension in AFM), which brings about uncertainties at larger scales. An alternative approach is to characterize surface roughness from soil hydraulic measurements, thereby capturing larger-scale effects. For instance, fractal dimension definitions (Ghanbarian et al., 2016; Pachepsky et al., 1995; Perfect, 1999) and area factor definitions (Or & Tuller, 2000; Zheng et al., 2015) of surface roughness have been reported in modeling works that were extracted from measurements of soil water characteristic (SWC) curves or unsaturated hydraulic conductivity. A limitation to this approach is that these SWC and unsaturated hydraulic conductivity data may not be highly sensitive to roughness and its influence on wetting-fluid configuration.

Measurements from gas-phase interfacial partitioning tracer tests (IPTT) have shown that total (film+meniscus) air-water interfacial areas (A_{nw}) in natural porous media increase exponentially at lower wetting-fluid saturations (Kim et al., 1999; Costanza-Robinson & Brusseau, 2002; Brusseau et al., 2006). Comparison between the measurements from gas-phase IPTT, aqueous-phase IPTT and X-ray microtomography revealed that the exponential increase is probably due to the significant involvement of surface roughness to film-associated interfaces at lower saturations (Brusseau et al., 2007). This is supported by the results of pore-scale modeling conducted using models that either implicitly (Or &

Tuller, 1999) or explicitly (Jiang et al., 2019) account for surface roughness and its impacts on interfacial area. The experimental and modeling results demonstrate that the $A_{nw} - S_w$ function is highly sensitive to surface roughness, particularly at lower water saturations. Based on this behavior, Jiang et al (2019) proposed using measured $A_{nw} - S_w$ functions as a "wetting-film characteristic curve" to provide robust characterization of surface roughness and its interaction with wetting-fluid films. With this approach, the gas-phase IPTT method can be used to conduct low-saturation measurements of total A_{nw} for a specific soil, and these data can be used to characterize fluid-surface interactions specific to that soil. It is anticipated that this approach would have multiple advantages, including greater sensitivity compared to other macroscale approaches, the ability to support both fractal-dimension and area-factor definitions, and provide characterization of surface roughness across a broader range of scales.

In the present study, we propose a general approach to characterize fluid-surface interactions and the associated model parameters from gas-phase IPTT measurements. The basic principles of characterization are universal, which can be realized via most of the current pore-scale models (i.e., bundle-of-cylindrical-capillaries, pore-network, pore-morphology, Lattice-Boltzmann). Here, we use a triangular-pore-space bundle-of-cylindrical-capillaries (BCC) model to conduct the characterization, which has been described in Jiang et al. (2019). We use the published IPTT measurements of four soil samples, and generate the characteristic parameters for each sample. We also test the validity of characterization approach under some varied conditions. In addition, we have conducted SEM imaging at different magnifications for each soil sample to visualize and verify the representation of surface roughness parameters. The present approach can be used to quantify fluid-solid and fluid-fluid interfacial interactions for a wide range of environmental problems .

2. Model

2.1 General Theory

The present modeling approach is based on the previous study of Jiang et al. (2019). The essential principle in the approach is the conceptual representation of wetting films on the grain surfaces of porous media. Experimental and simulation evidence has indicated that wetting films on grain surfaces are held by a combination of surface adsorption (DLVO) and capillary forces (Kibbey, 2013; Kim et al., 2012; Tokunaga, 2011). The dominant force depends on matric potentials, and thus wetting phase saturations, as well as the properties of the surface. When surface adsorption completely dominates, wetting films are only a few molecules thick, in which the film area can be treated identical to the solid surface area obtained from gas adsorption experiments (e.g., nitrogen-BET). When capillarity dominates, film thickness increases such that the film may partially or fully cover the solid surface roughness. In the extreme case of full coverage, the wetting film can be regarded as smooth. Jiang et al. (2019) presented the concept of minimum and maximum theoretical $A_{nw} - S_w$ functions, with the actual behavior observed dependent upon a number of factors. This concept is illustrated in Figure 2a by a theoretical "surface-fluid triangle", which illustrates the function of surface adsorption and capillarity.

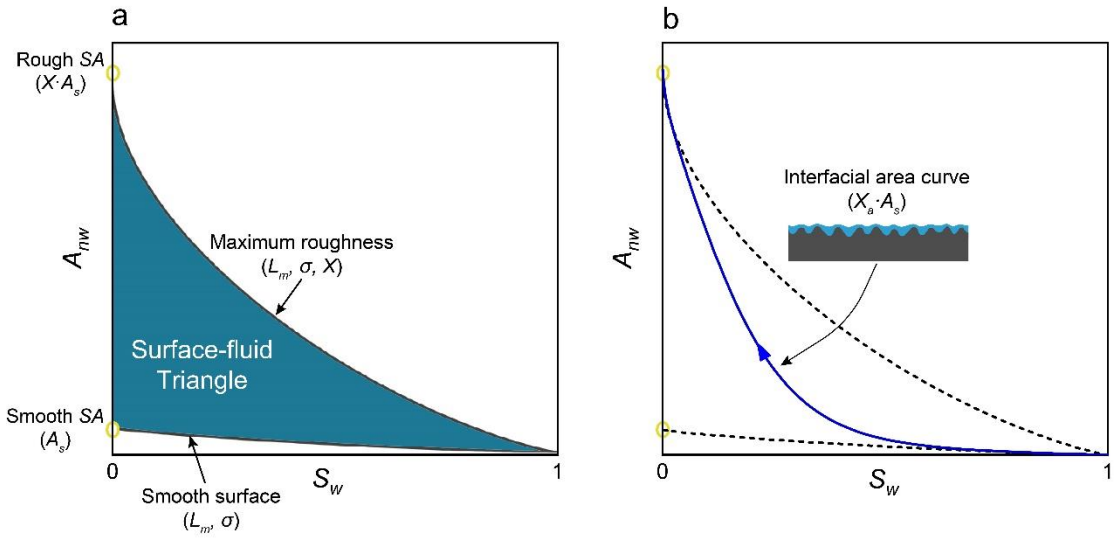

Figure 20. Illustration of (a) the "surface-fluid triangle" in an $A_{nw} - S_w$ plot, and (b) the location of an actual $A_{nw} - S_w$ curve. Model parameters corresponding to each curve are marked.

The surface-fluid triangle is anchored by a zero interfacial area at $S_w = 1$ and two points at $S_w = 0$: a "smooth" specific solid surface area (A_s) and a "rough" specific solid surface area (A_r), which follows the assumption that the maximum interfacial area is equal to the solid surface area (Or & Tuller, 1999; Peng & Brusseau, 2005; Jiang et al., 2019). The lower and upper curves correspond to two imaginary cases of "smooth-surface" and "maximum-roughness", respectively. For the smooth-surface curve, it is assumed that no surface roughness exists in grain surfaces, or surface roughness is completely masked by capillary fluids at all saturations. For the maximum-roughness curve, it is hypothesized that only surface adsorption participates in the configuration of wetting film, so that the shape of wetting film is always identical to the rough solid surface covered by the wetting film. The two limits of surface-fluid triangle are determined by the inherent properties of porous media. The smooth-surface curve is controlled simply by the pore structure and pore size distribution of a soil. Conversely, the maximum-roughness curve indicates the highest degree to which surface roughness can affect wetting film area. Such degree can be derived from the two anchor points in the A_{nw} axis. For a rough porous medium, the surface roughness factor, X, is defined by the ratio of its rough specific surface area, A_r, over the smooth specific surface area, A_s, such that:

$$X = A_r/A_s \quad (6)$$

Typically, A_r can be obtained from the nitrogen-BET measurement of specific solid surface area. There are various methods to determine A_s, for instance, using a smooth-sphere assumption for grain particles and calculating from the mean particle diameter; using pre-obtained pore size distribution from other measurements such as SWC; or using the estimation from X-ray microtomography, where surface roughness is typically negligible due to the resolution limit (Brusseau et al., 2007). In our simulations, the use of the BCC

approach can result in some degree of error in the representation of smooth-surface area for some porous media (Jiang et al., 2019).

Results of IPTT, especially the gas-phase experiments at lower water saturations (< 0.4), have shown that actual A_{nw} curves in full saturations reside within the surface-fluid triangle as in Figure 2b. The insert in Figure 2b illustrates the possible shape of wetting film in an actual drainage process. When capillary is dominant at higher saturations, the film thickness is sufficiently higher than the magnitude of surface roughness, which in effect masks the impact of surface roughness. In the plot, the actual A_{nw} curve will be seemingly attached to the smooth-surface curve. As surface adsorption becomes significant during drainage, surface roughness, including the fractal iterations to much smaller scales (1~10 nm), considerably increase the magnitude of film interfacial area, resulting in the exponential increase in Figure 2b. Finally, the A_{nw} curve ascends towards the specific solid surface area, and merges with the maximum-roughness curve. For a specific porous medium, the degree to which surface roughness is masked can vary depending on its features of fractal-scale roughness, which should be expressed via fractal dimension or area factor. Thus, it is reasonable to introduce an interfacial area factor X_a, which is always lower than the solid surface roughness factor X, such that:

$$X_a = A_{nw}/A_s \quad (7)$$

It is worthwhile to note that X in equation (1) only depends on the properties of soil, but X_a in equation (2) is a function of saturations, and ultimately, matric potentials in drainage. Therefore, for a universal approach to characterize surface roughness from sample-scale measurements of soils, the methodology requires two steps: (i) determine the value of X; (ii) determine X_a as a function of saturation or matric potential.

2.2 Characterization Model

Following the criteria in section 2.1, we select the bundle of cylindrical capillaries (BCC) method to establish the characterization model. The major advantage of BCC over

other modeling approaches (e.g., pore-network) is the apparent demonstration of pore size distribution for a specific porous medium, which is convenient to introduce the surface roughness representation of X and X_a in accordance with experimental data. In the present BCC model, a porous medium is approximated as a bundle of equilateral triangular pores, whose side length, L, follows a lognormal distribution, $f(L)$:

$$f(L) = \frac{1}{L\sigma\sqrt{2\pi}} \exp\left(-\frac{[\ln(L/L_m)]}{2\sigma^2}\right) \quad (8)$$

The two parameters L_m and σ are the mean side length and logarithm standard deviation for lognormal distribution, respectively. For an unsaturated smooth porous medium, both specific solid surface area (A_s) and interfacial area (A_{nw}) are only controlled by the pore size distribution parameters L_m and σ (see Figure 2a). For a rough porous medium, first, it is assumed that every pore has a uniform surface roughness factor, X, defined by equation (1); then, under a specific matric potential, μ, there is the interfacial area factor, X_a, exerted on each pore surfaces in the form of wetting film (Figure 1b). The mathematical equation of X_a is assumed to follow a logistic function in this study, which is given by:

$$X_a = \frac{X + e^{k(h_{ad} - h_m)}}{1 + e^{k(h_{ad} - h_m)}} \quad (9)$$

where the parameters k and h_m correspond to the change of wetting film in drainage under the impact of micro-scale fractal roughness. Parameter k controls the growth rate of film area in drainage, and h_m (in the unit of length) indicates the thickness of a critical sub-layer of roughness, which triggers the exponential increase in the $A_{nw} - S_w$ curve. The argument variable h_{ad} in equation (4) is a function of matric potential μ (see Appendix for the equation). With the constraints in equation (4), X_a is only controlled by one variable, μ, and is always limited in the range between 1 and X.

The characterization of surface roughness has been parameterized into five explicit parameters: L_m, σ, X, k, and h_m. Each of them can be determined from experimental data

sets, e.g., SWC ($P_c - S_w$) and IPTT ($A_{nw} - S_w$) measurements. In practice, data of SWC are used to determine the pore size distribution parameters L_m and σ, and subsequently, the overall roughness factor X can be calculated as the ratio of the smooth surface area obtained from these parameters and the measured nitrogen-BET specific surface area A_r. Upon obtaining L_m, σ, and X, the remaining parameters k and h_m can be obtained by fitting the model to the $A_{nw} - S_w$ data set. Determining the values of k and h_m for a specific porous medium is the critical step in the characterization procedure.

The detailed procedure of optimization requires a classification of the wetting-fluid distribution in pores, which can range from fully-filled to partially-drained to fully-drained pores. In partially-drained pores, wetting fluid is distributed along the pore side walls, and form different configurations as film fluids or meniscus fluids, corresponding to film and meniscus interfacial area. Under a given drainage potential, there is a critical size of pore where the nonwetting phase begin to invade into a filled pore (onset of drainage). This critical pore size, L_1, corresponds to a geometrical constraint given by Tuller et al. (1999):

$$L_1 = \frac{\gamma}{\rho\mu} C_3 \quad (10)$$

where γ and ρ are the surface tension of wetting liquid, respectively, and C_3 is a constant regarding to triangular pore geometry (see Appendix). Pores larger than that size are all partially-filled, with the same meniscus radius, r, controlled by the Young-Laplace law (the wetting phase is assumed to be completely wetting to the solid surface):

$$r = \frac{\gamma}{\rho\mu} \quad (11)$$

Knowing the relationship between matric potentials and critical pore sizes, the equations for capillary pressure (matric potential), saturation, and interfacial area can all be derived from pore geometry. Typical equations for both S_w and A_{nw} are given with matric potentials as the argument variable. To conduct the surface roughness characterization, it is assumed that the three variables coalesce into an integrated $P_c - S_w - A_{nw}$ relationship

(Hassanizadeh & Gray, 1993), so as to make it convenient to implement the model optimization on $A_{nw} - S_w$ data set. The equations for S_w and A_{nw} with the terms of all types of fluid configuration (filled-pore fluid, film fluid, and capillary-meniscus fluid) are given as:

$$S_w = S_{wd}(\mu) + S_{wf}(\mu) + S_{wc}(\mu) \quad (12)$$

$$S_{wd}(\mu) = \int_{L_{\min}}^{L_1(\mu)} f(L)\,dL \quad (13)$$

$$S_{wf}(\mu) = \int_{L_1(\mu)}^{L_{\max}} \frac{3h(\mu)\left[L - 2r(\mu)\cot(\pi/6)\right]}{A_3 L^2} f(L)\,dL \quad (14)$$

$$S_{wc}(\mu) = \int_{L_1(\mu)}^{L_{\max}} \frac{3F_3 r^2(\mu)}{A_3 L^2} f(L)\,dL \quad (15)$$

$$A_{nw} = A_{nwf}(\mu) + A_{nwc}(\mu) \quad (16)$$

$$A_{nwf}(\mu) = \int_{L_1(\mu)}^{L_{\max}} \frac{3X_a\left[L - 2r(\mu)\cot(\pi/6)\right]}{A_3 L^2} f(L)\,dL \quad (17)$$

$$A_{nwc}(\mu) = \int_{L_1(\mu)}^{L_{\max}} \frac{3\pi r(\mu)}{2A_3 L^2} f(L)\,dL \quad (18)$$

Equations (7~10) and equations (11~13) indicate that total saturation is the sum of filled-pore fluid (S_{wd}), film fluid (S_{wf}), and capillary-meniscus fluid (S_{wc}), while total interfacial area is only determined by film (A_{nwf}) and capillary-meniscus (A_{nwc}) fluid in partially-filled pores. Definitions of unmentioned parameters are listed in the Appendix. The magnitudes of these components have been investigated in previous modeling studies (Or & Tuller, 1999; Zheng et al., 2015; Jinag et al., 2019), amongst which filled-pore fluid is dominant in saturation, and film fluid is dominant in interfacial area. It is then logical to minimize focus on the uncertainties in the less significant components during the characterization process, e.g., film fluid in fitting $P_c - S_w$ curves, and meniscus interface in fitting $A_{nw} - S_w$ curves. It is also noted that the maximum A_{nw} in equation (11) as $\mu \to \infty$ is equal to the rough specific surface area A_r, which represents the assumptions of Figure 2b.

3. Materials

Peng & Brusseau (2005, 2012) measured the air-water interfacial areas for various types of porous media via gas-phase IPTT. In addition, they reported the data of specific solid surface areas and soil water characteristic curves for four media: Accusand, Granusil, Vinton, and Hayhook. Among the four porous media, Accusand and Granusil are well-sorted natural sands; Vinton is a sandy soil; Hayhook is a coarse loamy soil. The four selected porous media cover a broad range of natural sands and soils, which are useful for the test of surface characterization methods on varying natural media. Basic soil texture properties for the studied porous media are summarized in Table 1.

Typical gas-phase IPTT measurements are unable to be implemented at higher water saturations. In contrast, aqueous-phase IPTT is the alternative for porous media with $S_w >$ 0.5. Nevertheless, Peng & Brusseau (2005) developed an empirical relationship from the low-S_w data of interfacial area, and showed that low-S_w data were sufficient to predict the full-S_w interfacial area profile. In the present study, reported gas-phase IPTT measurements from Peng & Brusseau (2005, 2012) for the four selected porous media are used. For the consideration of completeness, available A_{nw} data at higher saturations obtained via aqueous-phase IPTT are also collected from Brusseau et al. (2006, 2015) for two of the selected media: Accusand and Vinton. In addition, an IPTT measurement of a PCE-water system on Accusand from Zhong et al. (2016) is also chosen to further verify the modeling methodology in generalized fluid systems. Another sandy medium with interfacial area measurements by Kim et al. (1997, 1999) is also listed in Table 1 for comparisons in the following sections.

Table 5. Physical properties of the selected porous media.

Medium	Texture	Mean diameter d_m (mm)	Porosity n	Bulk density (g/cm^3)	Specific solid surface area (cm^{-1})
Kim et al.	Sand	0.250	0.36	1.72	2000
Accusand	Sand	0.350	0.42	1.65	2800
Granusil	Sand	0.172	0.43	1.54	6622
Vinton	Sandy soil	0.234	0.46	1.46	51684
Hayhook	Soil	0.260	0.36	1.64	88000

4. Results and Discussion

4.1 Parameterization of Surface Roughness Effect

Experimental evidence has shown that wetting films on natural grain surfaces are sensitive to scales. Surface adsorption can only support thin films at the magnitude of 1~10 nm (Resurreccion et al., 2011; Tokunaga, 2011), while capillary forces tend to be enhanced on rougher surfaces, resulting in thicker films at the magnitude of 0.1~1 μm (Kim et al., 2012; Tokunaga, 2011; Tokunaga et al., 2003). Among the three types of surface roughness representations in Figure 1, the relative surface height (Type I) is limited by its primary scale for the selected range of coordinates. The fractal dimension (Type II) has been used to simulate soil hydraulic properties such as hydraulic conductivity and relative permeability (Ghanbarian et al., 2016; Thompson & Brown, 1991). However, fractal dimension is appropriate for multi-dimensional problems with a constant D value (e.g., the perimeter and cross-section area are related by fractal dimension in tube flow), but is inconvenient for situations where D is changing, which occur in the change of wetting film controlled by matric potentials. Conversely, the area factor (Type III) approach used in this study, especially the use of interfacial area factor X_a, defines a good cross-scale methodology to parameterize the scale-sensitive interaction between fluids and solid

surfaces. At the lowest matric potentials, the wetting-film interfaces will tend to be smooth, which is the lowest D. As surface adsorption dominates at higher matric potentials, the films become sufficiently thin such that their surface topology mimics the finest structures of the solid surface, representing the highest fractal dimension, which is also the D of rough solid surfaces. Therefore, the interfacial area factor X_a contains information of the fractal-scale properties of wetting films. In addition, the measuring scales for area factor is controlled by experiment-based variables, such as nitrogen-BET measured solid A_r, matric potentials, wetting-fluid saturations, and interfacial areas, which improves the accuracy of fractal representation.

Thus, it is elucidated that the "surface-fluid triangle" defined in Figure 2 delineates the free fractal space of wetting film interfacial area, wherein the upper (maximum-roughness) and lower (smooth-surface) curves represent the maximum and minimum fractal dimensions of the film interface, respectively. Meanwhile, the two limiting conditions determine the range for X_a, within $X_a = 1$ (smooth) and $X_a = X$ (roughness factor of solid phase). As long as the interfacial area factor $X_a(\mu)$ is measured from IPTT experiments, the surface-fluid interaction in fractal space can be quantified and parameterized.

The logistic equation (4) provides a simple approach for quantifying roughness characteristic, with only two parameters: k and h_m. The effects of k and h_m are illustrated in Figure 3. In general, both parameters define to which degree the participating capillary forces mask the solid surface roughness beneath a wetting film, as is shown by the phenomena that some portions of the $A_{nw} - S_w$ curves are coincident with the smooth-surface curves in both plots. Inspection of Figure 3 indicates that either increasing k or decreasing h_m can enhance the degree of masking. In addition, the trends of changes are different for k and h_m: in an $A_{nw} - S_w$ plot, k controls more of the horizontal region of A_{nw} curves (the higher saturation region), while h_m has a stronger influence on the vertical region (lower saturations).

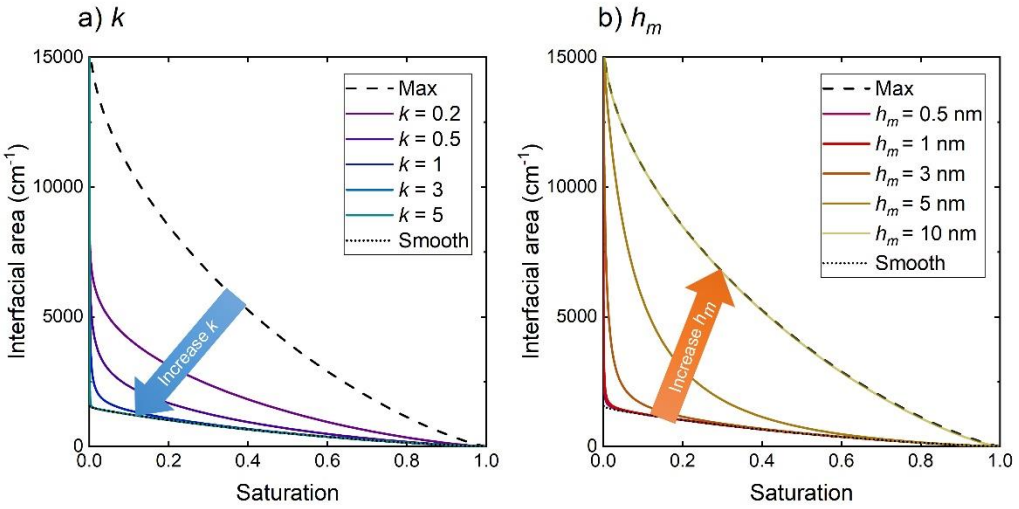

Figure 21. Effects of changing parameter (a) k (b) h_m in the space of surface-fluid triangle. The default parameter. The default values of parameters are $X = 50$, $L_m = 90$ μm, $\sigma = 0.5$, $\mu_d = $ 1 J/kg, $k = 1$, and $h_m = 2$ nm.

Based on the mathematical features of the logistic function and fractal geometry, we are able to develop the physical representations for parameters k and h_m. First, as a variable with the dimension of length, h_m corresponds to a critical matric potential, which is normalized as "critical adsorptive thickness" in the logistic function, such that wetting film thickness falls into the magnitude of the critical manifestation of fractal roughness. It is noted that the actual wetting film thickness at this stage is not equal to h_m, as the involvement of capillary forces in wetting film is still significant. The equation to calculate this film thickness is given in the Appendix. Larger values of h_m cause the exponential stage of $A_{nw} - S_w$ curves to start earlier, i.e. at higher saturations. The exponential parameter k determines the growth rate of the logistic curve, which is, from another perspective, a representation of the complexity of fractal structures. Surfaces with smaller k values have smaller degrees of surface-roughness masking for the $A_{nw} - S_w$ curves. Thus, the curves exhibit a more uniform rate of increase as saturation decreases. This indicates that surfaces with smaller k values comprise greater number of fractal iterations between smooth surface and maximum roughness, or between the varying ranges of fractal dimensions.

4.2 Characterization Results

Results of the fitted curves generated by the characterization model are illustrated in Figure 4 in comparison with the original measured data of $P_c - S_w$ and total $A_{nw} - S_w$. All simulated curves are generated by the optimization toolbox in MATLAB. It is shown that the model produces very good fits of the measured data. The solid roughness factor X is determined from the solid specific surface area measured via nitrogen-BET, the lognormal pore size distribution parameters L_m and σ are derived from the $P_c - S_w$ data sets, and the logistic parameters k and h_m are derived from the total $A_{nw} - S_w$ data sets. Overall, the good matches of the measured data for all four media shows that the proposed parameters and mathematical assumptions are sufficient to address the characteristics of surface roughness on natural granular media. One possible source of uncertainty is the values of lognormal standard deviation, which is affected by some inconsistencies on the low saturation data of $P_c - S_w$ curves. However, as discussed by Jiang et al. (2019), the standard deviation has very little impact on the determination of interfacial area parameters.

Table 2. Parameters of soil texture, pore size distribution, and surface roughness properties for the selected porous media.

	Soil texture		Solid surface roughness		Pore size distribution		Micro-scale surface-fluid		
Parameter	d_{50} (μm)	$U = d_{60}/d_{10}$	A_r (cm^{-1})	X	L_m (μm)	σ	k (nm^{-1})	h_m (nm)	h_c (nm)
Kim et al.	250	N/A	2000	5.0	171.0	0.164	2.1	6.3	4.0
Accusand	350	1.16	2800	8.7	212.7	0.303	3	9.7	8.5
Granusil	172	1.77	6622	11.3	116.4	0.251	1.5	7.5	9.2
Vinton	234	2.4	51684	58	93.6	0.685	1.8	5.2	26.3
Hayhook	260	16	88000	40.6	58.0	1.119	0.75	3.3	11.9

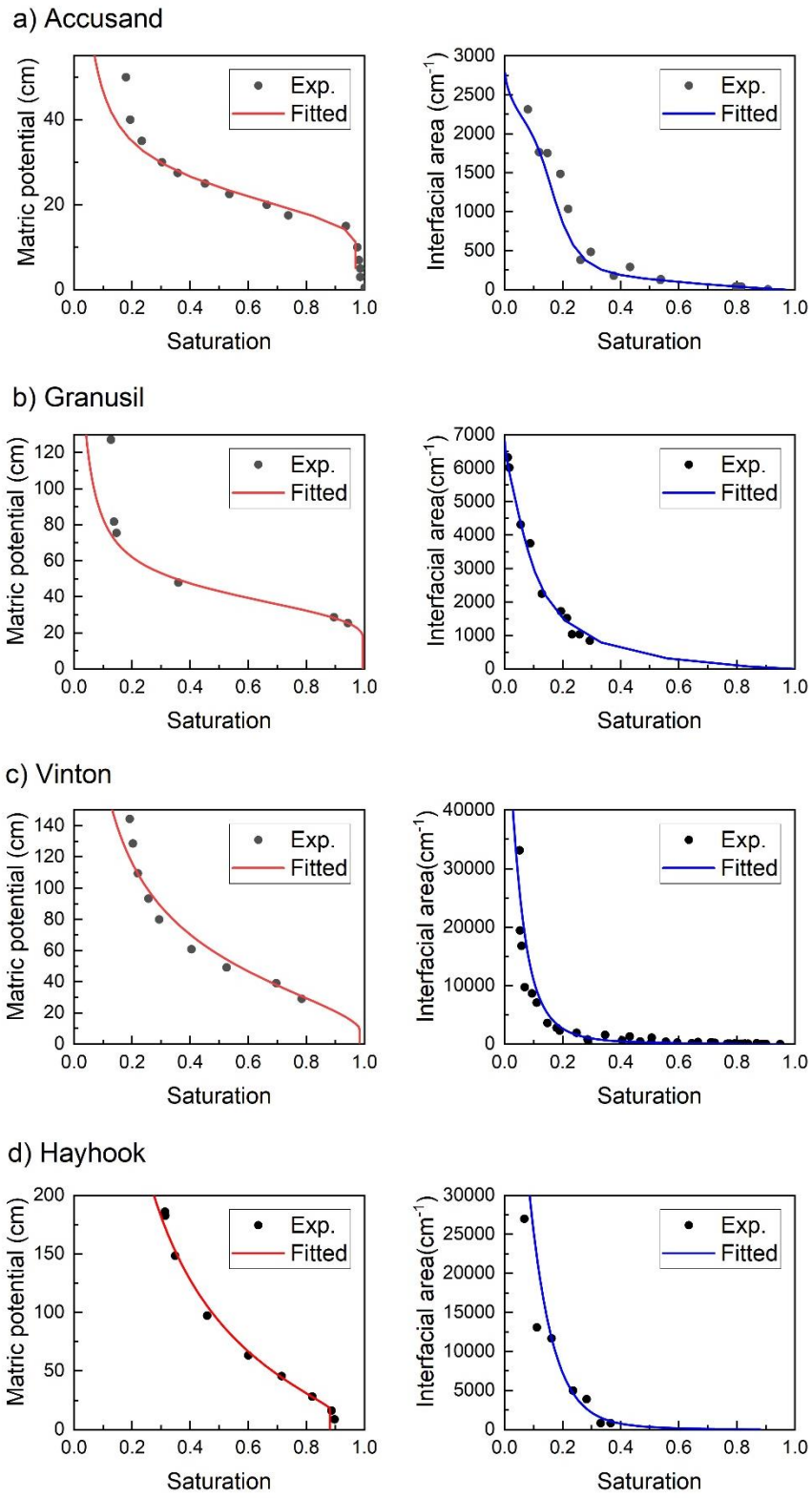

Figure 4. Model characterization results on the experimental data of $P_c - S_w$ and $A_{nw} - S_w$ measurements.

Values of the fitted model parameters, along with some other parameters of soil texture, e.g., median particle diameter d_{50} and uniformity coefficient U calculated by d_{60}/d_{10} are given in Table 2 according to the reported data (Peng & Brusseau, 2012). The results from another model test run on the literature data reported by Kim et al. (1997, 1999) are also listed in Table 2. The actual critical film thickness, h_c, which corresponds to the value of h_m, is calculated via the empirical film thickness equation given in Zheng et al. (2015) (see Appendix), showing the combined contributions of surface adsorption and capillarity to film thickness. In the view of surface roughness characterization, the primary concern is whether there are quantitative correlations between the surface roughness-related parameters and the sample-scale features, such as particle and pore size distribution.

Characterization results in Table 2 show that the traditional sample-scale parameters, e.g., uniformity coefficient U, lognormal average pore size length L_m, specific surface area A_r, and the solid roughness factor X, all show some degree of correlations with soil texture, especially between sands and soils. The one exception for the solid surface roughness factor is that of Hayhook, which is smaller than that of Vinton even though the former has a 70% larger specific solid surface area. This can be explained by the significantly larger uniformity coefficient of Hayhook soil, meaning it has a much larger grain-size distribution than the other media, which decreases the sample-scale capacity of surface roughness.

To test the correlations between micro-scale roughness properties and the sample-scale soil properties, results between X vs k and X vs h_c (critical thickness) are plotted in Figure 5. Inspection of Figure 5 shows that the correlation between sample-scale and micro-scale surface roughness in natural porous media is complicated. The logistic parameter k is poorly correlated to surface roughness factor X for the five media used in this study. Due to the randomness of k, it would be difficult to predict the fractal formations of natural porous media from soil texture. For instance, Vinton has far more specific surface area than Granusil, but it also has a larger value of k as well as a smaller h_m. Consequently,

the $A_{nw} - S_w$ curve of Vinton, in terms of Figure 3a, could be closer to the smooth-surface curve at some saturations, meaning that Vinton has stronger surface roughness masking than Granusil. Conversely, the critical thickness h_c presents some degree of correlation with X (R^2 = 0.84), which implies that rougher grain surfaces can induce the exponential increase of interfacial area at larger measuring scale.

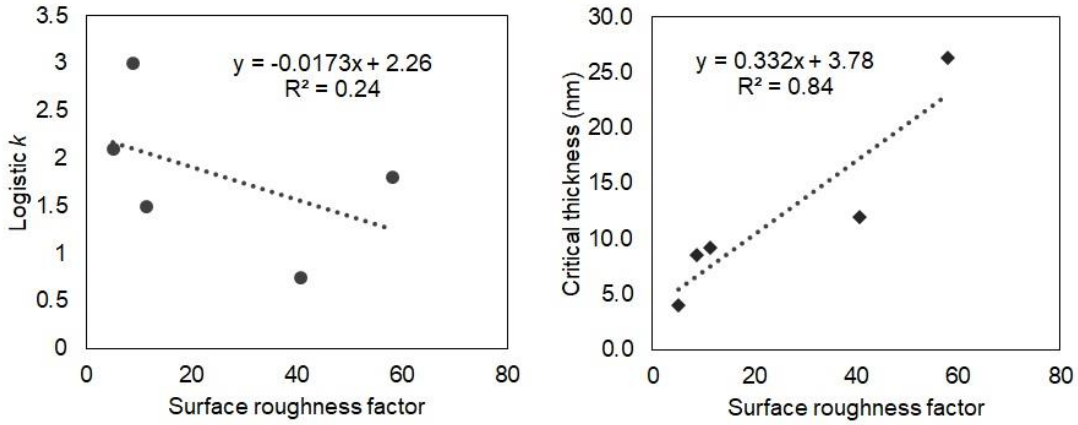

Figure 5. Correlations between the overall solid surface roughness factor X and micro-scale surface roughness characteristics.

The quantitative results in Table 2 and Figure 5 demonstrate the complexity of fluid-surface interactions. The competitive mechanism between surface adsorption and capillary forces for wetting film is assumed to occur at scales much smaller than the size of soil particles, and even smaller than the magnitude of relative surface height. Fluid-surface interaction on such micro-scale rough structures is controlled by the complicated and chaotic nature of fractal growth. Furthermore, the meso-scale (between single particle and finer structures) surface heterogeneity, such as pits and fractures on single grain surfaces (Araújo & Brusseau, 2019), would also increase the complexity of fractal properties for micro-scale roughness. Thus, the importance of surface roughness characterization is highlighted for a better demonstration of wetting film and its subsequent hydraulic properties.

4.3 Analysis of SEM images

The present modeling approach provides a different perspective to view surface roughness based on measured data for fluid-fluid interfacial areas. Introduction of inherent solid phase roughness parameters can avoid the scaling bias of direct measurement such as SEM or AFM, whereby higher resolutions lead to smaller measurable regions. To demonstrate these phenomena and compare with the characterization results, SEM images of the four porous media (Accusand, Granusil, Vinton, and Hayhook) used in this study are taken with a series of magnifications (500x, 2000x, 5000x, 20000x) (see Figure 6). The minimum and maximum magnifications (500x and 20000x) represent a change in image domain from approximately 35000 μm^2 to 40 μm^2 and resolutions from micrometer to nanometer scales. Images were obtained with a Hitachi S-4800 Field Emission SEM in the Kuiper Materials Imaging & Characterization Facility of the University of Arizona. SEM images are used to analyze visual associations between the real images of natural grain surfaces and the surface roughness parameters X, k, and h_m (h_c).

First, some meso-scale features, such as fractures on grain surfaces, can be identified from the 500x SEM images, as are pointed out in the rectangular indicators for Granusil and Vinton. The sub-iterations of these heterogeneous structures are obviously different from the more homogeneous surface domains. It is also observed that the meso-scale surfaces of Vinton appear more divergent than other media, as is indicated by the circle indicators of two surface regions with highly distinctive apparent roughness. This may partially explain the apparently anomalous value of k for Vinton. To mitigate the uncertainties from heterogeneity, the following magnified regions are selected to the seemingly roughest sites in the 500x images. The 2000x and 5000x images correspond to the reported magnitudes (0.1~1 μm) of relative surface height representation (Adams et al., 2012; Kibbey, 2013; Kim et al., 2012; Tokunaga et al., 2003). All media show apparent uniform surface structures at these two levels. It could be assumed that wetting liquid films at these scales are held primarily by capillary forces and remain sufficiently thick. However,

the potential for additional roughness scales for the soil media (Vinton and Hayhook) is manifest in the 5000x images, while the sandy media (Accusand and Granusil) exhibit a larger proportion of smoothness in the images.

In the 20000x images, the thickness of roughness layers is in the range of tens of nanometers, close to the magnitudes of critical thickness (h_c) in Table 2. It is possible to recognize the iterated sub-layers of fractal roughness at this level. Inspection of the 20000x images provides a possible verification to the correlation between overall surface roughness factor and critical thickness in Figure 5. At this level, the sandy media (Accusand and Granusil) only have a limited number of small and flat structures (as indicated in images) for the expansion of surface area, while the soil media (Vinton and Hayhook) present larger and deeper roughness formations that allow for further iterations of roughness scales. Such spatial differences can produce the differences in the nitrogen-BET surface areas between the sands and soils. However, it is also noticeable that surface information at this magnification has been considerably lost. It would be difficult to establish the explicit quantitative connections between the characterized modeling results and the SEM images at this degree of magnification. Rather, it is further highlighted that the modeling approach based on sample-scale measurement has the unique capability of extracting the micro-scale information of fluid-solid interaction that is operationally relevant to flow and transport, which is difficult to ascertain from imaging methods.

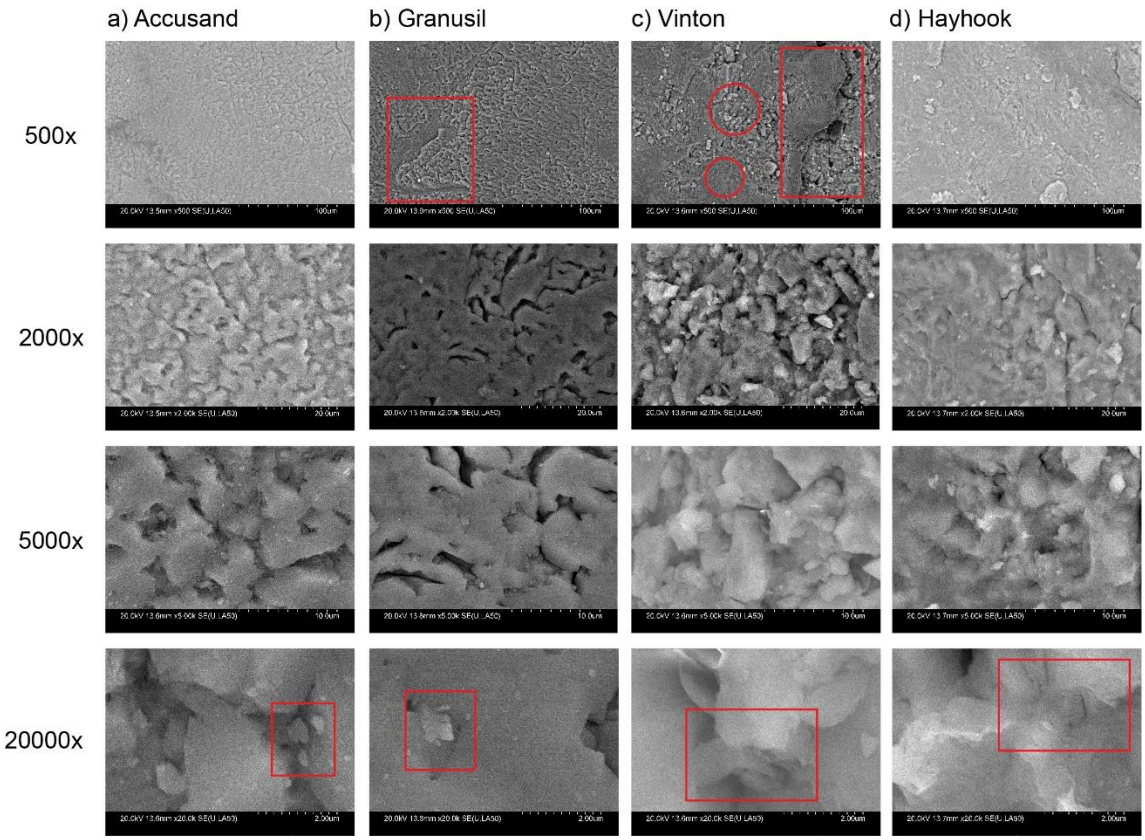

Figure 6. SEM images of the grain surfaces of the selected porous media. Boxes in 500x images show the fractured meso-scale structures on the surfaces of Granusil and Vinton. Circles in the 500x images of Vinton show the distinctive apparent meso-scale roughness of Vinton. Boxes in the 20000x images indicate the typical structures that are critical for further growth of surface area.

4.4 Feasibility for NAPL-water Fluid Systems

The validity of surface roughness characterization in the present method is based upon the premise that solid surface roughness remains constant regardless of any arbitrary flow conditions. Actual environmental problems can involve complicated fluids and saturations, especially when immiscible (nonaqueous phase) organic liquids (NAPL) are present. Surface roughness may have various impacts on different fluid systems (e.g., air-water or oil-water), and on different hydraulic properties (e.g., SWC, hydraulic conductivity, permeability, etc.). Hence, a brief feasibility test is conducted in this section using the published experimental data with different nonwetting fluids (air or NAPL) for the same

material (Accusand) in Figure 7. Air-water A_{nw} measurements are reported in Brusseau et al. (2015) and Peng & Brusseau (2005), and NAPL-water A_{nw} measurements using tetrachloroethene (PCE) are reported in Zhong et al. (2016). It is noted that the air-water A_{nw} data were measured with gas-phase IPTT at lower water saturations. In contrast, PCE-water interfacial areas were only accessible at relatively higher water saturations. To implement the verification, the air-water SWC and IPTT data are fitted following the modeling equations (7~13) (as reported in Jiang et al., 2019). The optimization produces values of the five critical parameters − L_m, σ, X, k, and h_m. The model is then applied to the PCE-water data by substituting the surface tension γ for water with the interfacial tension between PCE and water. Data used in Figure 7 are 0.0728 N/m for air-water and 0.0459 N/m for PCE-water.

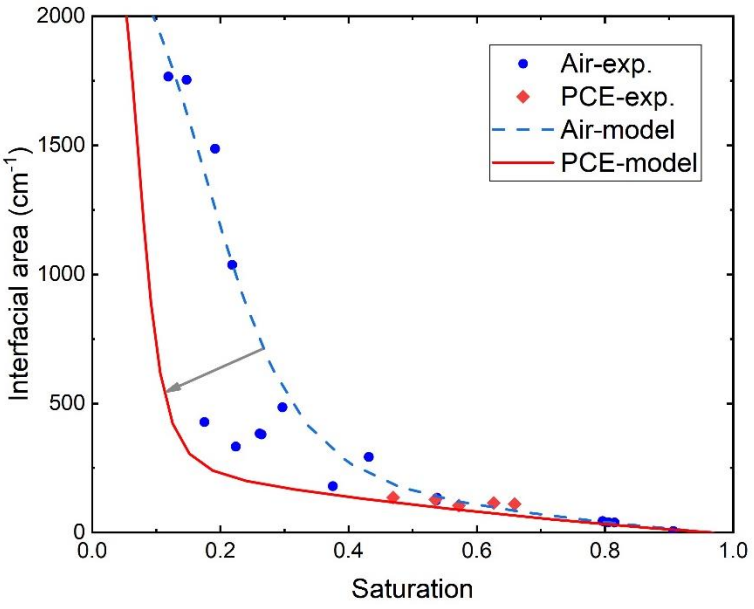

Figure 7. Feasibility test for the air-water and PCE-water interfacial areas measured from IPTT. Air-water curve (blue dashed line) is fitted from the experimental data points. PCE-water curve solid red line) is predicted using the model parameters obtained from calibration to the air-water data.

As is shown in Figure 7, the characterization of surface roughness provides a good

consistency for different water (wetting) saturations and different nonwetting fluids. The predicted PCE-water A_{nw} curve also shows good accuracy on the measured data points. These results indicate the validity of the approach for characterizing wetting-film configuration. Generally, decreasing interfacial tension causes longer dominance of capillary force in the wetting film, which makes the exponential increase of interfacial area induced by surface roughness occur later in drainage. However, at higher saturations, interfacial areas for both fluid pairs are similar, meaning that wetting films at this stage are capillary-dominant, wherein the film interfaces are not perceptive to matric potential. Similar experimental evidence was reported by Schaefer et al. (2000a, 2000b), in which fluid-pairs with different interfacial tensions presented similar interfacial areas in mass balance–based measurements. However, mass balance–based experiment would be able to represent the capillary-dominant state of wetting film, but are not fully accessible to the adsorption-dominant wetting film at very low saturations, whose properties are better captured by the gas-phase IPTT measurement. Thus, it is suggested that the interfacial tension between immiscible fluids has primary impact on adsorption-dominant films presented at lower saturations. For practical situations with unsaturated media at $S_w > 0.5$, it is likely to assume universal interfacial-area estimations for contaminant (e.g. PFAS) transport (e.g., Brusseau et al., 2019; Silva et al., 2019). For soils with lower water contents, the characterization of surface roughness using the present modeling method can be employed to extrapolate the A_{nw} curves for varying nonwetting fluids other than air.

5. Conclusions

This paper develops a methodology to employ the measurements of $A_{nw} - S_w$ curves to characterize the fluid-surface interaction controlled by micro-scale surface roughness. The method is based on a general theory of adsorbed wetting films on rough solid surfaces, where the films are held by the competitive forces between surface adsorption and capillary forces. The characterization is realized by quantifying the change of film-associated

fluid—fluid interfacial area between capillary-dominant states (smooth film) and adsorption-dominant states (rough film) controlled by matric potentials. As the quantification of wetting-film formations employs use of sample-scale measurements of porous media (e.g., nitrogen-BET and IPTT), it provides an effective approach to conceptualize and simulate the multiple scales of roughness associated with the fractal geometry of natural grain surfaces. The wetting-film *vs* matric-potential approach incorporates the advantages of surface roughness representations using both fractal dimension and area factor, which expands the scope of grain surface roughness beyond the traditional approach of relative surface height. The use of IPTT measurements establishes a complete picture of fluid-surface interaction across all grain surfaces within a porous medium, which is free of any spatial limitation. This advantage well compensates the information lost on traditional surface metrological approaches such as SEM and AFM.

The model characterization and SEM imaging results on the selected porous media in this study reveal the complexity of natural grain surfaces. The surface heterogeneity of natural grain surfaces is present across multiple scales – from sample and particle scales, to the meso-scale on one grain surface, and then to the micro-scale surface roughness following fractal dimensions. Surface roughness at different scales may exhibit some cross-scale correlations, such as between the overall surface roughness factor X and the critical micro-scale rough thickness h_c; rather, it could also be poorly correlated to the texture of porous media, such as presented by the logistic parameter k. Given the complicated nature of grain surfaces, the well-developed experimental measurement of fluid-fluid interfacial area, especially the low-S_w measurement using gas-phase tracers, provides a more reliable and controllable approach to characterize the surface properties based on the formation of wetting film.

The proposed characterization methodology promises numerous outlooks for environmental applications involving the transport phenomena between soil, fluids and atmosphere. The “surface-fluid triangle” and explicit logistic parameters defined by the

general model approach are the inherent properties of porous media. Based on the characterized soil properties, the methodology can be easily modified for immiscible- fluid pairs other than air-water. It could be particularly useful for the calculation of interfacial areas for sites contaminated by NAPL or sites with deep, low moisture-content vadose zones, where water saturation is low and mostly present as wetting films. It would also be useful for providing interfacial areas for systems influenced by mass exchange across solid-film-air interfaces, such as transport of contaminants undergoing biotransformation, or transport of colloids and solutes that adsorb at fluid-fluid interfaces. The present approach can be incorporated into a comprehensive flow and transport model to simulate mass transport in such systems.

Acknowledgements

This research was supported in part by a grant from the NIEHS Superfund Research Program (P42 ES04940). We acknowledge NASA grants #NNX12AL47G, #NNX15AJ22G and #NNX07AI520, and NSF grants #1531243 and #EAR-0841669 for funding of the instrumentation Hitachi S-4800 Field Emission SEM in the Kuiper Materials Imaging and Characterization Facility at the University of Arizona.

Appendix: Summary of Model Parameters and Derivations

Parameter	Nomenclature	Dimension	Annotation	Equation
Fluid properties				
ρ	Density of wetting fluid	ML^{-3}		
γ	Surface or interfacial tension	$ML^{-1}T^{-2}$	Can be switched to different fluid pairs.	
Measurable variables in experiments				
μ	Matric potential	L^2T^{-2}	Equivalent to capillary pressure P_c or pressure head H.	$\mu = gH$ $P_c = \rho\mu$
S_w	Wetting-fluid saturation	---		
A_{nw}	Nonwetting-wetting interfacial area	L^{-1}	Referred to the total interfacial area, but almost equal to film-associated area at most S_w. Measured by IPTT.	
A_r	Specific solid surface area (rough surface area)	L^{-1}	Measured by N_2/BET.	
Parameters in wetting film model				
X	Overall surface roughness factor	---	Ratio of rough surface area over smooth surface area for the porous medium	$X = A_r/A_s$
X_a	Interfacial area factor	---	Ratio of film area over smooth surface area. Function of matric potential.	$X_a = A_{nw}/A_s$

$h_{ad}(\mu)$	Adsorptive film thickness	L	Film thickness with only surface adsorption. Function of matric potential.	$h_{ad}(\mu) = \sqrt[3]{\frac{A_{svl}}{6\pi\rho\mu}}$
$h(\mu)$	Actual film thickness	L	Film thickness with both capillary and surface adsorption.	$h(\mu) = X_t h_{ad}(\mu)$
X_t	Film thickness factor	---	Calculated by empirical equation (Zheng et al., 2015).	$X_t = \begin{cases} X & h_{ad} \geq 10\,\text{nm} \\ X\left(\frac{h_{ad}(\mu)}{10}\right)^{\frac{\ln X}{\ln \frac{200}{7}}} & 0.35\,\text{nm} < h_{ad} < 10\,\text{nm} \\ 1 & h_{ad} \leq 0.35\,\text{nm} \end{cases}$
k	Logistic growth rate factor	L^{-1}	Given by logistic function of X_a.	$X_a = \frac{X + e^{k(h_{ad} - h_m)}}{1 + e^{k(h_{ad} - h_m)}}$
h_m	Critical adsorptive film thickness	L		
Parameters in sample upscaling				
$r(\mu)$	Meniscus radius	L	Given by Young-Laplace equation.	$r(\mu) = -\frac{\gamma}{\rho\mu}$
L	Pore side length	L	Side length of an equilateral triangular pore.	
L_m	Mean pore side length	L	Given by lognormal equation.	$f(L) = \frac{1}{L\sigma\sqrt{2\pi}} \exp\left(-\frac{[\ln(L/L_m)]}{2\sigma^2}\right)$
σ	Lognormal standard deviation	---		
L_{min}	Minimum pore side length	L	Set as a very small number.	$L_{min} = 5\times10^{-9}$ m
L_{max}	Maximum pore side length	L	Pore size associated with air-entry potential.	$L_{\max} = L_1(\mu) + 2h(\mu_d)$
μ_d	Air-entry potential	L^2T^{-2}	Can be derived from Brooks & Corey method.	

F_3	Corner area factor	---	Geometric factor for equilateral triangles.	$F_n = 3\sqrt{3} - \pi$
A_3	Pore area factor	---	Geometric factor for equilateral triangles.	$A_3 = \sqrt{3}/4$
C_3	Drainage blob radius factor	---	Geometric factor for equilateral under drainage.	$C_3 = 2\left[\sqrt{3} + \sqrt{\pi/\sqrt{3}}\right]$

References

Adams, T., Grant, C., & Watson, H. (2012). A simple algorithm to relate measured surface roughness to equivalent sand-grain roughness. *Journal ISSN*, *2929*, 2724.

Araújo, J. B., & Brusseau, M. L. (2019). Novel fluid-fluid interface domains in geologic media. *Environmental Science: Processes and Impacts*, *21*(1), 145–154. https://doi.org/10.1039/c8em00343b

Brown, S. R. (1987). Fluid flow through rock joints: the effect of surface roughness. *Journal of Geophysical Research: Solid Earth*, *92*(B2), 1337–1347.

Brown, S. R. (1989). Transport of Fluid and Electric Current Through a Single Fracture. *Geophysical Research Letters*, *94*(2), 9429–9438.

Brusseau, M. L., Peng, S., Schnaar, G., & Costanza-Robinson, M. S. (2006). Relationships among air-water interfacial area, capillary pressure, and water saturation for a sandy porous medium. *Water Resources Research*, *42*(3).

Brusseau, M. L., Peng, S., Schnaar, G., & Murao, A. (2007). Measuring air− water interfacial areas with x-ray microtomography and interfacial partitioning tracer tests. *Environmental Science & Technology*, *41*(6), 1956–1961.

Brusseau, M. L., El Ouni, A., Araujo, J. B., & Zhong, H. (2015). Novel methods for measuring air–water interfacial area in unsaturated porous media. *Chemosphere*, *127*, 208–213.

Brusseau, M. L., Yan, N., Van Glubt, S., Wang, Y., Chen, W., Lyu, Y., et al. (2019). Comprehensive retention model for PFAS transport in subsurface systems. *Water Research*, *148*, 41–50. https://doi.org/10.1016/j.watres.2018.10.035

Cassie, A. B. D., & Baxter, S. (1944). Wettability of porous surfaces. *Transactions of the*

Faraday Society, *40*, 546–551.

Costanza-Robinson, M. S., & Brusseau, M. L. (2002). Air-water interfacial areas in unsaturated soils: Evaluation of interfacial domains. *Water Resources Research*, *38*(10), 13-1-13–17. https://doi.org/10.1029/2001wr000738

Crawford, J. W. (1994). The relationship between structure and the hydraulic conductivity of soil. *European Journal of Soil Science*, *45*, 493–502.

Ghanbarian, B., Hunt, A. G., & Daigle, H. (2016). Fluid flow in porous media with rough pore-solid interface. *Water Resources Research*, *52*(3), 2045–2058.

Giménez, D., Allmaras, R. R., Huggins, D. R., & Nater, E. A. (1997). Prediction of the Saturated Hydraulic Conductivity-Porosity Dependence Using Fractals. *Soil Science Society of America Journal*, *61*(5), 1285–1292.

Hassanizadeh, S. M., & Gray, W. G. (1993). Thermodynamic basis of capillary pressure in porous media. *Water Resources Research*, *29*(10), 3389–3405.

Hirasaki, G. J. (1991). Wettability: fundamentals and surface forces. *SPE Formation Evaluation*, *6*(2), 217–226. https://doi.org/10.2118/17367-PA

Kibbey, T. C. G. (2013). The configuration of water on rough natural surfaces: Implications for understanding air-water interfacial area, film thickness, and imaging resolution. *Water Resources Research*, *49*(8), 4765–4774.

Jiang, H., Guo, B., & Brusseau, M. L. (2019). Pore-scale modeling of fluid-fluid interfacial area in variably saturated porous media containing microscale surface roughness. *Water Resources Research*, 55.

Kim, H., Rao, P. S. C., & Annable, M. D. (1997). Determination of effective air-water interfacial area in partially saturated porous media using surfactant adsorption. *Water Resources Research*, *33*(12), 2705–2711.

Kim, H., Rao, P. S. C., & Annable, M. D. (1999). Gaseous Tracer Technique for Estimating Air–Water Interfacial Areas and Interface Mobility. *Soil Science Society of America Journal*, 1554–1560.

Kim, T. W., Tokunaga, T. K., Shuman, D. B., Sutton, S. R., Newville, M., & Lanzirotti, A. (2012). Thickness measurements of nanoscale brine films on silica surfaces under geologic CO2sequestration conditions using synchrotron X-ray fluorescence. *Water Resources Research*, *48*(9).

Lampurlanés, J., & Cantero-Martínez, C. (2006). Hydraulic conductivity, residue cover and soil surface roughness under different tillage systems in semiarid conditions. *Soil and Tillage Research*, *85*(1–2), 13–26.

Liu, G., Zhang, M., Ridgway, C., & Gane, P. (2014). Pore wall rugosity: The role of

extended wetting contact line length during spontaneous liquid imbibition in porous media. *Colloids and Surfaces A: Physicochemical and Engineering Aspects*, *443*, 286–295. https://doi.org/10.1016/j.colsurfa.2013.11.033

Mandelbrot, B. B. (1983). *The fractal geometry of nature* (Vol. 173). WH freeman New York.

Oliver, J. P., Huh, C., & Mason, S. G. (1980). An experimental study of some effects of solid surface roughness on wetting. *Colloids and Surfaces*, *1*(1), 79–104.

Or, D., & Tuller, M. (1999). Liquid retention and interfacial area in variably saturated porous media: Upscaling from single-pore to sample-scale model. *Water Resources Research*, *35*(12), 3591–3605.

Or, D., & Tuller, M. (2000). Flow in unsaturated fractured porous media: Hydraulic conductivity of rough surfaces. *Water Resources Research*, *36*(5), 1165–1177.

Pachepsky, Y. A., Shcherbakov, R. A., & Korsunskaya, L. P. (1995). Scaling of soil water retention using a fractal model. *Soil Science*. https://doi.org/10.1097/00010694-199502000-00003

Peng, S., & Brusseau, M. L. (2005). Impact of soil texture on air-water interfacial areas in unsaturated sandy porous media. *Water Resources Research*, *41*(3).

Peng, S., & Brusseau, M. L. (2012). Air-Water Interfacial Area and Capillary Pressure: Porous-Medium Texture Effects and an Empirical Function. *Journal of Hydrologic Engineering*, *17*(7), 829–832.

Perfect, E. (1999). Estimating soil mass ffactal dimensions from water retention curves. *Geoderma*, *88*, 221–231. https://doi.org/10.1046/j.1365-2389.2001.00418-10.x

Philip, J. R. (1978). Adsorption and capillary condensation on rough surfaces. *Journal of Physical Chemistry*, *82*(12), 1379–1385. https://doi.org/10.1021/j100501a012

Resurreccion, A. C., Moldrup, P., Tuller, M., Ferré, T. P. A., Kawamoto, K., Komatsu, T., & De Jonge, L. W. (2011). Relationship between specific surface area and the dry end of the water retention curve for soils with varying clay and organic carbon contents. *Water Resources Research*, *47*(6).

Schaefer, C. E., DiCarlo, D. A., & Blunt, M. J. (2000). Determination of water-oil interfacial area during 3-phase gravity drainage in porous media. *Journal of Colloid and Interface Science*, *221*(2), 308–312. https://doi.org/10.1006/jcis.1999.6604

Schaefer, C. E., Dicarlo, D. A., & Blunt, M. J. (2000). Experimental measurement of air-water interfacial area during gravity drainage and secondary imbibition in porous media. *Water Resources Research*, *36*(4), 885–890.

Silva, J. A. K., Martin, W. A., Johnson, J. L., & McCray, J. E. (2019). Evaluating air-

water and NAPL-water interfacial adsorption and retention of Perfluorocarboxylic acids within the Vadose zone. *Journal of Contaminant Hydrology*, *223*(April), 103472. https://doi.org/10.1016/j.jconhyd.2019.03.004

Thompson, M. E., & Brown, S. R. (1991). The effect of anisotropic surface roughness on flow and transport in fractures. *Journal of Geophysical Research: Solid Earth*, *96*(B13), 21923–21932.

Tokunaga, T. K. (2011). Physicochemical controls on adsorbed water film thickness in unsaturated geological media. *Water Resources Research*, *47*(8).

Tokunaga, T. K., & Wan, J. (1997). Water film flow along fracture surfaces of porous rock. *Water Resources Research*, *33*(6), 1287–1295. https://doi.org/10.1029/97WR00473

Tokunaga, T. K., Olson, K. R., & Wan, J. (2003). Moisture characteristics of Hanford gravels. *Vadose Zone Journal*, *2*(3), 322–329.

Toledo, P. G., Novy, R. A., Davis, H. T., & Scriven, L. E. (1990). Hydraulic conductivity of porous media at low water content. *Soil Science Society of America Journal*, *54*(3), 673–679. https://doi.org/10.2136/sssaj1990.03615995005400030007x

Tuller, M., Or, D., & Dudley, L. M. (1999). Adsorption and capillary condensation in porous media: Liquid retention and interfacial configurations in angular pores. *Water Resources Research*, *35*(7), 1949–1964.

Wenzel, R. N. (1936). Resistance of solid surfaces to wetting by water. *Industrial & Engineering Chemistry*, *28*(8), 988–994.

Zheng, W., Yu, X., & Jin, Y. (2015). Considering surface roughness effects in a triangular pore space model for unsaturated hydraulic conductivity. *Vadose Zone Journal*, *14*(7), 1–13. https://doi.org/10.2136/vzj2014.09.0121

Zhong, H., El Ouni, A., Lin, D., Wang, B., & Brusseau, M. L. (2016). The two-phase flow IPTT method for measurement of nonwetting-wetting liquid interfacial areas at higher nonwetting saturations in natural porous media. *Water Resources Research*, *52*(7), 5506–5515. https://doi.org/10.1002/2016WR018783.

Appendix C

Case Study: Modeling the Vadose-Zone Transport of PFAS

Background

Per- and poly-fluoroalkyl substances (PFAS) are a group of critical emerging contaminants of increasing concern. PFAS concentrations have been observed to be orders of magnitude greater than the health advisory level in groundwater. Typically, PFAS is released through military activities, such as firefighting training, but groundwater contaminations have also been reported in non-military sites. Therefore, the transport and fate between ground surface and groundwater, i.e., the vadose zone, is of great significance in the monitoring and remediation of PFAS contaminants.

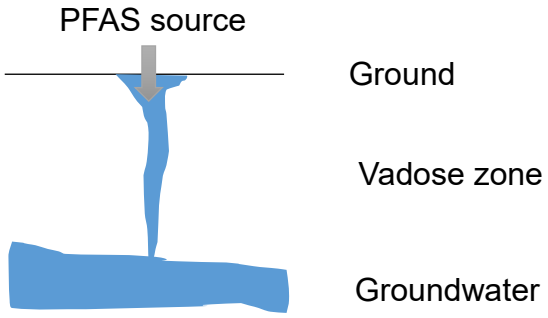

Figure 1. Illustration of a PFAS transport problem.

Brusseau et al., (2018, 2019) have proposed a comprehensive retention model for PFAS transport. The model evaluates the PFAS transport in a complicated system with four components: soil, water, NAPL and air. The model considers the mass transport of PFAS from the water phase to all other bulk phases and all interfaces. Miscible-displacement experiments were also conducted to verify the predictions from the retention model. Given this effective method for the retention behavior of PFAS in a complicated system, it is

useful to apply a one-dimensional vadose zone transport model to develop a comprehensive profile of PFAS concentrations, and simulate the release of PFAS plume into the groundwater zone.

Conceptual Model

I. Water flow

The present study will be based on the 1-D hydraulic flow transport model. The PFAS contaminants are released to the ground surface, and move through the soil via water flow (infiltration) within the vadose zone. In general, the water flow can be described using the Richards equation:

$$\frac{\partial \theta}{\partial t} - \frac{\partial}{\partial z}\left[K(\theta)\left(\frac{\partial h}{\partial z} + 1 \right) \right] = 0 \quad (1)$$

where θ is the volumetric water content, $K(\theta)$ is the unsaturated hydraulic conductivity, h is the matric head, z is the elevation above a vertical datum, and t is the time.

In this equation, the matric head h is connected to θ through the soil water characteristic curve, which can be estimated through the traditional van Genuchten equation, or using other modeling approaches.

On the other hand, the unsaturated hydraulic conductivity $K(\theta)$ is also related to θ using the traditional van Genuchten equation for hydraulic conductivity.

Therefore, equation (1) can be solved in terms of the vertical moisture profile θ(z, t) for a given type of soil.

II. PFAS transport

It is assumed that the mass transport of PFAS is following the Advection-Dispersion Equation (ADE) for typical solute transport, which is:

$$R\frac{\partial C}{\partial t} = D\frac{\partial^2 C}{\partial z^2} - v\frac{\partial C}{\partial z} \quad (2)$$

where C is the concentration of PFAS in a specific elevation z, $D = D_e/\theta$ is the diffusion-dispersion coefficient of PFAS, v is the velocity of advection (pore water velocity), and R is the retardation factor.

To calculate the pore water velocity, we can use the Darcy's Law to obtain the Buckingham-Darcy velocity:

$$J_w = -K(h)\frac{\partial H}{\partial z} \quad (3)$$

where H is the total hydraulic pressure head, with

$$H = h + z \quad (4)$$

Thus, the pore water velocity equals to:

$$v = \frac{J_w}{\theta} \quad (5)$$

The model for the retardation factor R of PFAS has been proposed by Brusseau et al. (2019), which can be also ultimately expressed as the function of the volumetric water content θ. Therefore, in order to solve equation (2), we may first solve equation (1) to generate the function of $\theta(z, t)$, and then, each value of θ is possible to yield the concentration profile of PFAS as $C(z, t)$.

III. Retention of PFAS

Brusseau et al. (2019) defines the retardation factor R of PFAS as follows:

$$R = 1 + \frac{1}{\theta}\left(K_d\rho_b + K_a\theta_a + K_{aw}A_{aw} + K_n\theta_n + K_{nw}A_{nw} + K_{an}A_{an}\right) \quad (6)$$

There are four phases: solid, water, NAPL and air, and three interfaces: air-water, air-NAPL and water-NAPL, that are involved equation (6) altogether. The subscripts a, w, n, represent air, water and NAPL, respectively. Amongst all the terms in equation (6), $K_d\rho_b$

represents the solid adsorption of PFAS; K_a and K_n represent the partitioning of PFAS between air/water and NAPL/water; K_{aw}, K_{nw} and K_{an} represent the interfacial adsorption of PFAS at the three types of interfaces. The volumetric contents of air and NAPL, θ_a and θ_n, follows the constraint:

$$\theta + \theta_a + \theta_n = n \qquad (7)$$

where n is the porosity.

The remaining parameters: A_{aw}, A_{nw}, and A_{an}, are associated with various interfacial-area models (including our latest triangular-tube BCC model or the empirical equation in Peng and Brusseau (2005)), which are also corresponded to θ. Brusseau et al. (2019) provides a full set of estimation methods to obtain the values of all of the adsorption and partitioning coefficients in equation (6). Therefore, a specific value of $R(\theta)$ can be generated for each location in the path of PFAS transport along the vadose zone.

Given the values of $R(\theta)$, equation (6) is now complete to be solved for a comprehensive concentration profile of $C(z, t)$. With $C(z, t)$, it is possible to estimate the magnitude of PFAS plume that is released to the groundwater, which is significant in the monitoring of PFAS contamination. It is also possible to acquire the amount of PFAS that is transported to soil, NAPL and atmosphere from the water phase.

IV. Application of the Proposed Methodology

Based on the proposed model in the manuscript of Appendix A, a specific porous medium can be expressed by five model parameters: L_m, σ, X, k, and h_m. Other important parameters, such as porosity, and physical properties of fluids such as density, surface tension, and viscosity are also available at the first stage. For the soil of a PFAS-contaminated site, required experimental work includes the soil water characteristic (SWC) measurement, N_2/BET measurement of specific solid surface area, and gas-phase IPTT. Based on experimental results, all of the five parameters are available for following

simulations.

Tuller & Or (2001) proposed a bundle-of-cylindrical-capillaries (BCC) model for soil hydraulic conductivity, in which they established explicit hydraulic conductivity for the proportions of duct, film, and corner flows, respectively. Zheng et al. (2015) proposed a similar BCC model that introduced the surface roughness factor, X, to the equations for film flow. According to Tuller & Or (2001), adsorption- and capillary- dominant films (as thin film and thick film) follow different flow equations. Zheng et al. (2015) modified these equations with the surface roughness factor X and interfacial area X_a. Using the BCC methodology in Appendix A, it is finalized that the total unsaturated hydraulic conductivity of the investigated porous medium is the function of all five parameters—L_m, σ, X, k, and h_m. Specifically, the pore-size-distribution parameters L_m and σ account for all duct, film and corner flows, and surface roughness – related X, k and h_m correlate to film flow. Therefore, the hydraulic conductivity used in the Richards equation is able to be generated by the proposed model:

$$K(h) = f_1(h,\ L,\ \sigma,\ X,\ k,\ h_m) \quad (8)$$

As is derived in our methodology, the SWC function has been quantified by the pore-size-distribution parameters. By switching saturation to volumetric water content θ, we know:

$$\theta = f_2(h,\ L_m,\ \sigma) \quad (9)$$

With equation (8), the profile of volumetric water content for different soil depth, $\theta(z, t)$, is complete to be realized. Meanwhile, our model has specified the fluid-fluid interfacial area as a function of matric potential (pressure head) with the same set of parameters:

$$A_{nw}(h) = f_3(h,\ L,\ \sigma,\ X,\ k,\ h_m) \quad (10)$$

It is noted that the nonwetting-wetting fluid pair in A_{nw} can be adjusted on the term of interfacial tension γ. In addition, the interfacial tension γ may be affected by the concentration of PFAS. Based on the conclusion of Appendix B, it is assumed that A_{nw} is

independent of γ at $S_w > 0.5$. At $S_w < 0.5$, A_{nw} is coupled with the concentration of PFAS.

Given the water content profile $\theta(z, t)$, it is sufficient to calculate the interfacial terms. Determinations of all K-related coefficients in equation (6) have been thoroughly discussed in Brusseau et al. (2019). It is feasible to derive the retardation factor R as a function of water content $\theta(z, t)$, and then establish its profile with soil depth.

Finally, the advective-dispersion equation (2) is complete to solve. The diffusion coefficient D_e may be collected from literature or estimated from the molecular structure of the specific PFAS compounds. The pore water velocity v is correlated to the as-obtained function of hydraulic conductivity by equation (8). Numerical solution to equation (2) will generate the concentration profile of PFAS compounds, $C(z, t)$, in the aqueous phase. The corresponding concentrations of PFAS in other phases and on interfaces can be all calculated from the various K-related coefficients in equation (6).

Conclusions

In this short article, we used the pre-developed mathematical models to analyze the feasibility of the methodology in Appendix A and B for a type of specific surfactant-like contaminants—PFAS. A unique feature of the transport model for such chemicals is the critical proportion of interfacial-area items, which has been comprehensively delineated in the proposed methodology. This article has discussed the complete procedure to apply the methodology in a practical contaminated site, and validated the feasibility from the derived equations. Future developments of the procedure would be the realization of $K(h)$ in equation (6), and treatment of the coupling items in the different equations for flow, transport and retention. Finally, with the input hydrological data and release concentration of PFAS as initial and boundary conditions, the vadose zone transport model for PFAS is complete for simulations.

References

Brusseau, M. L. (2018). Assessing the potential contributions of additional retention processes to PFAS retardation in the subsurface. *Science of the Total Environment*, *613–614*, 176–185. https://doi.org/10.1016/j.scitotenv.2017.09.065

Brusseau, M. L., Yan, N., Van Glubt, S., Wang, Y., Chen, W., Lyu, Y., et al. (2019). Comprehensive retention model for PFAS transport in subsurface systems. *Water Research*, *148*, 41–50. https://doi.org/10.1016/j.watres.2018.10.035

Tuller, M., & Or, D. (2001). Hydraulic conductivity of variably saturated porous media: Film and corner flow in angular pore space. *Water Resources Research*, *37*(5), 1257–1276. https://doi.org/10.1029/2000WR900328

Zheng, W., Yu, X., & Jin, Y. (2015). Considering surface roughness effects in a triangular pore space model for unsaturated hydraulic conductivity. *Vadose Zone Journal*, *14*(7), 1–13. https://doi.org/10.2136/vzj2014.09.0121

Appendix D

Example MATLAB Codes for Model Application on a Given Medium

Function file for film thickness – hrough.m

```
function h = hrough (mu, X, Asvl, rou)
% film thickness with surface roughness factor.
mu_1 = -3.19;
mu_2 = -7.44e4;
h = zeros(length(mu),1);
h_ad = (Asvl./(6*pi*rou*mu)).^(1/3);


for i = 1:length(mu)
    if mu(i) >= mu_1
        h(i) = (X)*h_ad(i);
    elseif mu(i) <=mu_2
        h(i) = h_ad(i);
    else
        h(i) = (X).*(h_ad(i)/10^-8).^(log(X)/(log(200)-log(7))).*h_ad(i);
    end
end
end
```

Function file for lognormal distribution – Lognormal.m

```
function [ A ] = Lognormal ( L , Lm, sd )
% Statistical distribution of pore size.
 A = (1./(L.*sd.*(2.*pi)^0.5)).*exp(-(log(L./Lm)).^2./(2*sd^2));
 end
```

Function file for total saturation – RoughSwL.m

```
function [S, Sd, Sc, Sf] = RoughSwL (mu, X, mu_m, Lm, sd)
% Output: Total saturation (S) and duct, corner, film saturation.
% Input parameters
% mu: range of chemical potential (J/kg).
% Lm: mean pore side length.
% X: surface roughness factor.
% sd: standard deviation.
% Pore geometry related parameters.


global sigma
n = 3;
angle_deg = 180-360/n;
angle_rad = angle_deg*pi/180;
Fn = n*(1/tan(angle_rad/2)-pi*(180-angle_deg)/360);
An = (n/4)*cos(pi/n)/sin(pi/n);
Cn = (2*(Fn+pi)+2*(pi*(Fn+pi))^.5)/n;


% Physical properties.
rou = 998.21; %liquid density (kg/m3)
Asvl = -6e-20; %Hamaker constant
g = 9.81;


% Determine Lmax and Lmin.
hb = (Asvl./(6.*pi.*rou.*mu_m)).^(1/3);
rb = -sigma/(rou*mu_m);
Lb = rb*Cn;
Lmax = Lb+2*hb;
Lmin = 5e-9;
had_mu = (Asvl./(6*pi*rou*mu)).^(1/3); % Adsorptive film thickness.
h_mu = hrough (mu, X, Asvl, rou); % Total film thickness.
r_mu = -sigma./(rou*mu);
```

```
% Surface roughness and surface length coefficient.
Xt_mu = h_mu./had_mu;


L1 = zeros(length(mu),1);
Sd = zeros(length(mu),1);
Sf = zeros(length(mu),1);
Sc = zeros(length(mu),1);
 for i = 1:length(mu)
     % Calculate L1 with the integration limit.
     if   -sigma.*Cn/(rou*mu(i))>Lmax
     L1(i) = Lmax;
     elseif -sigma*Cn/(rou*mu(i))<Lmin
     L1(i) = Lmin;
     else
     L1(i) = -sigma*Cn/(rou*mu(i));
     end
     m = 500; % Number of spatial steps for integration
     dL1 = (L1-Lmin)/m; % Spatial step size
     dL2 = (Lmax-L1)/m;
     % Calculate the integral range for each given item in {mu}.
     Ld = Lmin:dL1(i):L1(i);
     Lfc = L1(i):dL2(i):Lmax;
    h = h_mu(i);
    r = r_mu(i);
    % Satruation of a single pore.
     Sud = 1;
     Suf = n*h*(Lfc-2*r*cot(pi/(2*n))./(An.*Lfc.^2);
     Suc = (n*Fn*r^2)./(An.*Lfc.^2);
     % Integral with the gamma function.
     Sd(i) = trapz(Ld, Sud.*Lognormal(Ld, Lm, sd));
     Sf(i) = trapz(Lfc, Suf.*Lognormal(Lfc, Lm, sd));
     Sc(i) = trapz(Lfc, Suc.*Lognormal(Lfc, Lm, sd));
end


S = Sd + Sf +Sc;
End
```

Function file for total interfacial area – RoughAnwL.m

```
function [A, Ac, Af] = RoughAnwL (mu, X, mu_m, Lm, sd)
% Output: Total interfacial area (A) and corner, film interfacial area.
% Input parameters
% mu: range of chemical potential (J/kg).
% Lm: mean pore side length.
% X: surface roughness factor.
% omega: standard deviation.


global k hm sigma

 % Pore geometry related parameters.
n = 3;
angle_deg = 180-360/n;
angle_rad = angle_deg*pi/180;
Fn = n*(1/tan(angle_rad/2)-pi*(180-angle_deg)/360);
An = (n/4)*cos(pi/n)/sin(pi/n);
Cn = (2*(Fn+pi)+2*(pi*(Fn+pi))^.5)/n;


% Physical properties.
rou = 998.21; %liquid density (kg/m3)
Asvl = -6e-20; %Hamaker constant
g = 9.81;
 % Determine Lmax and Lmin.
hb = (Asvl./(6.*pi.*rou.*mu_m)).^(1/3);
rb = -sigma/(rou*mu_m);
Lb = rb*Cn;
Lmax = Lb+2*hb;
Lmin = 5e-9;
had_mu = (Asvl./(6*pi*rou*mu)).^(1/3);
h_mu = hrough (mu, X, Asvl, rou);
r_mu = -sigma./(rou*mu);
```

```
% Surface roughness and surface length coefficient.
Xt_mu = h_mu./had_mu;
Xa_mu = (X+exp(k*(had_mu*10^9-hm)))./(1+exp(k*(had_mu*10^9-hm)));


L1 = zeros(length(mu),1);
Af = zeros(length(mu),1);
Ac = zeros(length(mu),1);
 for i = 1:length(mu)
     % Calculate L1 with the integration limit.
     if   -sigma.*Cn/(rou*mu(i))>Lmax
     L1(i) = Lmax;
     elseif -sigma*Cn/(rou*mu(i))<Lmin
     L1(i) = Lmin;
     else
     L1(i) = -sigma*Cn/(rou*mu(i));
     end
     m = 500; % Number of spatial steps for integration
     dL2 = (Lmax-L1)/m;
     % Calculate the integral range for each given item in {mu}.
     Lfc = L1(i):dL2(i):Lmax;
    r = r_mu(i);
    Xa = Xa_mu(i);
     % Interfacial area of a single pore.
     Auf = 3*Xa.*(Lfc-2*r*cot(pi/(2*n)))./(An.*Lfc.^2);
     Auc = 3*pi*0.5*r./(An.*Lfc.^2);
 % Interfacial area of the sample.
     Af(i) = trapz(Lfc, Auf.*Lognormal(Lfc, Lm, sd));
     Ac(i) = trapz(Lfc, Auc.*Lognormal(Lfc, Lm, sd));
end
A = Af + Ac;
end
```

Function file for saturation fitting – dfitSwL.m

```
function [mdS] = dfitSwL (x)
global Sw_exp mu_exp X mu_m
Sw_fit = RoughSwL (mu_exp, X, mu_m, x(1), x(2));
```

```
dS = (Sw_fit-Sw_exp).^2;
mdS = (sum(dS)/length(dS)).^0.5;
end
```

Main program file

```
clc
clear
global Sw_exp mu_exp X mu_m k hm sigma


k = 3.7;
hm = 9.7;
mu_m = -1.2;     %air entry potential (J/kg)
X = 8.5;   % Input surface roughness factor.


Sw_exp = [1 0.995051954 0.995051954 0.990103909 0.985155863 0.985155863 0.985155863
0.985155863 0.985155863 0.980207818 0.980207818 0.980207818 0.975259772 0.975259772
0.975259772 0.935675408 0.737753587 0.663532905 0.534883721 0.450766947 0.356754082
0.302325581 0.233052944 0.19346858    0.178624443 0.158832261 0.14893617    0.124195943
0.104403761 0.084611578 0.059871351 0.059871351]';
mu_exp = -[0.04905    0.0981    0.14715 0.1962    0.24525 0.2943    0.35316 0.44145 0.4905
0.5886    0.6867    0.7848    0.8829    0.981     1.22625 1.4715    1.71675 1.962     2.20725 2.4525
2.69775 2.943     3.4335    3.924     4.905     5.886     6.867     7.848     9.81      24.525    49.05
73.575]'; % measured matric potential (J/kg)
h_exp = -100*mu_exp/9.81;


Lm = 8e-5;     % Mean pore side length (m).
sd = 0.2;
mu1 = -0.5:-0.3:-50;
mu2 = -0.01:-.2:-50;
mu1 = mu1';
mu2 = mu2';
x0 = [Lm sd];

% Calculate Lmax.
```

```
n = 3;
angle_deg = 180-360/n;
angle_rad = angle_deg*pi/180;
Fn = n*(1/tan(angle_rad/2)-pi*(180-angle_deg)/360);
An = (n/4)*cos(pi/n)/sin(pi/n);
Cn = (2*(Fn+pi)+2*(pi*(Fn+pi))^.5)/n;


sigma = .0728; %surface tension (N/m)
rou = 998.21; %liquid density (kg/m3)
Asvl = -6e-20; %Hamaker constant
hb = (Asvl./(6.*pi.*rou.*mu_m)).^(1/3);
rb = -sigma/(rou*mu_m);
Lb = rb*Cn;
Lmax = Lb+2*hb;
Lmin = 5e-9;


A = [1 0; -1 0; 0 -1];
b = [Lmax; -Lmin; 0];
[x, fval] = fmincon('dfitSwL', x0, A, b);

Sw_fit1 = RoughSwL (mu1, X, mu_m, x(1), x(2));
h_fit = -100*mu1/9.81;


figure(1)
subplot(1,2,1)
semilogy(Sw_exp, -mu_exp, 'd', Sw_fit1, -mu1)
axis([0 1 1 100])
legend('Experiment', 'fitted')
xlabel('Saturation')
ylabel('Chemical Potential (J/kg)')


Sw_exp2 = [0.538       0.5365    0.815     0.7963    0.8055    0.080112783 0.11882034    0.147299348
0.191849763 0.218534619 0.261234968 0.906429901 0.431561836 0.375554304 0.296880097
]';
Anw_exp = [135    124.6     39.19     44.98     39.9       2313.975552 1766.963541 1754.155988
1487.404248 1037.533705 383.8866499 6.084365783 293.148182    180.2435198 485.5662701
]';
```

```
Sw_exp3 = [0.022712781    0.131525817 0.133784751 0.137384175 0.15296209    0.168329345
0.168428809 0.176587229 0.202467199 0.23000192    0.232583487 0.239466999 0.24
0.257461561 0.271721575 0.278469527 0.282049958 0.306274885 0.31571722    0.318463174
0.319025032 0.320699297 0.332127522 0.342415068 0.350216296 0.364540536 0.370772996
0.37422607    0.375583515 0.38        0.382432661 0.42        0.420574329 0.432729725 0.436949818
0.440434973 0.479220393 0.48        0.484145996 0.489779755 0.504257402 0.51        0.535248265
0.537283659 0.546124557 0.586768449 0.6 0.611082225 0.616416341 0.627172858 0.696521837
0.766348975 0.847759354 0.851260721 0.854067229 0.88        0.913556274 0.95
0.993948475]';
Anw_exp2 = [3.167894467 14.66367003 15.11064821 15.67596707 15.81130024 16.70291756
16.74835083 16.59614976 17.17243147 15.67051451 17.35363294 15.45189414 16.785
14.7221931    17.56684327 17.78815856 15.2003486    15.32049273 15.92591148 17.25074902
17.57166633 17.2893464    17.68327275 16.56876919 19.14360715 16.33516684 13.94823903
16.53401398 17.80634522 16.469    18.25008901 16.958    13.89671279 18.86680875 15.31546381
15.56192446 12.37011243 16.663    14.31034601 14.6947325    14.40811742 16.668    14.556832
16.5619965    16.53773558 11.32231601 16.589    13.90343798 9.898323479 13.76100458
16.43235459 12.32818931 16.50788625 6.81210285    5.359453426 16.155    6.153401384 11.366
1.570368694]';


Sw_fit2 = RoughSwL (mu2, X1, mu_m, x(1), x(2));
[Anw_fit, Anw_cap] = RoughAnwL(mu2, X1, mu_m, x(1), x(2));
Anw_fit = Anw_fit/100;


subplot(1,2,2)
plot(Sw_exp2, Anw_exp, 'd', Sw_fit2, Anw_fit,'b')
legend('Experiment-Total', 'Simulated-Total')
xlabel('Saturation')
ylabel('Interfacial area (cm^-1)')
```